Investigating the Orientational Order in Smectic Liquid Crystals

A DISSERTATION
SUBMITTED TO THE FACULTY OF THE GRADUATE SCHOOL
OF THE UNIVERSITY OF MINNESOTA
BY

Shun Wang

IN PARTIAL FULFILLMENT OF THE REQUIREMENTS
FOR THE DEGREE OF
Doctor of Philosophy

June, 2010

Acknowledgements

There are many people that have earned my gratitude for their contribution to my time in the graduate school. First and foremost I would like to thank my advisor C. C. Huang. I appreciate C. C.'s supervision, advice, and guidance to make my Ph.D experience both productive and stimulating. C. C. has taught me skills that a good experimental physicist should possess. C. C. also exemplifies all the qualities of a scientist e.g., patience, motivation, enthusiasm, intuition and immense knowledge.

The members in C. C's group have been extremely helpful to my thesis. LiDong Pan and I have been working together for four years. His help and suggestions have been vital to my research. John Liu has taught me the operation and data analysis of the differential optical reflectivity system. John Liu and Bradley "Peanut" McCoy have trained me to set up and perform the resonant x-ray diffraction experiments. Three undergraduate students, Chris Hennin, Can Zhang and Brian Moths, have been reliable colleagues while they are in the group.

I would also like to thank our collaborators, Dr. R. Pindak, Dr. S. T Wang from NSLS and Prof. P. Barois from Universite Bordeaux. The discussion with them when performing resonant x-ray diffraction has always been insightful.

Besides my advisor, I would like to thank the rest of my thesis committee; Prof. James Kakalios, Prof. Oriol Valls and Prof. James Leger.

Dedication

This thesis is dedicated to my parents, Yongyuan Wang and Fazhen Wu, and my wife, Dan Yang for their support and encouragement during all these years of study.

Abstract

This thesis is composed of two projects. The first one is the investigation of a reversed phase sequence, which subsequently leads to the discovery of a novel Smectic-C liquid crystal phase. The 10OHFBBB1M7 (10OHF) compound shows a reversed phase sequence with the SmC_{d4}^* phase occurring at a higher temperature than the SmC^* phase. This phase sequence is stabilized by moderate doping of 9OTBBB1M7 (C9) or 11OTBBB1M7 (C11). To further study this unique phase sequence, the mixtures of 10OHFBBB1M7 and its homologs have been characterized by optical techniques. In order to perform the resonant X-ray diffraction experiment, we have added C9 and C11 compounds to the binary mixtures and pure 10OHF. In two of the studied mixtures, a new smectic-C^* liquid crystal phase with six-layer periodicity has been discovered. Upon cooling, the new phase appears between the SmC_{α}^* phase having a helical structure and the SmC_{d4}^* phase with four-layer periodicity. The SmC_{d6}^* phase shows a distorted clock structure. Three theoretical models have predicted the existence of a six-layer phase. However, our experimental findings are not consistent with the theories.

The second project involves the mixtures of liquid crystals with different shapes. The role of different interactions in stabilizing the antiferroelectric smectic liquid crystal phases have been a long-standing questions in the community. By mixing the antiferroelectric smectic liquid crystal with achiral liquid crystal molecules with rod and hockey-stick shapes, distinct different behaviors are obtained. In the case of the mixtures of chiral smectic liquid crystals with rod-like molecules, all the smectic-C^* variant phases vanish with a small amount of doping. However, the hockey-stick molecule is much less destructive compared to the rod-like molecule. This suggests that the antiferroelectric smectic liquid crystal molecules may have a shape closer to a hockey-stick rather than a rod.

Contents

List of Tables

List of Figures

viii

Chapter 1

A Brief Introduction To Chiral Smectic-C* Liquid Crystals

1.1 What are liquid crystals?

Liquid crystals are materials that exhibit an intermediate state between the liquid and the solid phases. It may flow like the liquid but at the same time possesses some positional/orientational order like the solid crystal [1, 2]. Due to its structure and fluidity, such materials can be used in a variety of electro-optical display devices, such as LCD monitors and televisions. Liquid crystals can be divided into two groups; thermotropic and lyotropic. The phase transitions in thermotropic liquid crystals are driven by temperature. For the lyotropic liquid crystals, phases transitions depend on both the concentration of liquid crystals in the solvent and temperature. All the liquid crystals studied in my thesis are thermotropic. One of the most common liquid crystals is the rod-like liquid crystal. The shape of the molecule resembles that of a rod or a cigar. Rod-like liquid crystals often form the three phases shown in Fig. 1.1. In the nematic phase, there is no positional order. The long axes of the molecules orient themselves more or less in the same direction. In the smectic-A phase, the molecules form a layered structure. In the smectic-C phase, the long axes of the molecules tilt away from the layer normal.
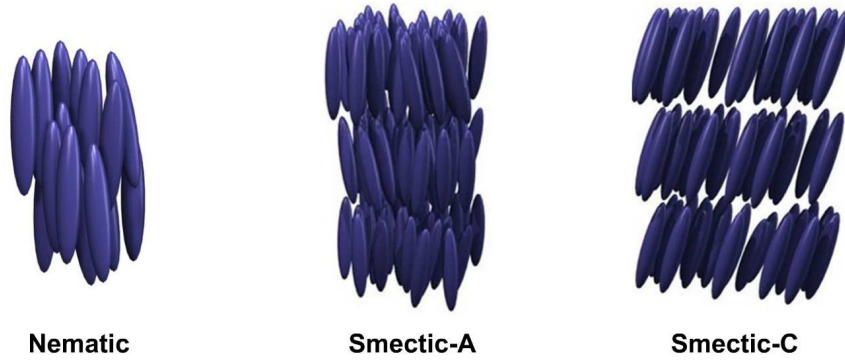
Figure 1.1: Each rod in the illustration represents one liquid crystal molecule.

1.2   Chiral smectic-C* phases

If the molecules are chiral, because of the chiral symmetry breaking, there is sponta-neous polarization perpendicular to the tilt plane in the smectic-C phase. This polar-ization induces many more interesting phases called chiral smectic-C* (SmC*) variant phases.[3, 4, 5]. They show heli-, ferro-, ferri- or antiferro-electric response with large polarization, which enables potential applications in fast electro-optical switching ap-plications. Extensive efforts have been aimed at investigating the SmC* variant phases by scientists and engineers in the past twenty years. To date, the interlayer arrange-ments of these phases have been unambiguously revealed experimentally; they exhibit a clock structure having periodicity of a few (SmC$^*_\alpha$), tens of (SmC*), four (SmC$^*_{d4}$), three (SmC$^*_{d3}$) and two layers (SmC$^*_A$) as illustrated in Fig. 1.2. Many theoretical advances have been made to explain the origin of their rich variety and complex structures, for example the continuous model, the discrete model and Ising-like model. However, the-orists still agree that the underlying physics for the stabilization of these phases is only partially understood.

There are many experimental probes to characterize the SmC* variant phases. Electro-optical [6] measurements were applied to investigate SmC* variant phases soon after their discovery to show the ferro-,ferri- and antiferroelectric switching behavior
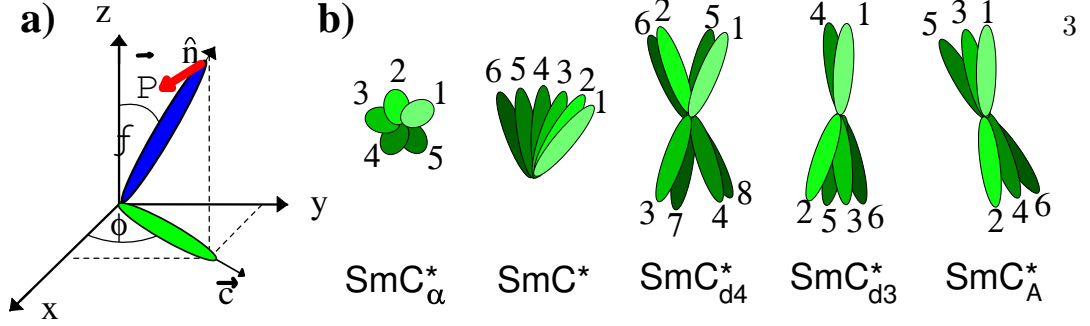
Figure 1.2: (a) Schematic representation of the average molecular tilt in a SmC* layer. θ and ϕ are the tilt and azimuthal angles. (b) From left to right, the SmC$^*_\alpha$, SmC*, SmC$^*_{d4}$, SmC$^*_{d3}$ and SmC$^*_A$ phases. Ellipses, numbered by layer indices, represent the projections of the molecules onto the layer plane. In the SmC$^*_\alpha$ phase, the tilt angle is usually small compared to the other phases.

of these phases. Calorimetry [7, 8] studies were also performed to identify the phase transitions. Ellipsometry [9, 10], depolarized reflected light microscopy[11], dielectric spectroscopy [12], conoscopy [13] have been employed to study the chiral SmC* variant phases. Resonant x-ray diffraction [14, 15] have proven the most powerful tool in revealing the orientational order of the chiral smectic-C phases.

1.3   Free standing films

Many smectic liquid crystals form free standing films. Such films can be prepared by pulling the bulk sample across a film plate with a film hole by a glass spreader, illustrated in Fig. 1.3. There are many advantages of using free standing film for the characterization of the SmC* variant phases. First, the sample preparation is relatively easy. Second, no substrate is needed. Thus, we do not need to worry about the liquid crystal molecules pinned to the substrate. Moreover, in most circumstances, the effect of a substrate on our probe beam, i.e., x-ray or laser can be overwhelming. Third, the layers of the smectic free standing film are quantized with a defined layer normal (perpendicular to the film plate). The layer thickness can be varied from two layers to hundreds of layers by adjusting bulk sample quantity and the spreading speed. In both the optical and x-ray studies, the free standing film geometry is used.
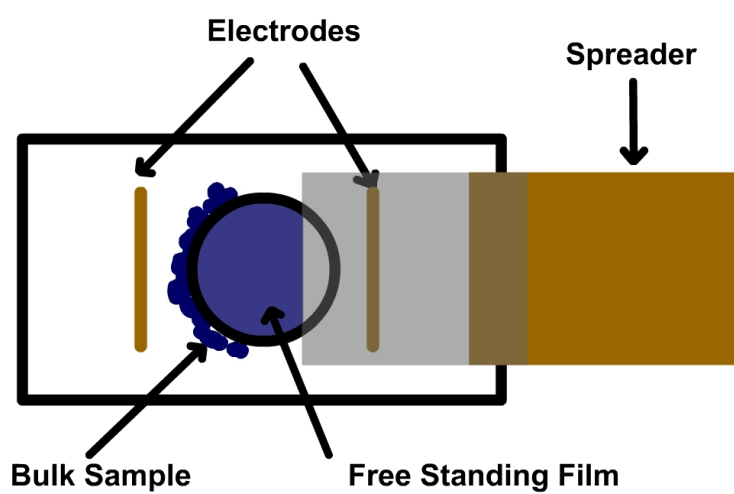
Figure 1.3: Top view of the film plate showing the spreader pulling the liquid crystal sample from the left to the right to form a free standing film.
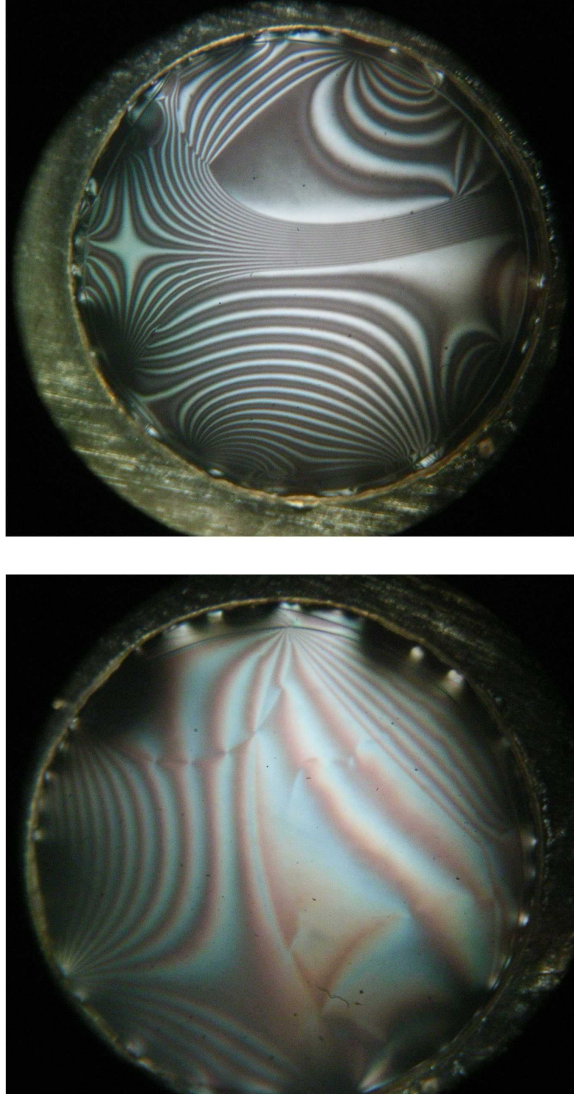
Figure 1.4: Free-standing films of the SmC$^*_{d3}$ and SmC$^*_{d4}$ phases of the 30% C9/70% 12OHF mixture under a polarized optical microscope. The textures are formed because of defects. Defects found in optical microscopy are useful indentifying the SmC* variant phases. However, when performing differential optical reflectivity, it produces noisy singal when the defects move across the laser beam. Thus, a defect free film is highly desirable for differential optical reflectivity measurement.

Chapter 2

Experimental Techniques

There are three major experimental techniques that we use to study the SmC* variant phases. Two of them are optical tools; differential optical reflectivity and null transmission ellipsometry. The principle of these two in-house optical setups is to use polarized light to probe the index of refraction (dielectric constants) of the uniaxial or biaxial films. Because the index of refraction is closely related to the structure of the specific phase, we can identify the phases and their structures. The third experimental technique is called resonant x-ray diffraction. It uses resonant x-rays to reveal orientational order in the SmC* variant phases.

2.1 Differential Optical Reflectivity

2.1.1 Introduction

Differential Optical Reflectivity (DOR) [16] is one in-house optical facility for the identification of the SmC* variant phases and their phase transitions. The experimental setup is shown in Fig. 2.1. The basic idea is to measure the difference of the intensities of the p-polarized (polarization parallel to the incident plane) and s-polarized light (polarization perpendicular to incident plane) reflected from the free standing film. This differential signal is highly sensitive to the biaxiality of the film, which is directly related to the structure of the phase.

The films used in DOR in this thesis usually have thicknesses ranging from 50 to

200 layers unless otherwise specified. The film thickness can be determined precisely by measuring and fitting the reflectivity of a red and a green laser at six different incident angles. However, this procedure is time consuming and requires the parameter n_o (ordinary index of refraction) in the SmA phase of the film which can be extracted from the null transmission ellipsometer [17]. More than twenty mixtures prepared from compounds showing different shapes and physical properties were studied in this thesis. It will take unnecessary long time to determine the thickness of each film. Most importantly, the phase sequence does not depend on the film thickness unless the film is very thin [18]. To preserve time without losing necessary information, no precise thickness measurements were performed for the films in this thesis. The film thickness can be estimated from its reflected color [19], which is sufficient for the purpose of phase identification.
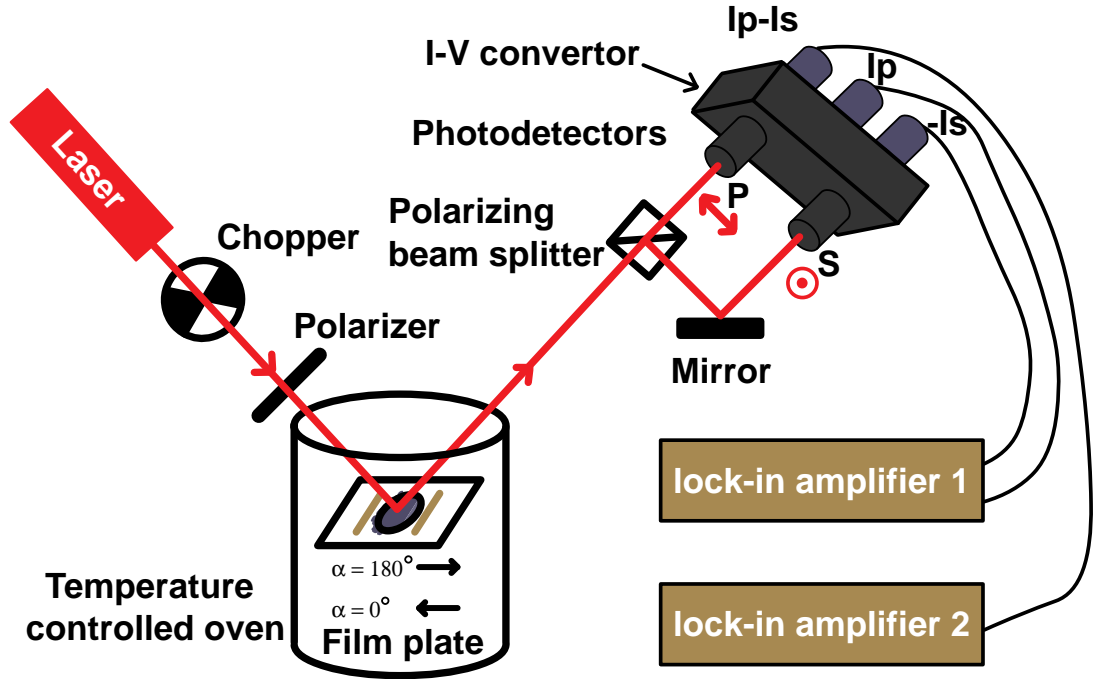
Figure 2.1: Schematic illustration of the experimental setup of DOR.

2.1.2 Experimental setup

Now let us take a look at the schematic diagram. The intensity-stabilized 633 nm He-Ne red laser is chopped at 169 Hz by a mechanical chopper in order for the signal to be analyzed by the lock-in amplifiers. The laser becomes linearly polarized after passing through a Glan-Thompson polarizer. This polarizer is mounted on a rotation stage to change the direction of the polarization of the incident light. The beam is then directed toward the film. The reflected light is split into two beams with p- and s-polarization by a polarizing beam splitter. The intensities of these two beams are detected by two silicon photodetectors. Signals from the detectors are immediately subtracted and converted to voltage by an I-V converter. This voltage is read by a lock-in amplifier which locks to the frequency of the chopper. This differential signal is called I_p-I_s. The I-V converter also outputs I_p and -I_s voltage. These two voltages are read by another lock-in and I_p+I_s is be obtained. I_p+I_s is just the total reflected intensity of the film, which gives the information about the optical thickness of the film.

The glass film plate (made by sandblasting a microscope slide cover glass) is placed in a temperature-controlled two-stage oven with stability of $\pm0.02°C$. There are two electrodes glued to the bottom of the film plate. By applying a weak electric field of about $2V/cm$ in the plane of the film, we can align the polarization of the film. The orientation of the field is defined as $\alpha = 180°$ (left to right in the film plane) and $\alpha = 0°$ (right to left in the film plane). The film is usually prepared in its SmA phase. After the film becomes uniform, we adjust the polarization of the incident light by rotating the Glan-Thompson polarizer so that in the SmA phase, the I_p-I_s is zero. The advantage of doing this is that the signal becomes only sensitive to changes in the reflected polarization state, while common-mode intensity fluctuations are significantly reduced. The oven is cooled down to the desired temperature with a rate of 0.05-$0.1°C/min$ while the electric field is set at $\alpha = 180°$. Then it is heated up from the lowest temperature back to the SmA phase. After one thermal cycle is finished, the orientation of the electric field is flipped to $\alpha = 0°$. The thermal cycle is repeated once again. The data from the $\alpha = 180°$ and $\alpha = 0°$ cycles provide the information about the symmetries of the phases. More detailed information about how to operate the DOR is provided in the theses of Dr. Pankratz, Dr. Cady and Dr. Liu [20, 21, 22].

2.1.3 Data
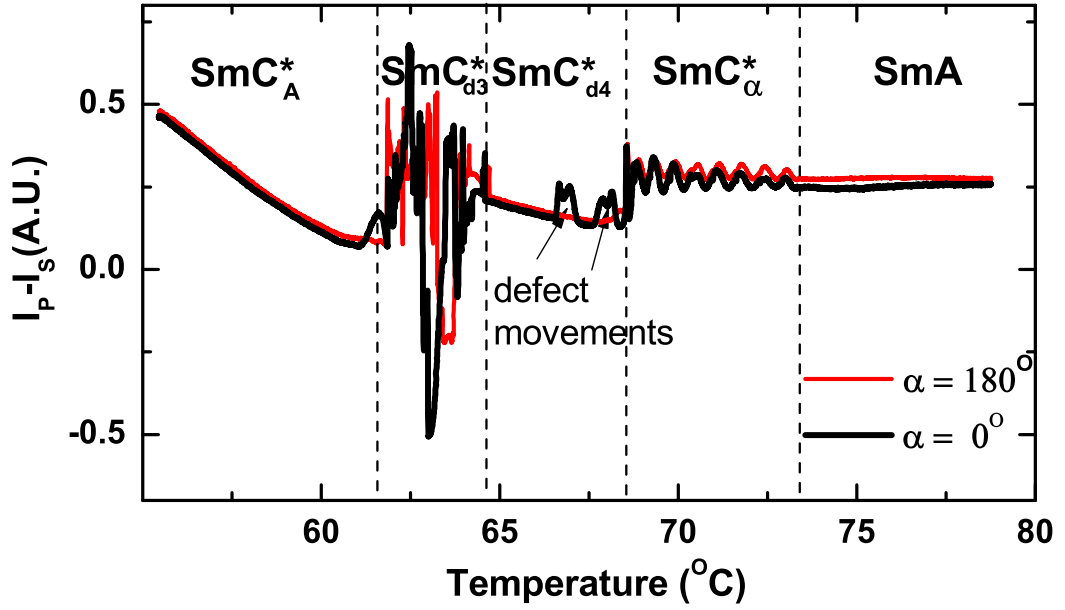
Figure 2.2: I_p-I_s vs. temperature plot for a film of 1%8̄S5 in MHPBC.

Figure 2.2 displays an example of I_p-I_s vs. temperature scan taken upon cooling. I will talk briefly about how to identify the phases from the data. In the SmA phase, because molecules are not tilted, the data from $\alpha = 180°$ and $\alpha = 0°$ almost overlap. The small difference between the two is due to the surface-induced synclinic tilted layer in the film-air interfaces. In smectic liquid crystals, the surface transition temperature is always higher than the bulk [23, 24]. The SmC$_\alpha^*$ phase is optically uniaxial because its helical pitch in this phase (below 60 nm) is much smaller than the wavelength of the laser (633 nm). Thus it is impossible to discriminate the SmC$_\alpha^*$ phase and the SmA phase using a polarized optical microscope. In the freestanding film geometry, the surface layers provide the biaxiality needed to probe the structure of the SmC$_\alpha^*$ phase. As the short helical pitch in the SmC$_\alpha^*$ phase evolves with temperature, the surface layers rotate about the layer normal. This rotation is picked up by DOR as a characteristic oscillation of I_p-I_s due to the change of the polarization of the reflected

light as shown in Fig. 2.2 [17]. Upon entering the SmC^*_{d4} phase, the I_p-I_s signal usually shows a step. The SmC^*_{d4} phase has $180°$ rotational symmetry. So I_p-I_s does not change when the electric field is flipped from $\alpha = 180°$ to $\alpha = 0°$. Two bumps in the $\alpha = 0°$ data are caused by the movement of defects in the film. The SmC^*_{d3} phase is always full of defects as shown in Fig. 1.4. I_p-I_s always show a non-repeatable noisy signal in the SmC^*_{d3} phase. The SmC^*_A phase has the same symmetry as the SmC^*_{d4} phase. In principle, we could not distinguish the two by DOR. Fortunately, the SmC^*_A phase is always displayed at a lower temperature than the SmC^*_{d4} phase. Most of the time the SmC^*_A and SmC^*_{d4} phases are separated by the noisy SmC^*_{d3} phase in the mixtures studied in this thesis. Thus, we can use this reasoning to determine the SmC^*_A phase.

2.2   Null Transmission Ellipsometry

Since Null Transmission Ellipsometry (NTE) is very similar to DOR, it is only introduced briefly here. More details can be found in Ref [45]. Ellipsometry usually measures two parameters of the free standing liquid crystal film, (1) the amount of the polarization rotated by the film and (2) the phase lag of the p-polarized and s-polarized light after passing through the film. In NTE, we measure two parameters; Δ and Ψ. Δ is the phase shift between the p- and s-components of the incident light necessary to make the transmitted light to be linearly polarized at an angle $\Psi+90°$. Our NTE is a little different from a traditional ellipsometer in the sense that it actually does the measurement "backwards". The experimental apparatus of NTE is shown in Fig. 2.3. The incident linearly polarized He-Ne laser light passes through a quarter-wave plate and becomes circularly polarized. The beam then passes through a chopper, a polarizer and a compensator before transmitting the film at $45°$. The compensator is another quarter-wave plate, its optical axis being oriented at $-45°$ from to the p-axis. Positive angles are defined as clockwise when looking along the direction in which the light is traveling. The transmitted beam then reaches a silicon photodetector through an analyzer. The orientation of the polarizer and analyzer are rotated until a null signal is obtained at the detector. The two parameters are identified in the following way, Δ = $-2P_n+90°$ and $\Psi = A_n$. P_n and A_n are the angles of the polarizer and analyzer relative to the p-axis that give the zero transmitted intensity of the laser beam at the

detector. In this thesis, only the Δ is shown because the two parameters give similar information and the data from Δ measurement usually have lower noise-to-signal ratios. The film plate of NTE is constructed differently from that of DOR. Instead of having two electrodes to align the net polarization of the film, NTE has eight. The advantage is that in NTE the angle α, defined as the angle between electric field and the incident plane, can be set to any desired direction. Both ellipsometric parameters, Δ and Ψ, can be acquired as a function of α at a fixed sample temperature. As a result, NTE could determine the symmetry of the phase better than DOR. The data upon cooling and heating are taken in the same fashion as DOR.
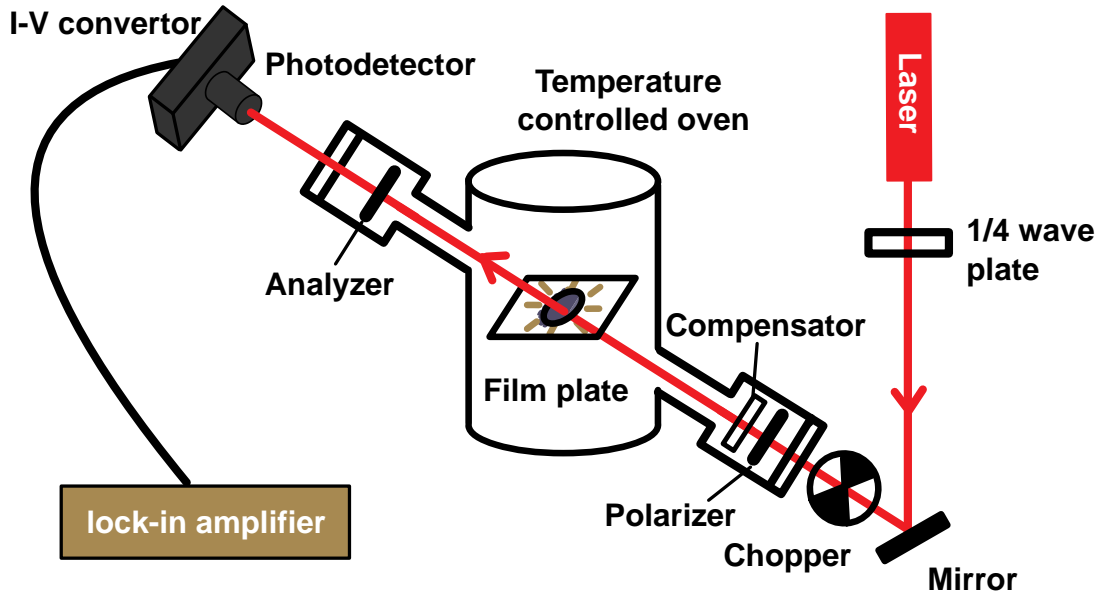
Figure 2.3: Experimental setup of NTE.

2.3 Resonant X-ray Diffraction

2.3.1 Principle of resonant x-ray diffraction

X-ray diffraction (XRD) is widely used for the determination of microscale or nanoscale structures such as averaged particle sizes, particle shapes, particle distribution, and

surface-to-volume ratio in condensed matter physics. XRD has been used to study the chiral SmC* variant phases as well. Possible phase transitions can be identified from the layer spacing vs. temperature measurement. For example, the layer spacing usually decreases at the transition from the SmA to any chiral SmC* phase. Because the transitions between the chiral SmC* phases are usually first order, the layer spacing might display a discontinuity. From the fitting of the Bragg peaks, more information regarding the smectic order can be extracted. It was found that the antiferroelectric SmC*$_A$ phase has much higher smectic order than the ferroelectric SmC* phase [4]. Although the conventional XRD has been useful in probing the chiral SmC* variant phases, the results are not conclusive because conventional XRD lacks the ability to reveal the orientational order, which is the most important feature for the chiral SmC* variant phases.

Resonant x-ray diffraction (RXRD) [14, 15] solves the problem. There are two components of the atomic scattering factor that link the intensity of the diffracted beam to the incident one [26]. The usual scattering factor F which adds the contribution from atoms in the whole molecule is a scalar, and thus not sensitive to the orientational order. However, there is an atomic scattering factor $\bar{f}$ due to the resonant atom, which is a rank-2 tensor. It is related to the orientation of the valence orbitals of the resonant atom within the molecule. It becomes nonzero only within a narrow energy band near the absorption edge. Therefore, the scattering signal becomes sensitive to the orientational order of the molecules close to the resonant energy.

Experimentally, resonant satellite peaks show up in addition to the Bragg peaks [27]. From the positions and shapes of these peaks, the orientational order of the chiral SmC* variant phases can be determined. More specifically, for a structure with n-layer periodicity, in addition to principal peaks at $Q_z/Q_0 = l$ ($l = 1, 2, ...$) there are satellite peaks ($m = \pm1, \pm2$) at $Q_z/Q_0 = l + m$ ($1/n \pm \epsilon$). $Q_0 = 2\pi/d$ and d is the layer spacing. $\epsilon = 2\pi/p$ where p is the optical pitch. Thus, from the data, information about the layer spacing and pitch (related to n) can be obtained.

2.3.2 Experimental setup

RXRD experiments were conducted at Beamline X19A at National Synchrotron Light Source (NSLS), Brookhaven National Lab. The beamline with low soft x-ray energy
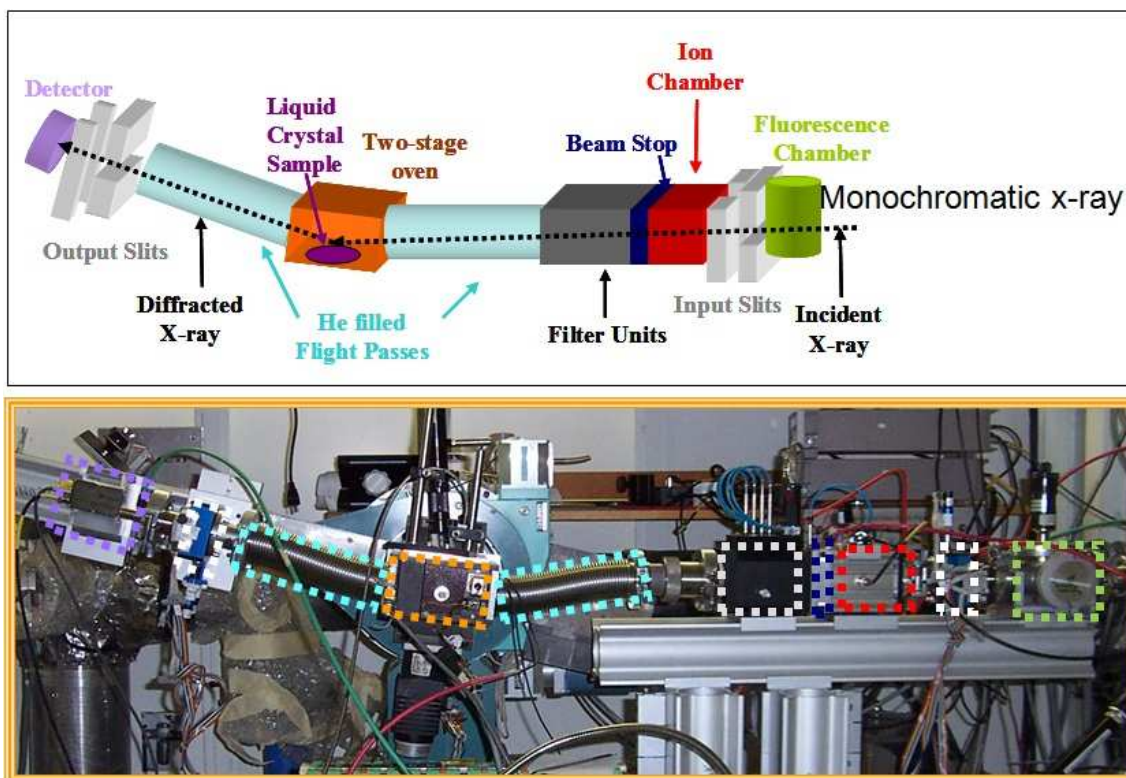
Figure 2.4: (Top) Schematic diagram of components in the RXRD experiment. (Bottom) The experimental setup at Beamline X19A, NSLS, Brookhaven National Lab.

and high energy resolution provides access to the resonant energy near the K_α edge of the sulfur atom in the liquid crystal compounds.

Figure 2.4 illustrates the RXRD setup. The monochromatic x-ray first passes a fluorescence chamber. This chamber is used to determine the resonant energy of the sulfur atom in the studied compounds. Figure 2.5 shows an example of the fluorescence scan. It enables us to measure the sulfur K-edge absorption peaks for the studied compounds by monitoring the fluorescence intensity as a function of incident beam energy. The principal maximum E_0 in 10OTBBB1M7(C10) occurs at 2.473 keV. The input slits after the fluorescence chamber define the dimension of the x-ray beam. The size of the beam is usually set to be 1 mm (horizontal) by 0.5 mm(vertical). Exiting the input slits, the beam passes an ion chamber, a beam stop and an attenuator. The
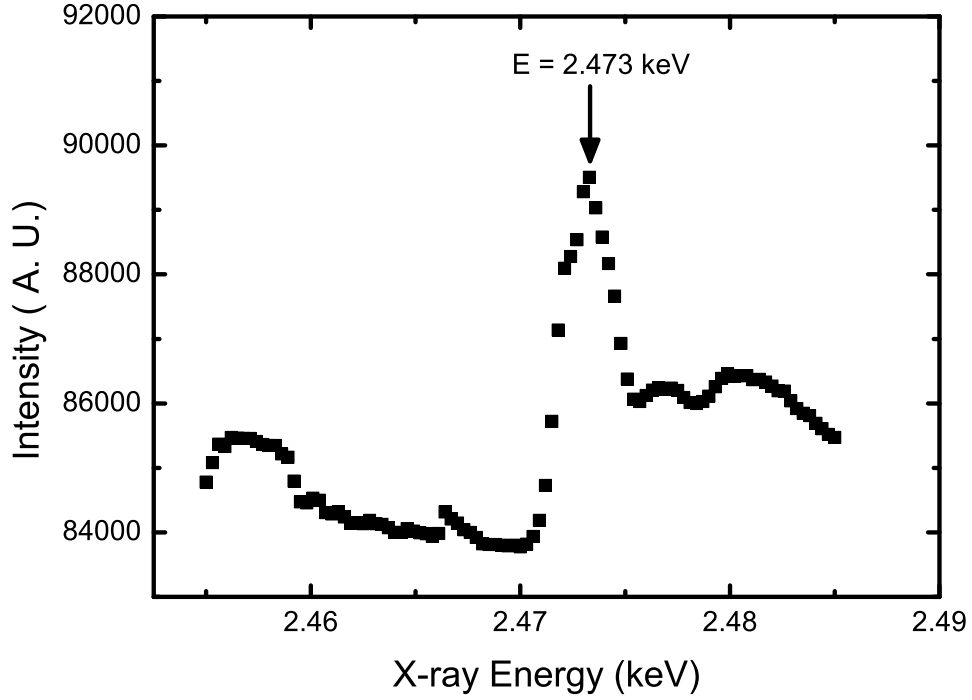
Figure 2.5: Fluorescence intensity vs. x-ray beam energy incident onto bulk 10OTBBB1M7(C10) powder sample.

ion chamber monitors the x-ray intensity, which can be used to normalize the scattering intensity. Such normalization will minimize the effect of any drift in the x-ray intensity. The attenuator is composed of four filters, each of which reduces the x-ray intensity by a factor of two. Therefore, we can use less intense x-rays if allowed to protect the sample from unnecessary exposure which will lead to the decomposition of the organic liquid crystal compounds. The liquid crystal is in free standing film geometry prepared in a two-stage temperature controlled oven, connected to the attenuator by flexible bellows. The x-ray diffracts off the film and reaches a detector through an output slit. The output slit and the oven are also linked by flexible bellows. The oven and the detector are mounted on the θ and 2θ circles of a Huber two-circle goniometer, respectively. The whole x-ray flight path as well as the oven are properly connected and constantly flushed
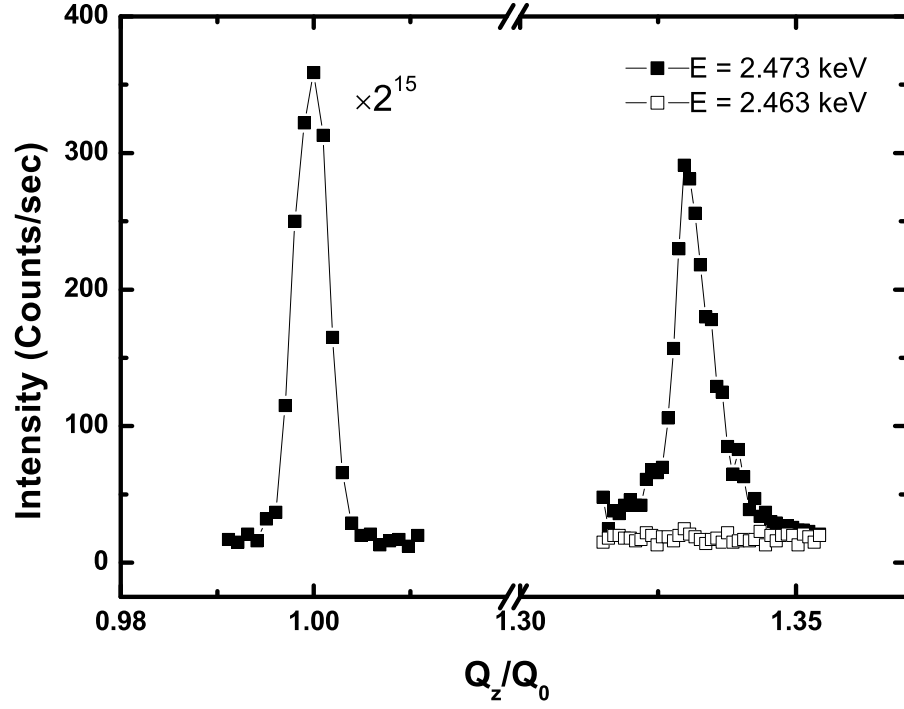
Figure 2.6: X-ray intensity scan in the SmC$^*_{d3}$ phase of C10. The l=1 Bragg peak and the ($l = 1$, $m = 1$) resonant peak are shown.

with helium to minimize sample deterioration and x-ray absorption by air.

There is a window on the top of the oven through which the film can be observed, either by eye or by a CCD camera through a long working distance microscope. To obtain a good diffraction signal, the thickness of the film should exceed five hundred layers. Sometimes, films of thousands of layers are spread in order to obtain resonant peaks with sufficient intensity. The color of a thick enough film should be white with thickness lines. Unlike DOR and NTE, the RXRD experiment does not require a uniform film.
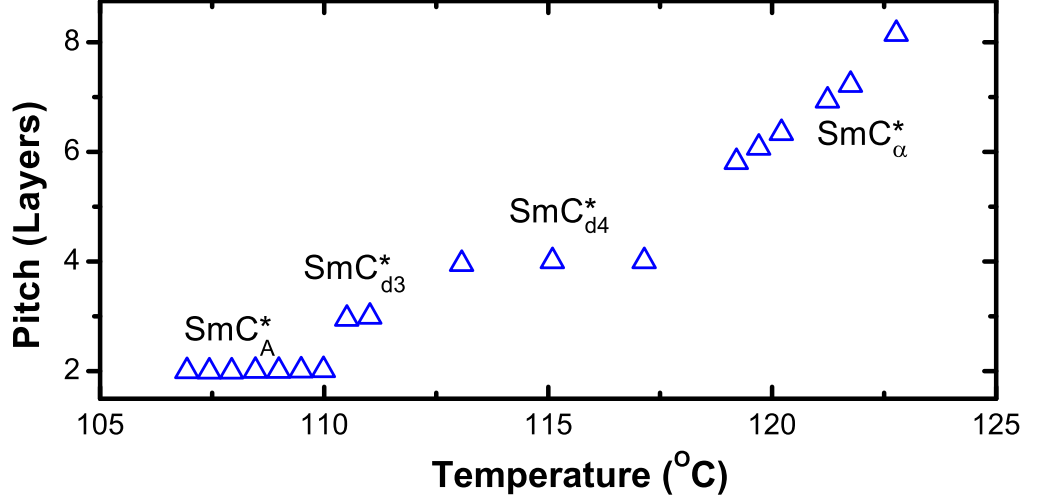
Figure 2.7: The pitch vs. temperature plot for C10.

2.3.3 Data

At the beginning of each RXRD run, we usually use an nOTBBB1M7(Cn) compound to fine-tune the alignment and test the system. Results from test run of C10 are shown here as an example of the RXRD data. Figure 2.6 shows the Bragg peak and the resonant peak in the SmC^*_{d3} phase of C10. The resonant peak shows up at $Q_z/Q_0 = 1.333$, corresponding to $l = 1$, $n = 3$, $m = 1$. It gives the periodicity or pitch of the SmC^*_{d3} phase to be three layers. When the x-ray energy is tuned 10 eV away from the resonant energy, the resonant peak disappears. This demonstrates the resonant nature of the satellite peak. Figure 2.7 shows the pitch measurement for C10. From this plot, all the phases in C10 can be identified unambiguously. Note that each of the data points takes about 30 minutes because the time needed for the temperature stabilization as well as the scans of the principal Bragg and resonant peaks. For the limited synchrotron time, it is usually impossible to have extremely high data density. In order to determine the transition temperatures accurately, usually we need to combine the results from RXRD and DOR. DOR provides continuous data acquisition. These two experimental techniques are complementary to each other.

Chapter 3

A Reversed Phase Sequence

3.1 The SmC_α^*-SmC_{d4}^*-SmC^* phase sequence

Among antiferroelectric liquid crystal compounds, a typical order of appearance of mesophases on cooling is the following: SmA-SmC_α^*-SmC^*-SmC_{d4}^*-SmC_{d3}^*-SmC_A^*, with some of these phases missing in many compounds. Laux *et al.* [28] have reported a unique phase sequence SmC_α^*-SmC_{FI}^*-SmC^* upon cooling in nOHFBBB1M7 (n=10), 10OHF. Wang *et al.* [29] identified the phase sequence of 10OHF to be SmC_α^*-SmC_{d4}^*-SmC^*. It was demonstrated by Sandhya *et al.* [30] that the SmC_{d4}^* phase was thermodynamically monotropic and only appeared upon cooling. They also showed that the SmC_{d4}^* phase was unstable under bias voltage. It was found that in binary mixtures of 10OHF and nOTBBB1M7 (n=9), C9, the SmC_{d4}^* temperature window expanded rapidly with increasing concentration of C9 and the SmC_{d4}^* phase became thermotropic [29, 30]. Binary mixtures of 10OHF and C11 showed similar behavior. The SmC^* phase found in both compounds was squeezed out and the SmC_{d4}^* phase was stabilized. The phase reversal phenomenon has also been observed in other liquid crystal compounds [31]. The other homologs of 10OHF (namely, 9-, 11- and 12OHF) do not show reversed phase sequence behavior [32]. The chemical structures and transition temperatures of nOHF and Cn are displayed in Fig 3.1.

In this chapter, NTE and DOR are employed to investigate samples of 10OHF doped with its homologs. The result shows that the reversed phase sequence disappeared with moderate dopant concentrations. For further study, we select the 73% 10OHF/27%
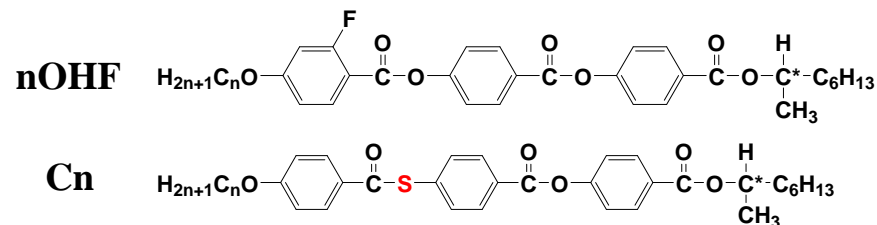
17

Figure 3.1: Chemical structures and transition temperatures of nOHF and Cn.

11OHF binary mixture, which does not show the SmC^*_{d4} phase. By adding C9 into this particular mixture, the reversed phase sequence is revived. For a given concentration of C9, in the ternary 10OHF/11OHF/C9 mixtures, SmC^*_{d4} temperature windows are found to be larger than in the corresponding 10OHF/C9 binary mixtures [33].

3.2 The mixtures of 10OHF and its homologs

3.2.1 Mixtures of 10OHF and 9OHF

We have studied three mixtures of 10OHF/9OHF (15%, 29% and 50% of 9OHF), three mixtures of 10OHF/11OHF (15%, 25% and 27% of 11OHF) and two mixtures of 10OHF/12OHF (15% and 25% of 12OHF). Three of these mixtures are characterized by NTE. They are 90% 10OHF/10% 9OHF, 85% 10OHF/15% 11OHF and 75% 10OHF/25% 11OHF. The rest are studied by DOR.

Let us look at the 9OHF/10OHF mixtures first. Figure 3.2 illustrates the ellipsometric parameter (Δ_{90}, Δ_{270}) obtained from NTE temperature scans of a film of 85% 10OHF with 15% 9OHF at $\alpha=90°$ and $\alpha=270°$. Upon cooling, the small difference between Δ_{90} and Δ_{270} above T_1 is due to surface ordering in the SmA phase. The oscillations of Δ_{90} and Δ_{270} between T_1 and T_2 are signatures of the SmC$_\alpha^*$ phase [25]. Between T_2 and T_3 is the SmC$_{d4}^*$ phase. At T=70°C the ellipsometric parameters Ψ and Δ were obtained as a function of α. The data show that Ψ and Δ have 180° symmetry, which is the characteristic of the SmC$_{d4}^*$ phase [10]. Below T_3 the large span of Δ between $\alpha=90°$ and $\alpha=270°$ is the feature of the SmC* phase [34]. The phase sequence of this mixture upon cooling is SmA (83.1°C) SmC$_\alpha^*$ (72.1°C) SmC$_{d4}^*$ (64.3°C) SmC*. We can see that all the transition temperatures decreases compared to the pure 10OHF, which is not surprising because 9OHF has lower transition temperatures than 10OHF. The temperature window of the SmC$_\alpha^*$ phase in this mixture is about the same as 10OHF. The temperature range of the SmC$_{d4}^*$ decreases from 8 to 6 degrees.

Upon heating, the phase sequence is SmC*(70.6°C) SmC$_\alpha^*$ (81.9°C) SmA. The SmC$_{d4}^*$ phase disappears on heating in this mixture. This monotropic behavior of the SmC$_{d4}^*$ phase in this mixture is the same as in pure 10OHF. In fact, in all the mixtures of 10OHF and its homologs, the SmC$_{d4}^*$ phase (if they show any) is monotropic. Therefore, for the rest of the mixtures we will only show the cooling data. The doping effects of 9-,11- and 12-OHF are different from that of C9 and C11, in which the SmC$_{d4}^*$ phase becomes thermotropic (appears on both cooling and heating) [29, 32].
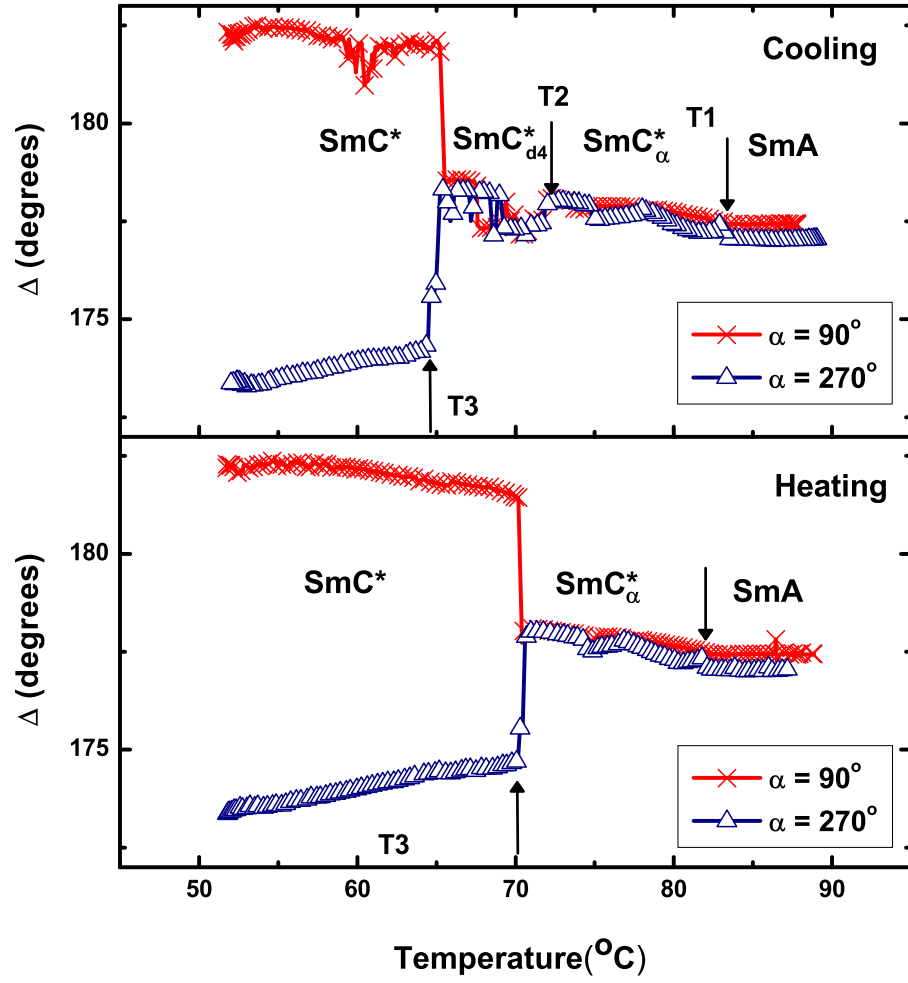
Figure 3.2: Δ as a function of temperature for a film of the 85% 10OHF/15% 9OHF mixture from NTE while cooling (top) and heating(bottom) at 0.1°C/min. α is the angle between the **E** orientation and the incident plane of the laser light. The thickness of this film is 56 layers.

Figure 3.3: I_p-I_s and I_p+I_s as a function of temperature for a film of the 70% 10OHF/30% 9OHF mixture from DOR while cooling at 0.1°C/min. Arrows mark the transition temperatures. The thickness of this film is more than 300 layers.

Figure 3.4: I_p-I_s and I_p+I_s as a function of temperature for a film of the 70% 10OHF/30% 9OHF mixture from DOR while cooling at 0.1°C/min. Arrows mark the transition temperatures. The thickness of this film is about 50 layers.

The phase sequence of the 70% 10OHF/30% 9OHF mixture is the same as the 85% 10OHF/15% 9OHF mixture. The transition temperatures are SmA (80.7°C) SmC$_\alpha^*$ (68.1°C) SmC$_{d4}^*$ (65.5°C) SmC*. The DOR temperature scans of a film (about 300 layers) of the 70% 10OHF/30% 9OHF mixture are shown in Fig. 3.3. The oscillations in I$_p$-I$_s$ in the SmC$_\alpha^*$ are interesting because the amplitude of one oscillation between 72.4 °C and 70.4 °C is very small. This behavior could be explained by the nonmonotonic pitch evolution with temperature. However, the period of this oscillation is about the same as the previous and next one, which suggests that the temperature derivative of pitch is almost constant in this mixture. Another explanation is that the biaxiality of the surface layers somehow does not change much during this oscillation. This behavior is not observed in thinner films (see Fig. 3.4). In the SmC* phase, a "pitch reversal" happens at T = 58 °C. The I$_p$-I$_s$ shows a discontinuity. Interestingly, the $\alpha = 0°$ ($\alpha = 180°$) signal looks like a continuation of $\alpha = 180°$ ($\alpha = 0°$) from the high temperature. The reason for this is that the pitch changes sign at T = 58 °C. At SmA-SmC$_\alpha^*$ transition, the I$_p$+I$_s$ signal decreases because the molecules starts to tilt. Discontinuity is observed at both SmC$_\alpha^*$-SmC$_{d4}^*$ and SmC$_{d4}^*$-SmC* transition, which implies potential layer spacing change.

The DOR temperature scan of a film of the 50% 10OHF/50% 9OHF mixture is shown in Fig. 3.5. The oscillations in the SmC$_\alpha^*$ phase again show the strange feature in the amplitude. The SmC$_{d4}^*$ phase is gone is this mixture. Thus the reversed phase sequence is unstable upon doping with 9OHF.

Figure 3.5: I_p-I_s and I_p+I_s as a function of temperature for a film of the 50% 10OHF/50% 9OHF mixture from DOR while cooling at 0.1°C/min. Arrows mark the transition temperatures. The thickness of the film is about 200 layers.
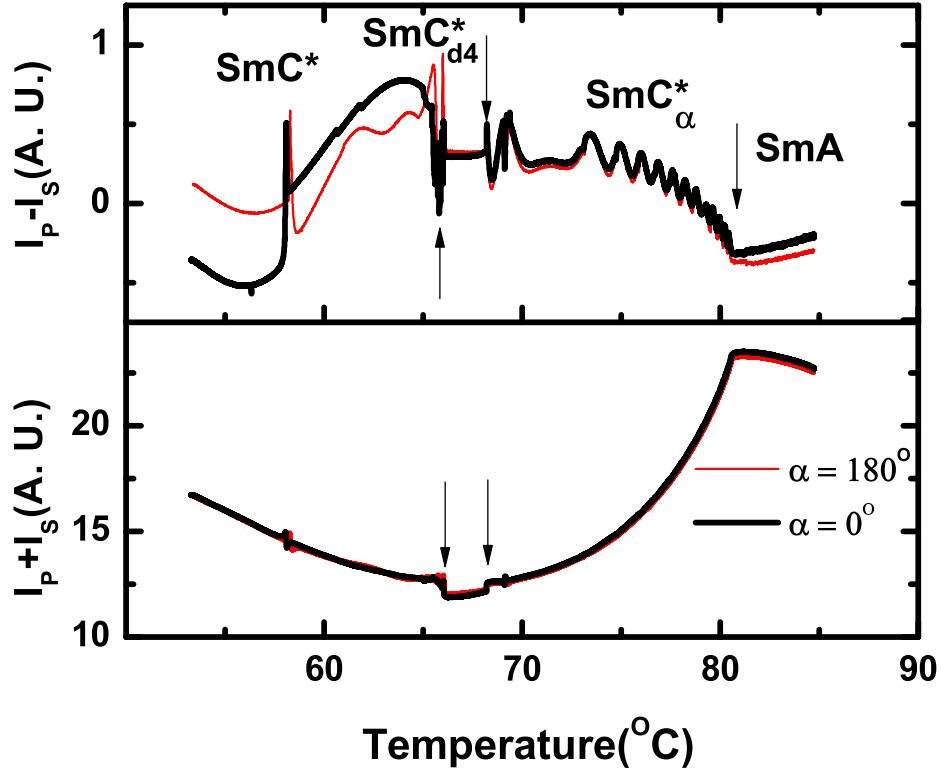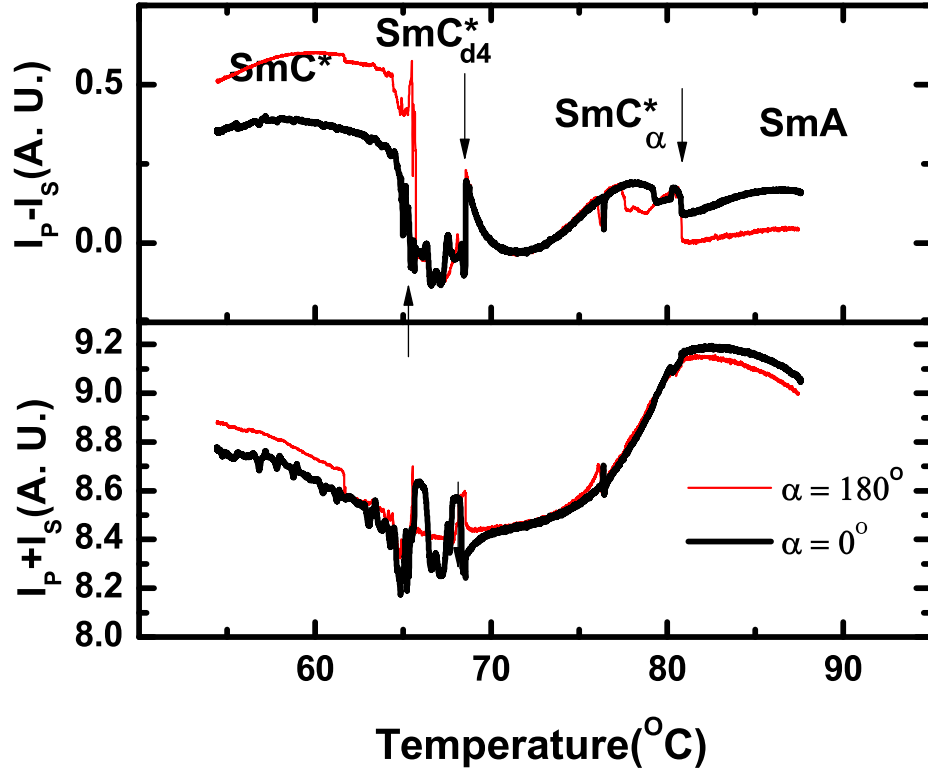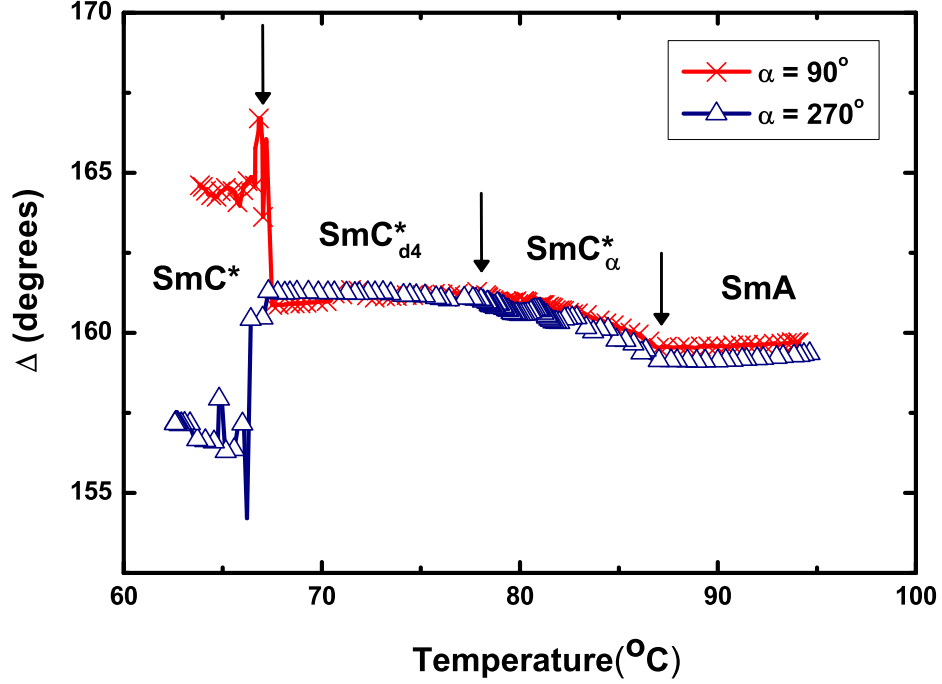
Figure 3.6: Δ as a function of temperature for a film of the 90% 10OHF/10% 11OHF mixture from NTE while cooling at $0.1°C/min$. Arrows mark the transition temperatures. The thickness of the film is 120 layers

3.2.2 Mixtures of 10OHF and 11OHF

The 10OHF/11OHF mixtures show very similar behavior as the 10OHF/9OHF mixtures. Figure 3.6 displays the NTE temperature scan for a film of 90% 10OHF/10% 11OHF mixture. The phase sequence is SmA (87.5°C) SmC_α^* (77.3°C) SmC_{d4}^* (67.1°C) SmC*. The SmA-SmC_α^* and SmC_α^*-SmC_{d4}^* transition temperatures increase because 11OHF has a higher SmA-SmC_α transition temperatures than 10OHF. Surprisingly, the SmC_{d4}^*-SmC* transition temperature in this mixture is lower than in the pure 10OHF. As a result, the temperature range of the SmC_{d4}^* phase is slightly larger in this 90% 10OHF/10% 11OHF mixture than in pure 10OHF, which is different from all the other mixtures of 10OHF and its homologs.

The NTE temperature scan for a film of the 75% 10OHF/25% 11OHF mixture is illustrated in Fig. 3.7. The temperature range of the SmC_{d4}^* phase drops to only 1.4 K
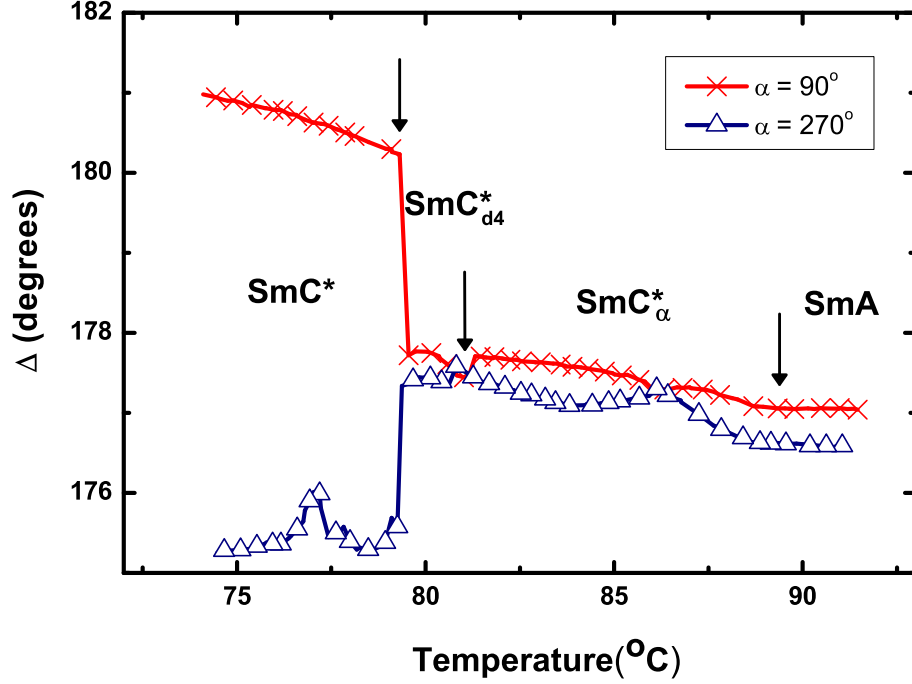
Figure 3.7: Δ as a function of temperature for a film of the 75% 10OHF/25% 11OHF mixture from NTE while cooling at 0.1°C/min. Arrows mark the transition temperatures. The thickness of the film is 56 layers.

in this mixture.

In order to see at what doping concentration the SmC$^*_{d4}$ phase disappears, we made another mixture of 73% 10OHF/27% 11OHF. The DOR scan of this mixture is shown in Fig. 3.8. There exists no SmC$^*_{d4}$ phase in this mixture. Thus, the transition temperatures of the 75% 10OHF/25% 11OHF and 73% 10OHF/27% 11OHF mixture yield a well-defined boundary of the SmC$^*_{d4}$ phase in the 10OHF/11OHF phase diagram.

3.2.3 Mixtures of 10OHF and 12OHF

The DOR data of the two 10OHF/12OHF mixtures are shown in Fig. 3.9 and 3.10. The temperature range of the SmC$^*_{d4}$ phase decreases.

To summarize, a phase diagram of 10OHF/9OHF and 10OHF/11OHF mixtures is

shown in Fig. 3.11. The SmC^*_{d4} phases in all the mixtures are monotropic. The temperature window of the SmC^*_{d4} phase decreases with increasing 9OHF concentration. There is no SmC^*_{d4} phase observed in the 50% 9OHF/50% 10OHF mixture. The stability of the SmC^*_{d4} phase increases slightly with 10% 11OHF doping. However, for 25% 11OHF doping, the temperature window of the SmC^*_{d4} phase decreases dramatically to 1.4 degrees. For the 73% 10OHF/27% 11OHF mixture, the SmC^*_{d4} phase completely disappeared. A phase diagram of 10OHF/12OHF mixtures is shown in Fig. 3.12. Similar to 10OHF/11OHF mixtures, the SmC^*_{d4} phase disappears at 25% dopant concentration.
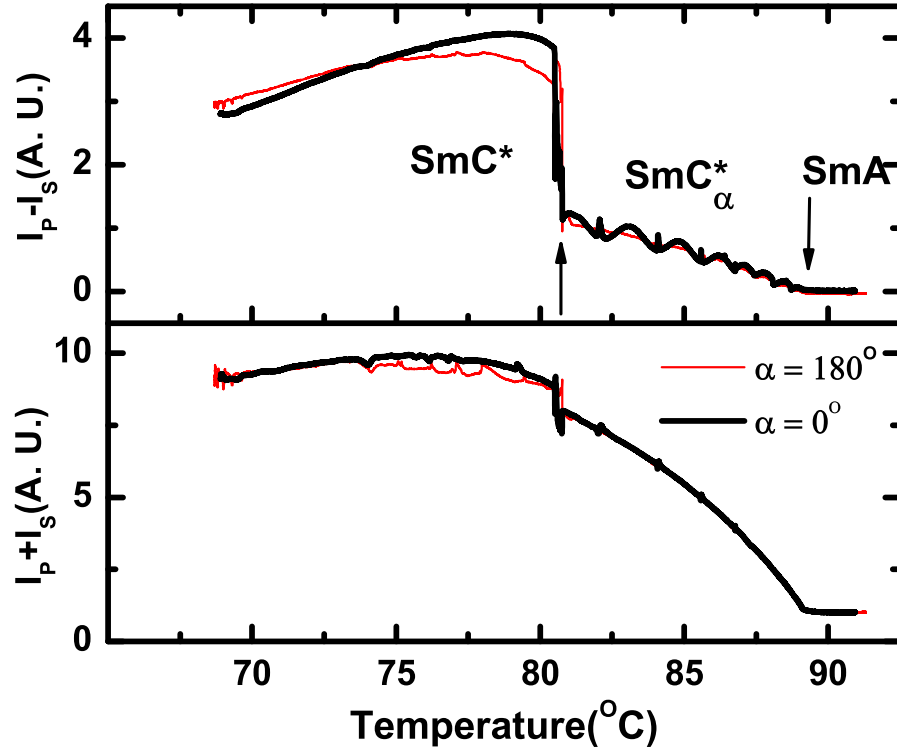
Figure 3.8: I_p-I_s and I_p+I_s as a function of temperature for a film of the 73% 10OHF/27% 11OHF mixture from DOR while cooling at 0.1°C/min. Arrows mark the transition temperatures. The thickness of the film is about 200 layers.
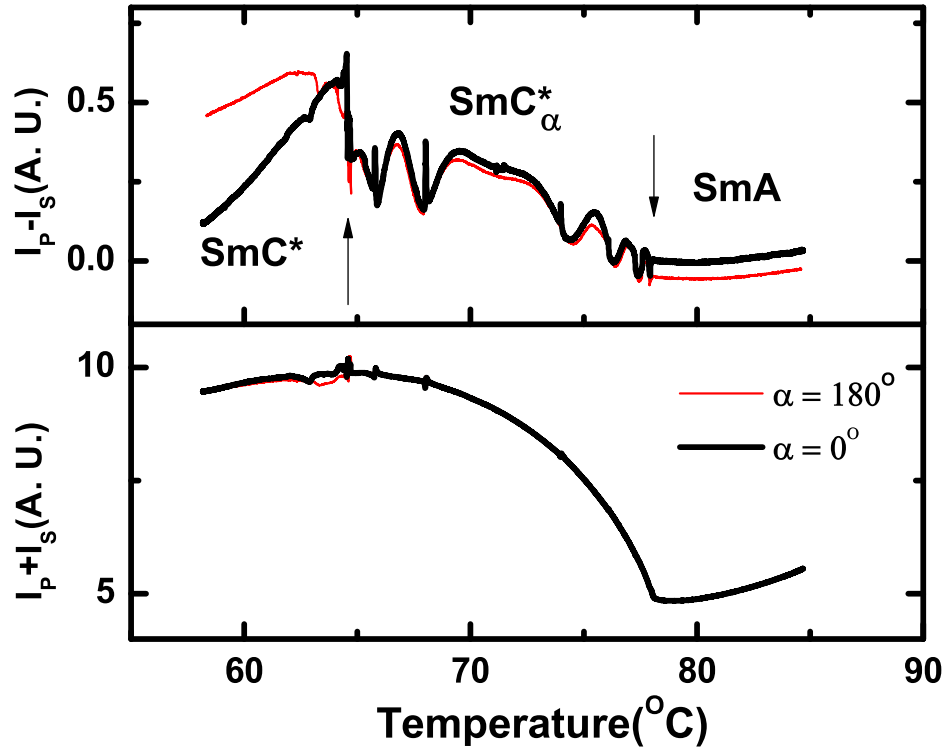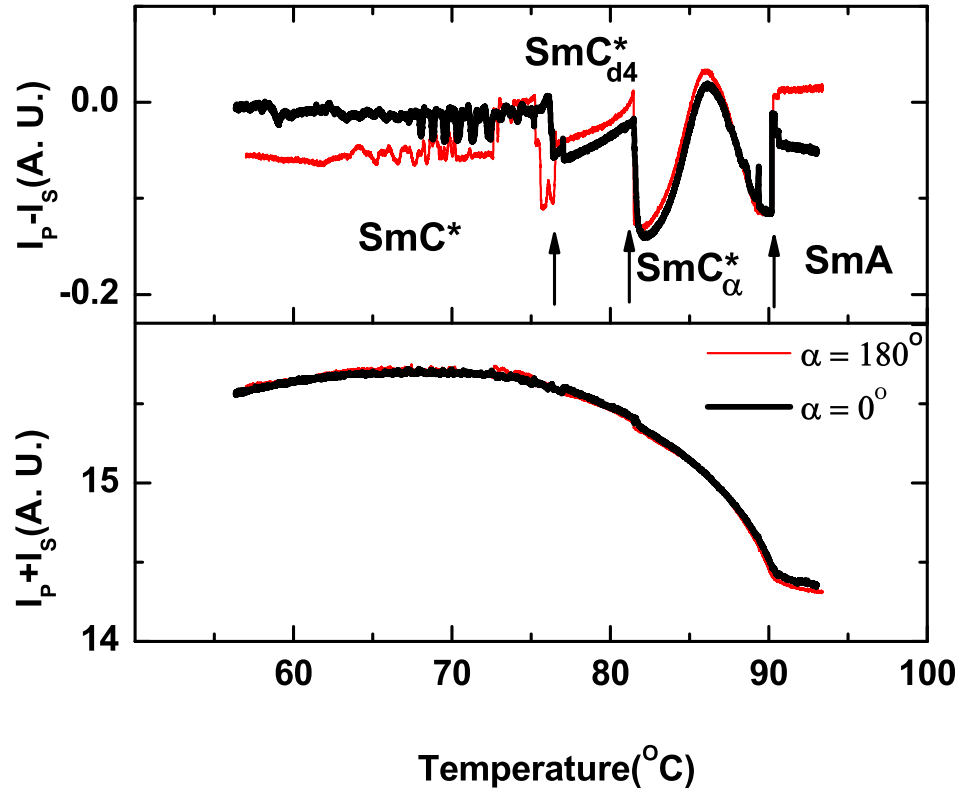
Figure 3.9: I_p-I_s and I_p+I_s as a function of temperature for a film of the 85% 10OHF/15% 12OHF mixture from DOR while cooling at 0.1°C/min. Arrows mark the transition temperatures. The thickness of the film is about 50 layers.
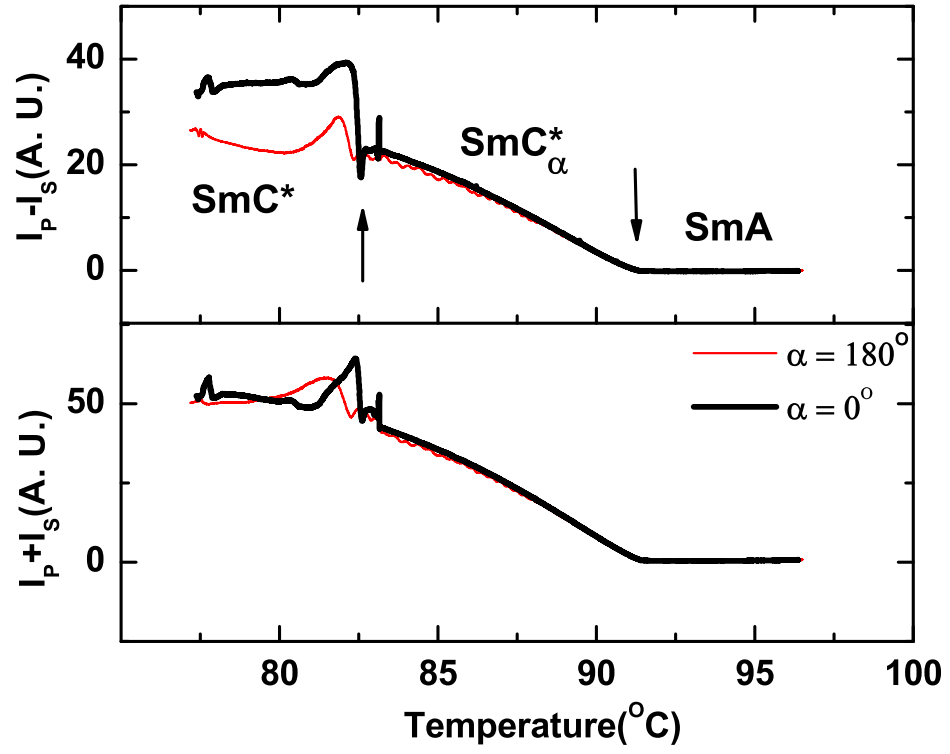
Figure 3.10: I_p-I_s and I_p+I_s as a function of temperature for a film of the 75% 10OHF/25% 12OHF mixture from DOR while cooling at $0.1°C/min$. Arrows mark the transition temperatures. The thickness of the film is more than 200 layers.
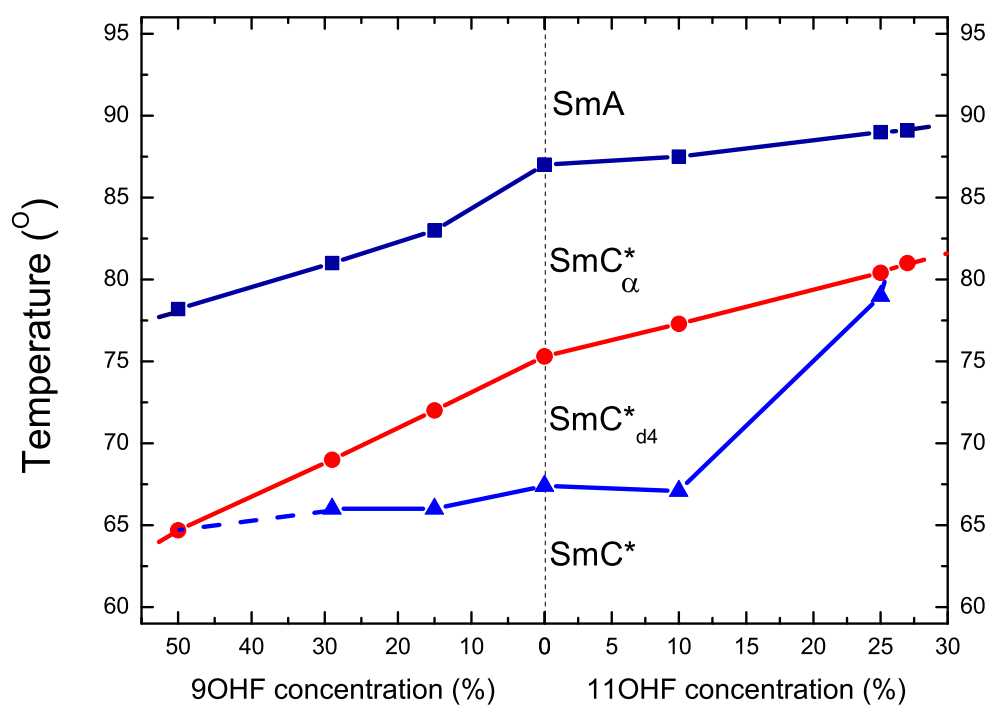
Figure 3.11: Phase diagram of $10OHF_{1-u}$ $9OHF_u$ and $10OHF_{1-v}$ $11OHF_v$ mixtures.
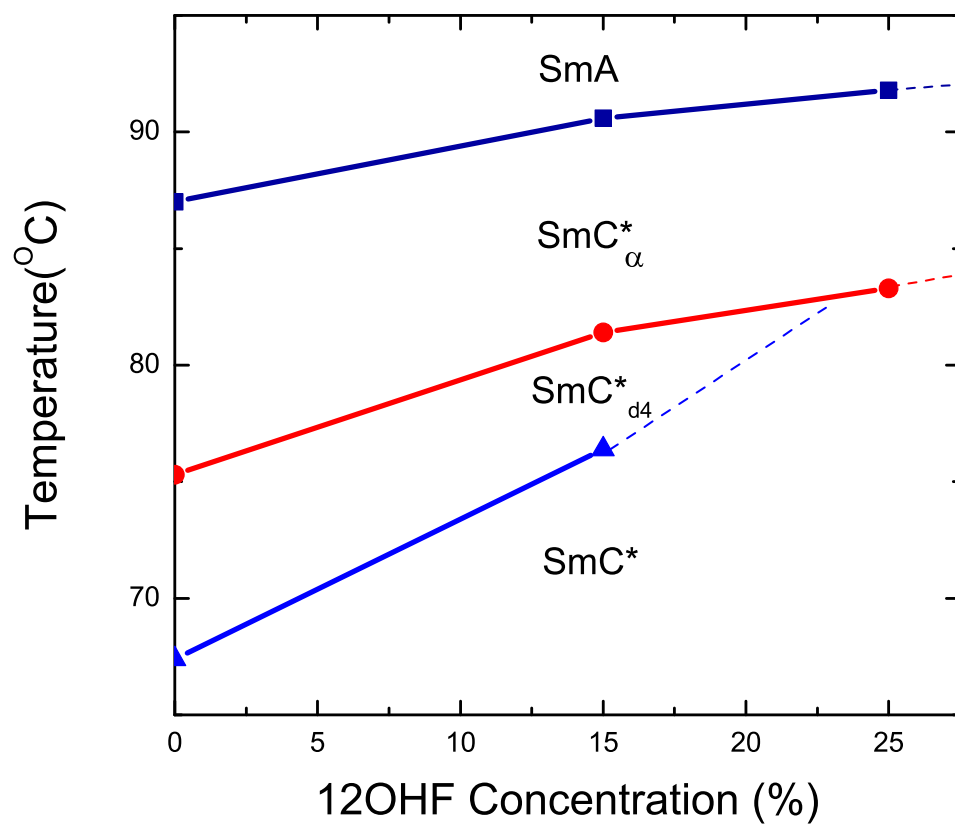
Figure 3.12: Phase diagram of $10\mathrm{OHF}_{1-u}$ $12\mathrm{OHF}_u$ mixtures.

Figure 3.13: I_p-I_s and I_p+I_s as a function of temperature for a film of the 50% 9OHF/50% 11OHF mixture from DOR while cooling at $0.1°C/min$. Arrows mark the transition temperatures. The thickness of the film is below 30 layers.

3.3 Other Mixtures

3.3.1 Mixtures of 9OHF and 11OHF

A natural question one would ask is whether the 50% 9OHF/50% 11OHF mixture has the same physical property as 10OHF. If the 50% 9OHF/50% 11OHF mixture can reproduce the reversed phase sequence of 10OHF, it probably means 10OHF is not unique. The DOR data of the 50% 9OHF/50% 11OHF mixture are shown in Fig. 3.13. The SmA-SmC$_\alpha^*$ transition temperature T_1 can be determined by the sudden increase in I_p+I_s. Unfortunately, this film does not have oscillations in the SmC$_\alpha^*$ phase because the film is very thin (below 30 layers). The oscillations do show up in the other thick

films of the same mixture so that we know it is the SmC^*_α phase. This plot is chosen because it shows a clear-cut transition into the SmC^* phase. It is very clear that there is no SmC^*_{d4} phase between the SmC^*_α and the SmC^* phase. Neither the SmC^*_{d4} phase nor the reversed phase sequence exists in this mixture. This proves that mixing 9OHF with 11OhF does not reproduce the reversed phase sequence of 10OHF. The reversed phase sequence is indeed a unique property of 10OHF.

3.3.2   Mixtures of C9 and nOHF homologs

It is known that C9 stabilizes the SmC^*_{d4} phase in 10OHF. It would be interesting to see if C9 will induce the SmC^*_{d4} phase in other nOHF homologs. If the answer is yes, one would also wonder whether the SmC^*_{d4} phase appears below the SmC^* phase (like in the normal case) or above the SmC^* phase (like in 10OHF). In order to answer these questions, we made three mixtures of C9 and nOHFs, namely the 50% C9/50% 9OHF, 50% C9/50% 11OHF and 30% C9/70% 12OHF mixtures.

The phase sequence of the 50% C9/50% 9OHF mixture is SmA-SmC^*_α-SmC^*, the same as the 9OHF. No SmC^*_{d4} phase is found.

The 50% C9/50% 11OHF mixture appears more interesting. From the DOR data (Fig. 3.14) we can clearly identify the SmC^*_α by oscillations and SmC^* phase by the split of the signal from two α values. However, we are not sure about the low temperature phase. It has $180°$ symmetry as shown by the overlapping of the $\alpha = 180°$ and $\alpha = 0°$ data, from which we can only say that it could be either the SmC^*_{d4} phase or the SmC^*_A phase. Neither DOR nor NTE has the ability to discriminate these two phases, both of which exist in C9. Therefore, we have to run RXRD on this sample.

The RXRD data (Fig 3.15) unambiguously shows that the low temperature phase is SmC^*_{d4}. It also confirms the SmC^*_α and SmC^* phases in this mixture. The pitch decreases from 6.9 layers to 6.2 layers upon cooling in the SmC^*_α phase. Compared to the SmC^*_α pitch in C9, which is from 6.2 layers to 4.6 layers upon cooling, the pitch in this mixture is longer. It suggests that probably 9OHF has a longer pitch in the SmC^*_α phase than C9. The pitch in the SmC^* phase of this mixture is around 110 layers.

The 50% C9/50% 11OHF mixture has the phase sequence of SmA($102.9°C$) SmC^*_α($94.0°C$) SmC^*($87.8°C$) SmC^*_{d4}($50.0°C$) Crystal. To answer the first question at the beginning of this section, the SmC^*_{d4} phase does show up in the C9/11OHF mixture. Surprisingly,

it has a temperature range of 38 degrees, much larger than the SmC^*_{d4} phase in C9 (24 degrees). It is hard to explain why 11OHF, without any SmC^*_{d4} phase, could expand the SmC^*_{d4} phase by such a large amount when mixing with C9. The SmC^*_{d4} is below the SmC^* phase. Thus, 10OHF and its mixtures remain the ones in which the phase reversal is observed.

The phases in the 30% C9/70% 12OHF mixture becomes more complicated (Fig 3.16). Above T_1 is the SmA phase. Between T_1 and T_2 is the SmC^*_α phase. The oscillations are not very clear because this film is thick (more than 500 layers) and the periods of the oscillations are very small. Between T_2 and T_3 is the SmC^*_{d4} phase. The data in the SmC^*_{d4} phase is noisy because of the defects as shown in Fig 1.4. The temperature range is smaller than that of C9. Surprisingly, the SmC^*_{d3} phase appears below the SmC^*_{d4} phase, indicated by the extremely noisy and non-repeatable signal (texture of the film shown in Fig 1.4). Since neither C9 nor 12OHF has the SmC^*_{d3} phase, it is not expected in their mixture. However, a similar phenomenon has been observed by Lagerwall *et. al* [35]. They claim that the SmC^*_{d3} phase sometimes arises as a result of the frustration in the mixtures of one compound favoring the ferroelectric phase and the other favoring antiferroelectric phase. Below T_4, it is the antiferroelectric SmC^*_A phase.

Many mixtures of the homologs members nOHF (n = 9, 10, 11, 12) have been studied. The results along with those obtained from mixtures of nOHF and C9 are summarized in Table 3.1.
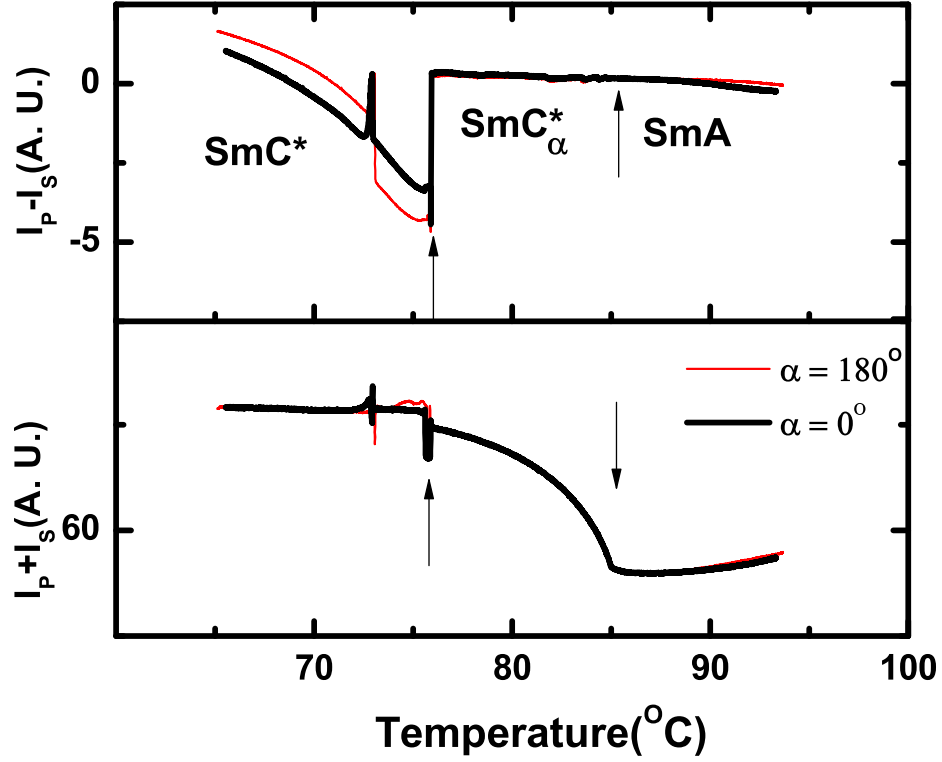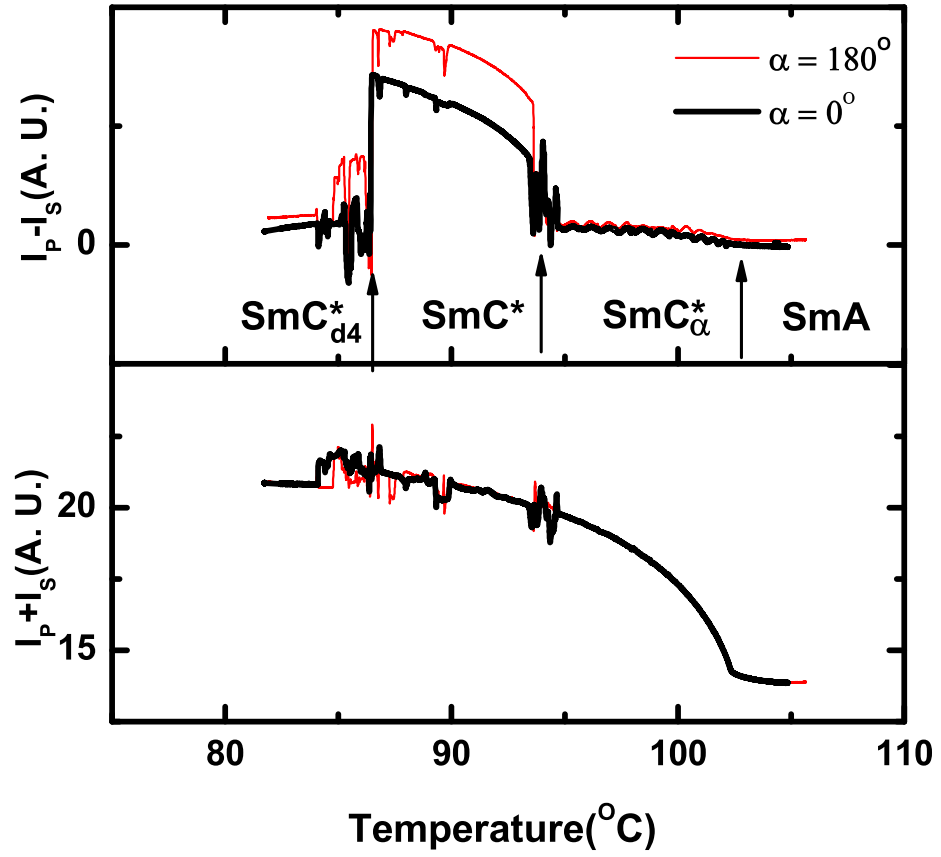
Figure 3.14: I_p-I_s and I_p+I_s as a function of temperature for a film of the 50% C9/50% 11OHF mixture from DOR while cooling at 0.1°C/min. Arrows mark the transition temperatures. The thickness of the film is more than 400 layers.
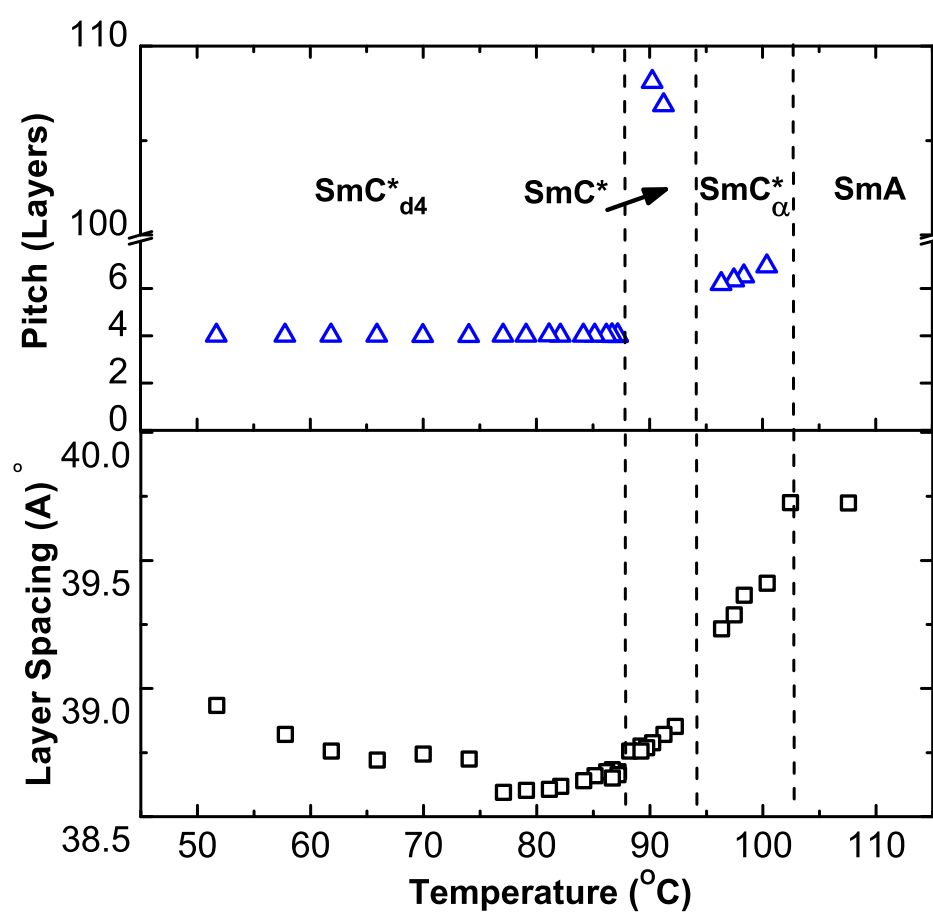
Figure 3.15: Temperature dependences of pitch (triangles) and layer spacing (squares) for the 50% C9/50% 11OHF mixture. Different phases are divided by dashed lines.
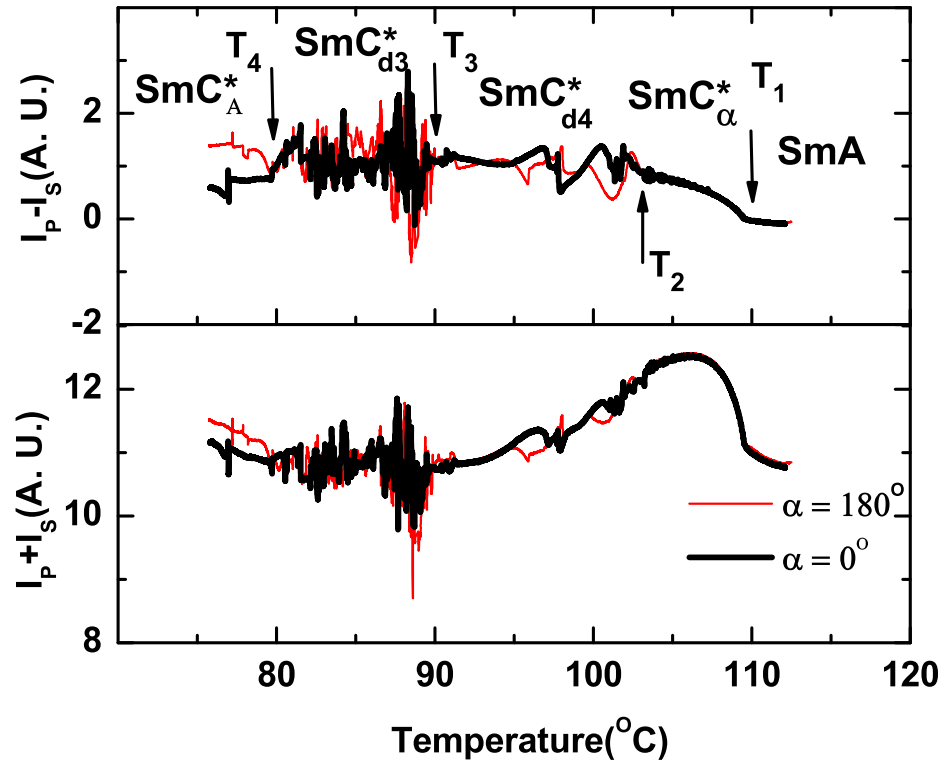
Figure 3.16: I_p-I_s and I_p+I_s as a function of temperature for a film of the 30% C9/70% 12OHF mixture from DOR while cooling at 0.1°C/min. Arrows mark the transition temperatures. The thickness of the film is more than 400 layers.

	10OHF	9OHF	11OHF	12OHF	C9
10OHF	SmC^*_α-SmC^*_{d4}-SmC^*	SmC^*_α-SmC^*_{d4}-$SmC^{*\dagger}$	SmC^*_α-SmC^*_{d4}-$SmC^{*\S}$	SmC^*_α-SmC^*_{d4}-$SmC^{*\ddagger}$	SmC^*_α-SmC^*_{d4}-$SmC^{*\P}_*$
9OHF	SmC^*_α-SmC^*_{d4}-$SmC^{*\dagger}$	SmC^*_α-SmC^*	SmC^*_α-SmC^* (50%9OHF/50%11OHF)	N/A	SmC^*_α-SmC^* (50%9OHF/50%C9)
11OHF	SmC^*_α-SmC^*_{d4}-$SmC^{*\S}$	SmC^*_α-SmC^* (50% 9OHF/50% 11OHF)	SmC^*_α-SmC^*	N/A	SmC^*_α-SmC^*-SmC^*_{d4} (50%11OHF/50%C9)
12OHF	SmC^*_α-SmC^*_{d4}-$SmC^{*\ddagger}$	N/A	N/A	SmC^*_α-SmC^*	SmC^*_α-SmC^*_{d4}-SmC^*_{d3}-SmC^*_A (30%12OHF/70%C9)
C9	SmC^*_α-SmC^*_{d4}-$SmC^{*\P}$	SmC^*_α-SmC^* (50% 9OHF/ 50% C9)	SmC^*_α-SmC^*-SmC^*_{d4} (50%11OHF/50%C9)	SmC^*_α-SmC^*_{d4}-SmC^*_A (30%12OHF/70%C9)	SmC^*_α-SmC^*_{d4}-SmC^*_A

† The SmC^*_{d4} phase disappears beyond 50% 9OHF concentration.
§ The SmC^*_{d4} phase disappears beyond 27% 11OHF concentration.
‡ The SmC^*_{d4} phase disappears beyond 25% 12OHF concentration.
¶ The SmC^* phase disappears beyond 50% C9 concentration.

Table 3.1: Phase sequences of mixtures of nOHF and Cn

3.4   Ternary mixture

From the previous section we learned that adding C9 into a compound without the SmC_{d4}^* phase could induce the SmC_{d4}^* phase. This induced SmC_{d4}^* phase appears below the SmC^* phase as in the normal phase sequence. The absence of the SmC_{d4}^* phase in the 73% 10OHF/27% 11OHF mixture makes it a very good candidate for further study on the reversed phase sequence. We want to know whether C9 will bring the SmC_{d4}^* phase back and whether the SmC_{d4}^* phase shows above or below the SmC^* phase.

A series of (73% 10OHF/27% 11OHF)$_{1-x}$ C9$_x$ mixtures with x = 0.05, 0.10, 0.15 and 0.25 were prepared and investigated by using NTE and DOR. Figure 3.17 shows the phase diagram of (73% 10OHF/27% 11OHF)$_{1-x}$ C9$_x$ mixtures obtained from DOR measurements. The phase sequence at x = 0.15 was confirmed by RXRD studies. For example, at T = 83.6°C, the resonant peak is at Q_z/Q_0 = 1.17 ($Q_0=2\pi/d$ and d is the layer spacing), indicating the SmC_α^* phase with a pitch value of 5.8 layers. At T = 73°C, the resonant peak position near Q_z/Q_0 = 1.25 reveals a four layer structure. This proves that it is the SmC_{d4}^* phase. At T = 52.6°C, a resonant peak on the shoulder of the (002) Bragg peak is observed. It is the SmC^* phase with a pitch of 150 layers.

The effect of C9 doping on pure 10OHF is that it stabilizes the SmC_{d4}^* phase existing in 10OHF. In the 73% 10OHF/27% 11OHF binary mixture, there is no SmC_{d4}^* phase. By adding only 5% C9 into this binary mixture, the SmC_{d4}^* phase is restored with a temperature window of 21 degrees, which is just slightly smaller than 24 degrees found in pure C9. In addition, the SmC_{d4}^* phase range expands to more than 30 degrees with increasing C9 concentration in the ternary mixtures. The SmC_{d4}^* phase becomes thermotropic. Meanwhile, the temperature window of the SmC^* phase is reduced dramatically with increasing C9 concentration.

It is interesting to compare the SmC_{d4}^* phase temperature window of (73% 10OHF/27% 11OHF)$_{1-x}$ C9$_x$ mixtures with that of the 10OHF/C9 mixtures. Since pure 11OHF has no SmC_{d4}^* phase and it destabilizes the SmC_{d4}^* phase when mixing with 10OHF, one might expect that 11OHF would also decrease the temperature window of the SmC_{d4}^* phase when added into the 10OHF/C9 mixture. Figure 3.18 shows the temperature range of the SmC_{d4}^* phases in the 10OHF/C9 mixtures from Ref. [29] and the ternary mixtures studied in this research work. The data point at 15% C9 for the binary mixture

has a larger error bar because we didn't study this particular mixture. The data was constructed by interpolation from the 10OHF/C9 phase diagram. Surprisingly, 11OHF broadens the SmC_{d4}^* phase in all the ternary mixtures, by up to 15 degrees. It is consistent with the fact that the 50% C9/50% 11OHF mixture has a much larger SmC_{d4}^* temperature.

To gain a better knowledge about this phase reversal phenomenon, we also studied the pitch evolution of the (73% 10OHF/27% 11OHF)$_{0.85}$ C9$_{0.15}$ mixture in the SmC_α^* phase by RXRD (Fig. 3.19(a)). Upon cooling, the pitch is found to be 6.7 layers just below the SmA-SmC_α^* transition. Then the pitch decreases to 5.6 layers and subsequently increases to 5.9 layers. Unlike in most of the compounds and mixtures we have investigated, the pitch in this ternary mixture evolves nonmonotonically with temperature in the SmC_α^* phase.

To date, three theoretical models predict the existence of the mesophases with six-layer periodicity [36, 37, 38, 39]. From Fig. 3.19(a), we can see the pitch value yields 5.95 layers (our resolution was about ±0.05 layer) at two temperatures with one degree separation before the transition to the SmC_{d4}^* phase. However, the shape of the resonant satellite peaks at these two temperatures did not show any difference from the rest of data taken in the SmC_α^* phase (Fig. 3.19 (b)-(d)) within the experimental resolution. Our simulation shows that for a distorted six-layer phase, the resonant peaks are split peaks with different intensities. Meanwhile, from the NTE measurements, all the studied films are, within our experimental resolution, optically uniaxial above the SmC_α^* to SmC_{d4}^* transition temperature. Based on the experimental results, the existence of the distorted six-layer phase is unlikely because neither biaxiality nor split peaks are observed. On the other hand, our data cannot rule out the possibility of a small temperature range of a uniaxial phase with 6-fold clock arrangement. More experimental results are required to address an important question. What is the difference between a uniaxial phase with a six-layer clock arrangement and an extremum near 6 layers in the temperature variation of helical pitch in the SmC_α^* temperature window?
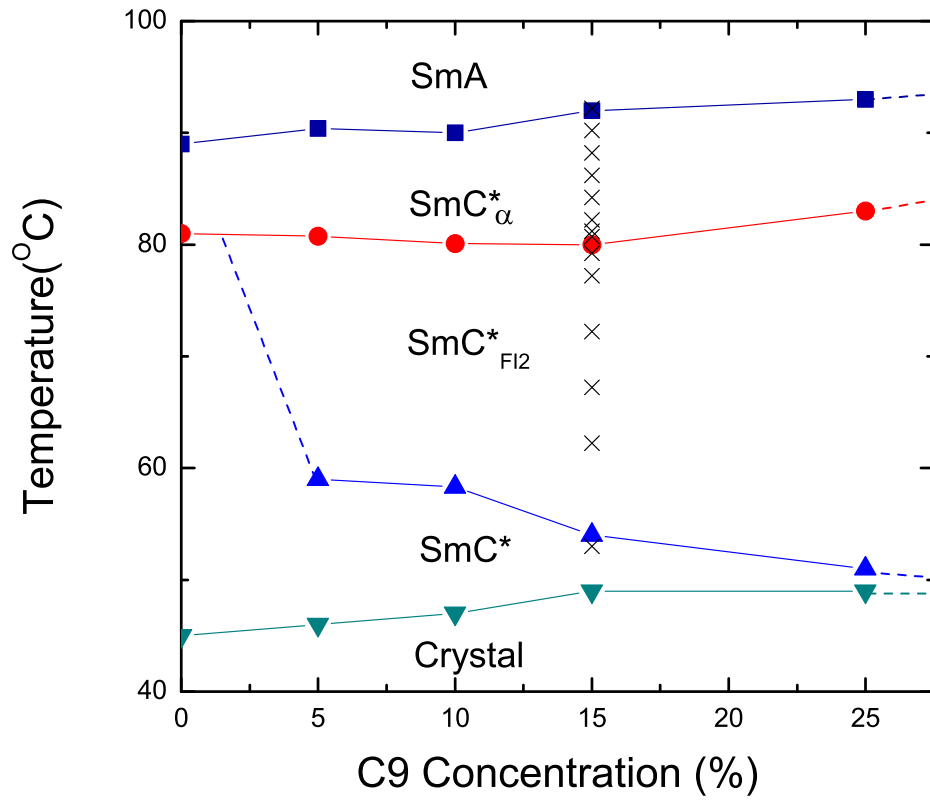
Figure 3.17: Phase diagram of $(73\% \; 10\text{OHF}/27\% \; 11\text{OHF})_{1-x} \; \text{C9}_x$ mixtures. The crosses mark the temperatures at which RXRD was performed. The phase sequence of C9 is SmA ($115°$C) SmC$_\alpha^*$ ($109°$C) SmC$_{d4}^*$ ($85°$C) SmC$_A^*$. The disappearance of the SmC$_\alpha^*$-SmC$_{d4}^*$ transition below 10% C9 mixture is not an important issue for reseach work. Without any data in this range, we represent this part of phase boundary by a dashed line.
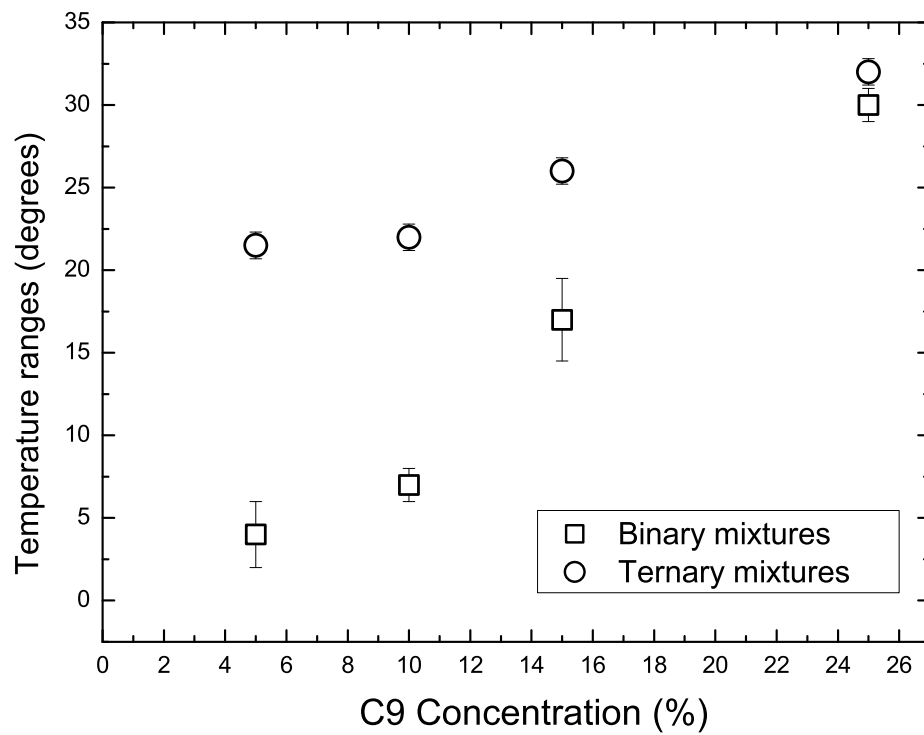
Figure 3.18: Temperature ranges of the SmC$^*_{d4}$ phase in the ternary (73% 10OHF/27% 11OHF)$_{1-x}$ C9$_x$ mixtures and in the binary (10OHF)$_{1-x}$ C9$_x$ mixtures as a function of C9 concentration (x).
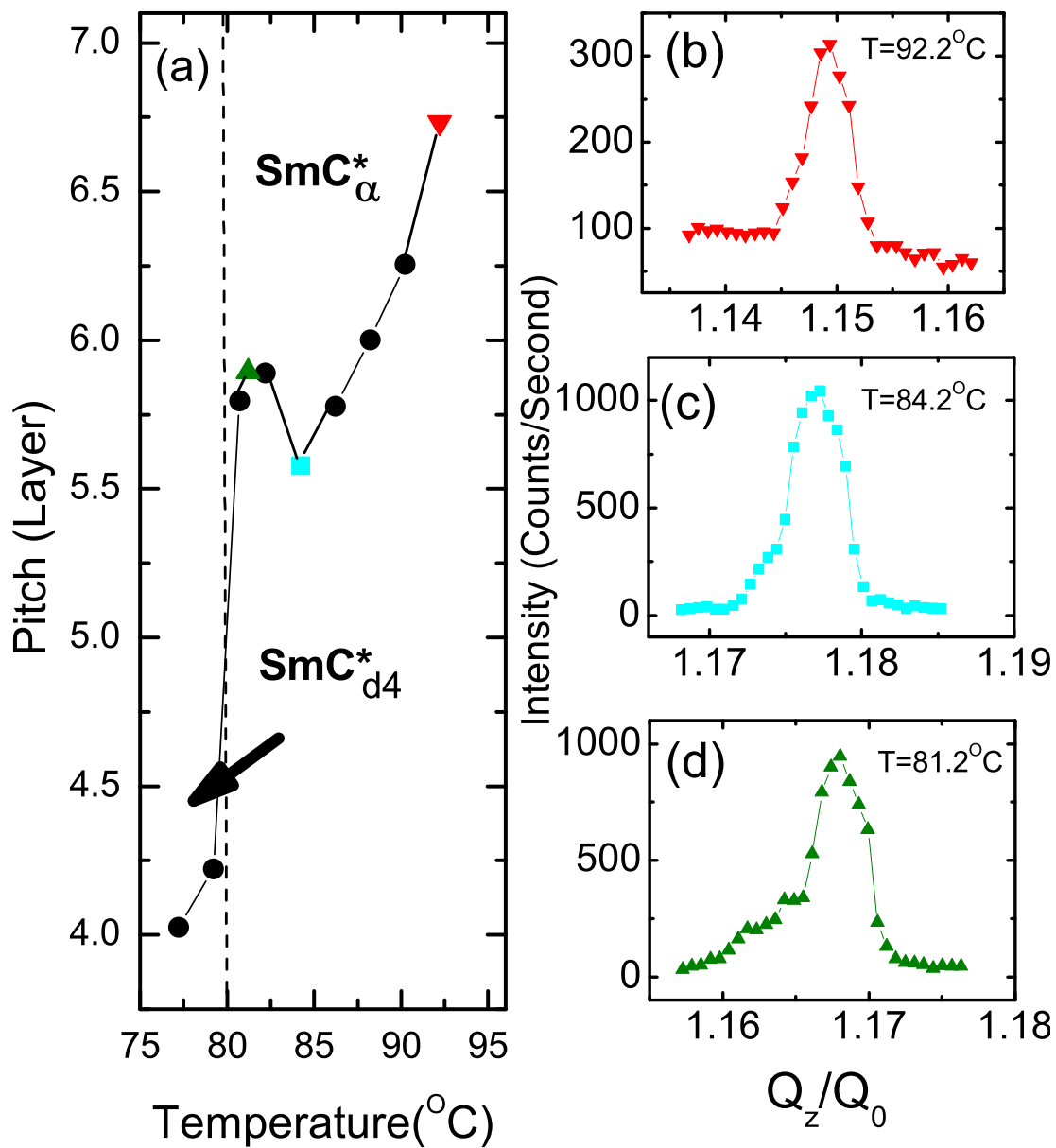
Figure 3.19: (a) The pitch-temperature evolution of the (73% 10OHF/27% 11OHF)$_{0.85}$ C9$_{0.15}$ ternary mixture in the SmC$_\alpha^*$ phase measured by RXRD. (b)-(d) Scans of the same mixture at 92.2°C, 84.2°C and 81.2°C.

3.5 Summary

To summarize, we have studied binary mixtures of 10OHF and its homologs and found that none of the three homologs stabilizes the unusual phase sequence of 10OHF. In most cases, the temperature window of the SmC_{d4}^* phase continuously decreases with increasing concentration of the doping homologs. No reversed phase sequence was found in the other nOHF/C9 mixtures either. In the 10OHF/11OHF/C9 ternary mixtures, the SmC_{α}^*-SmC_{d4}^*-SmC^* phase sequence is restored. Our studies show that the SmC_{d4}^* phase becomes stable in the 10OHF/C9 mixtures but not in both 10OHF/11OHF and 11OHF/C9 binary mixtures. Thus it is surprising to find out that the presence of 11OHF in the ternary mixtures significantly stabilize the SmC_{d4}^* phase. A possible new phase with six-layer periodicity is also observed.

Finally, it is worthwhile to point out that previous studies on the antiferroelectric display are mainly focused on the SmC_A^* phase, which requires a high switching voltage. The SmC_{d4}^* phase, which is also antiferroelectric, requires much lower E fields to change to the ferroelectric state [4]. Some mixtures studied in this research work with very wide temperature ranges for the SmC_{d4}^* phase should be good candidates for research in antiferroelectric displays.

Chapter 4

The Discovery Of A Novel Liquid Crystal Phase

We report the discovery of a new smectic-C^* liquid crystal phase with six-layer periodicity by DOR, NTE and RXRD [40]. Upon cooling, the new phase appears between the SmC_α^* phase having a helical structure and the SmC_{d4}^* phase with four-layer periodicity. This SmC_{d6}^* phase is identified in two mixtures which have an unusual reversed SmC_{d4}^*-SmC^* phase sequence. We observe discontinuity in the optical data of the two mixtures. From RXRD, there are three experimental observations supporting our discovery. First, the pitch shows a clear jump at the SmC_α^*-SmC_{d6}^* phase transition and stays locked-in to six layers in the SmC_{d6}^* phase. Discontinuity in the layer spacing is also observed in one of the mixtures at the transition. Second, the split resonant x-ray peaks in the SmC_{d6}^* phase reveal a distorted biaxial structure, which distinguishes it from the uniaxial SmC_α^* phase characterized by a single resonant peak. The third experimental observation is the coexistence of the SmC_{d6}^* and SmC_α^* phases near the SmC_α^*-SmC_{d6}^* transition temperature, indicating a first order phase transition. The SmC_{d6}^* phase shows a distorted clock structure. Three theoretical models have predicted the existence of a six-layer phase. However, our experimental findings are not consistent with the theories.
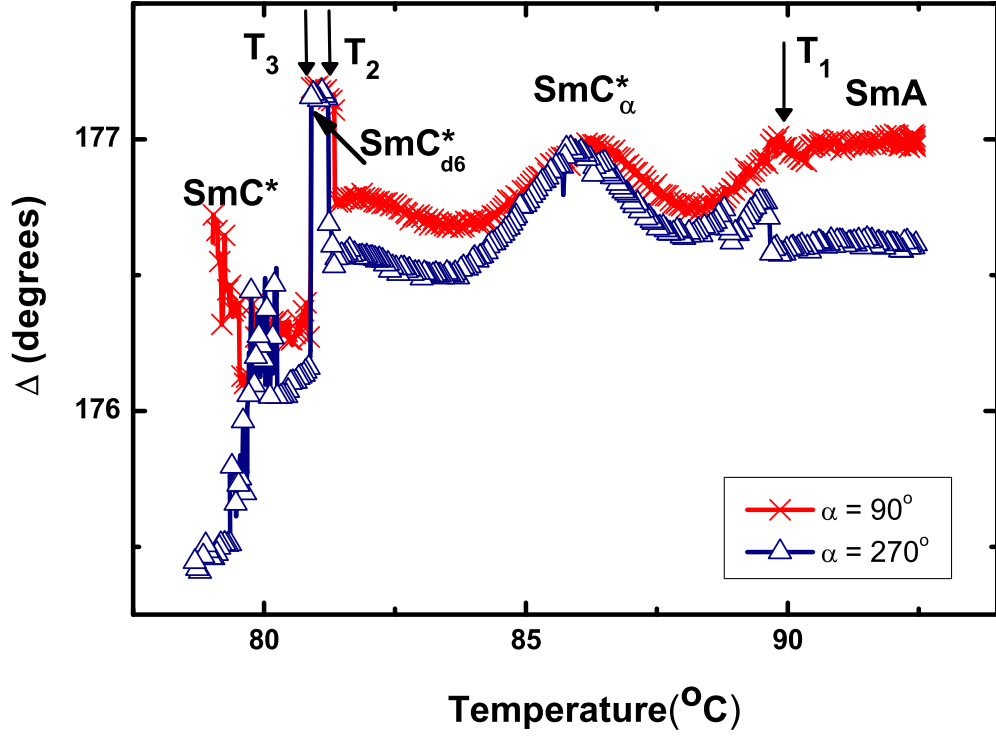
Figure 4.1: Δ as a function of temperature for a film of Mixture A from NTE while cooling at $0.1°C/min$. Arrows mark the transition temperatures. The thickness of the film is about 80 layers.

4.1 The (73% 10OHF/27% 11OHF)$_{0.85}$ C9$_{0.15}$ mixture

4.1.1 NTE studies

The (73% 10OHF/27% 11OHF)$_{0.85}$ C9$_{0.15}$ ternary mixture showing a strange pitch evolution in the SmC$_\alpha^*$ phase (Fig. 3.19) is certainly intriguing. In this section, we try to answer all the questions left at the end of the Chapter 3 by performing more detailed investigation on this mixture. It turns out that the two data points with the pitch value of six layers are indeed in a completely new phase. We name this newly discovered phase the SmC$_{d6}^*$ phase.

First, let us take a look at the NTE data of the (73% 10OHF/27% 11OHF)$_{0.85}$ C9$_{0.15}$ ternary mixture, which we will call Mixture A from now on. The ramp data is displayed

in Fig. 4.1. Between T_1 and T_2 is the SmC^*_α phase. Near T_2, Δ shows jumps at both $\alpha=90°$ and $\alpha=270°$. There are discontinuities in the vicinity of T_3. It is pretty clear from the data that between T_2 and T_3 there is another phase within a small temperature range. Another way to use NTE is to hold the temperature at certain value and record Δ while rotating the electric field orientation α. We call this "rotation". From the rotation data, we could extract the information such as the symmetry and biaxiality. The rotation data of Mixture A at different temperatures are summarized in Fig. 4.2. We can see that between T_1 and T_2, the biaxiality of the film (proportional to the span of Δ) is small. This is consistent with the uniaxial structure of the SmC^*_α phase. The small biaxiality comes from the surface layers. Between T_2 and T_3, the data becomes almost symmetrical about $\alpha = 180°$ axis. It means that this phase has $180°$ symmetry. Another distinction from the SmC^*_α phase is that the biaxiality becomes larger, but still small compared to that in the SmC^*_{d4} phase. Below T_3, the data is still almost symmetrical about the $\alpha = 180°$ axis. However, the profile of the data changes from "M" to "W" shape. As the temperature lowers, the difference between the two minima becomes more pronounced and the symmetry axis shifts away from $\alpha = 180°$. These indicate some changes in the structure.
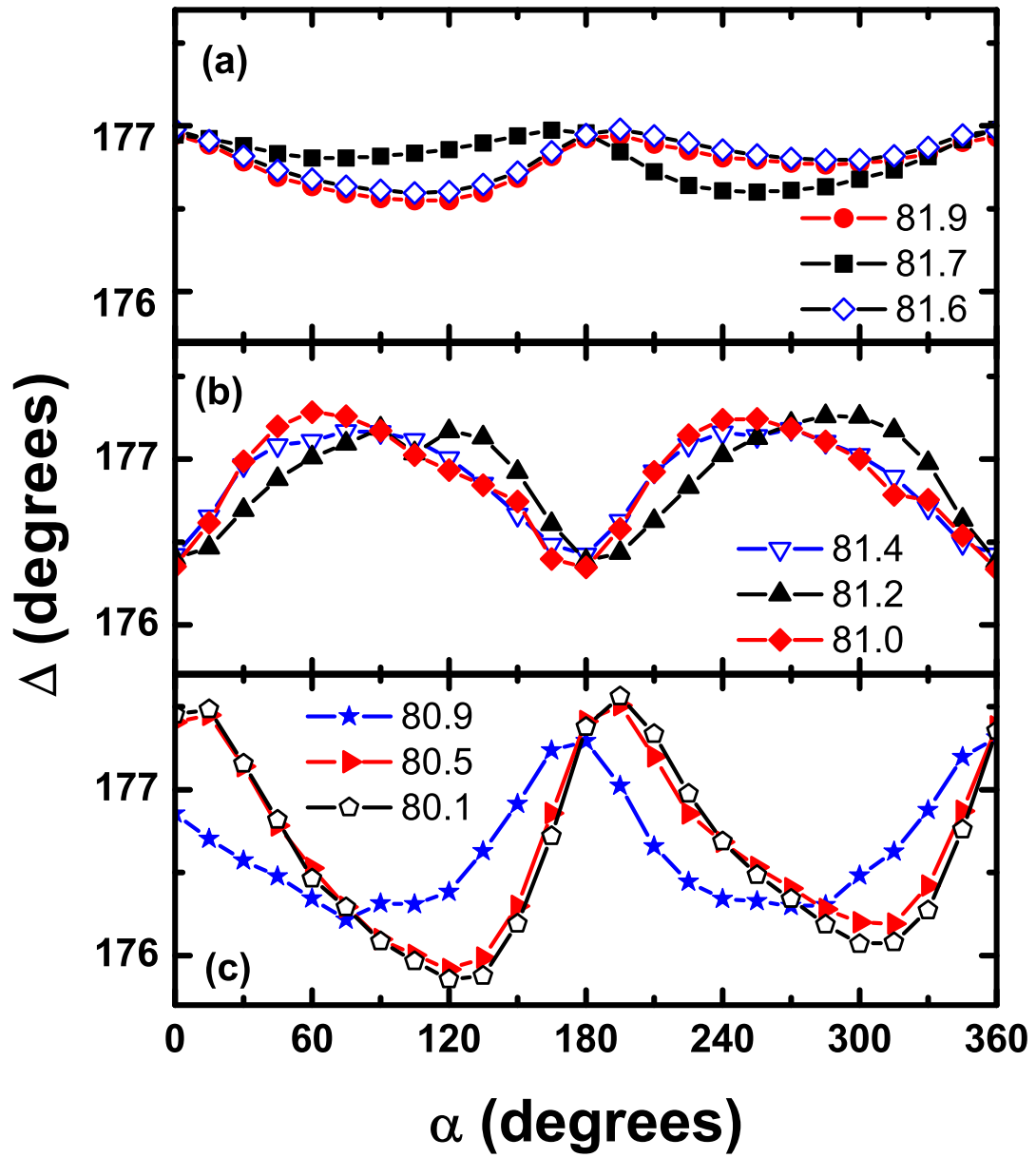
Figure 4.2: Δ vs. α for Mixture A (a) between T_1 and T_2 (b) between T_2 and T_3 (c)below T_3.
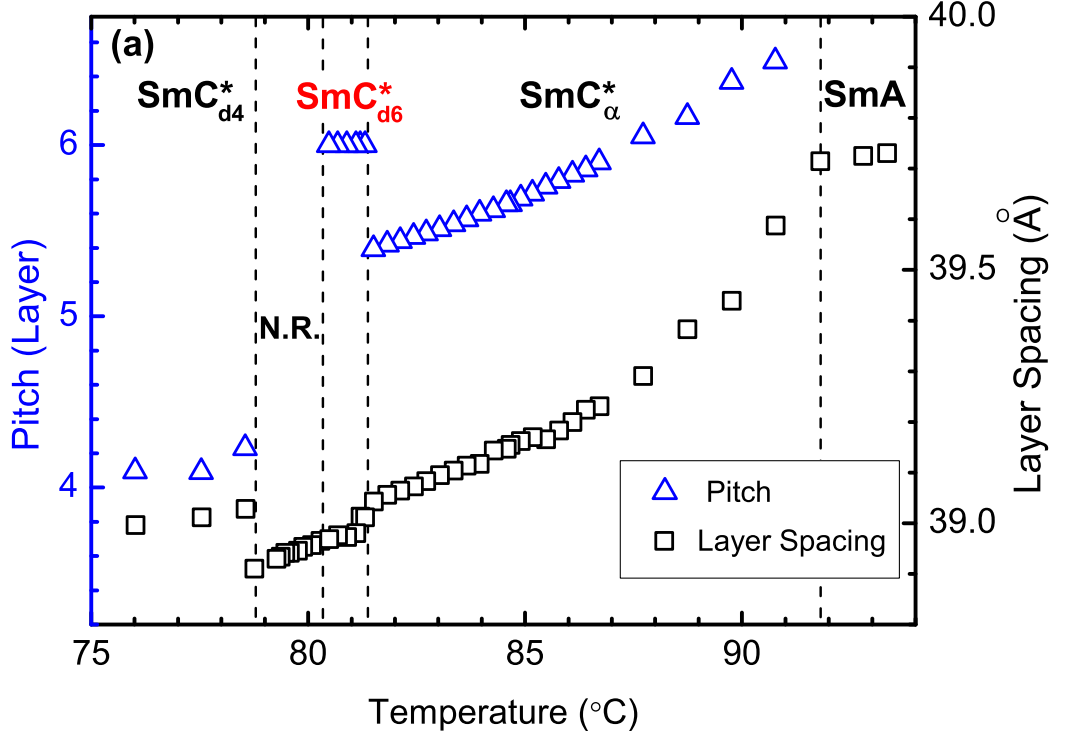
Figure 4.3: Temperature dependences of pitch (triangles) and layer spacing (squares) for Mixture A. Different phases are divided by dashed lines. Noisy resonant signals are obtained in the regions between the SmC_{d6}^* and SmC_{d4}^* phases. We call it the noisy region (N.R.). No pitch data are given in this region.

4.1.2 RXRD data

With the convincing optical data in hand, we are more positive about the existence of the SmC_{d6}^* phase. Therefore, we conducted the high-resolution RXRD experiment again. Compared to the preliminary measurements presented in Chapter 3, the full width half maximum was reduced approximately by a factor of 3 by decreasing the size of both the input and output slits. In order to compensate the loss of the photon counts, much thicker films (more than 1000 layers) were prepared, providing larger scattering intensities. The uncertainty in the pitch measurement was reduced from ± 0.05 L to ± 0.03 L. High resolution in Q is also important for the observation of the split peaks in the SmC_{d6}^* phase.

The temperature dependences of pitch and layer spacing for Mixture A are shown

in Fig. 4.3, the pitch in the SmC_α^* phase decreases almost linearly from 6.49 to 5.39 layers upon cooling. At T $= 81.43\,^\circ C$, there is an abrupt jump to 6.00 layers. A sudden decrease in the layer spacing is also observed at this temperature. Then the pitch stays locked-in to 6.00 layers for a temperature range of approximately one degree. The lock-in of the pitch to six layers is a clear evidence of the existence of the SmC_{d6}^* phase. The jump implies that the SmC_{d6}^* phase and the SmC_α^* phase are two different phases and the transition between them is first order. From the layer spacing data we can also see that the tilt angle nearly saturates around the SmC_{d6}^* phase. It is interesting how the pitch evolves with temperature. Upon cooling, it decreases smoothly through six layers and then jumps up to six. There are two structures with six-layer periodicity in this mixture, (i) a uniaxial SmC_α^* structure with a pitch value of six existing near $T = 87.72$ $^\circ C$ and (ii) a biaxial SmC_{d6}^* structure over a temperature range of about one degree. These two structures show very different resonant peaks. Examples of resonant peaks in the SmC_α^* phase, the SmC_{d6}^* phase and the SmC_{d4}^* phase are summarized in Fig. 4.4 and 4.5.

Between T $= 80.2\,^\circ C$ and T $= 78.9\,^\circ C$, the pitch is not well defined because there are multiple weak and noisy peaks spread over a wide range in Q space (a hundred times broader than the full width half maximum of the SmC_α^* and SmC_{d6}^* resonant peaks, see Fig. 4.6). At the same time, the shapes of the non-resonant principal peaks do not change at all. The resonant peaks become sharp again in the SmC_{d4}^* phase, accompanied by a discontinuity in the layer spacing. This behavior suggests that during the transition from the SmC_{d6}^* to SmC_{d4}^* phase, the layer structure remains well established but the orientations of the molecules are in a very complex state due to the frustration. How to extract the information about the orientational order from these noisy peaks in this region remains an important research project for us in the future.
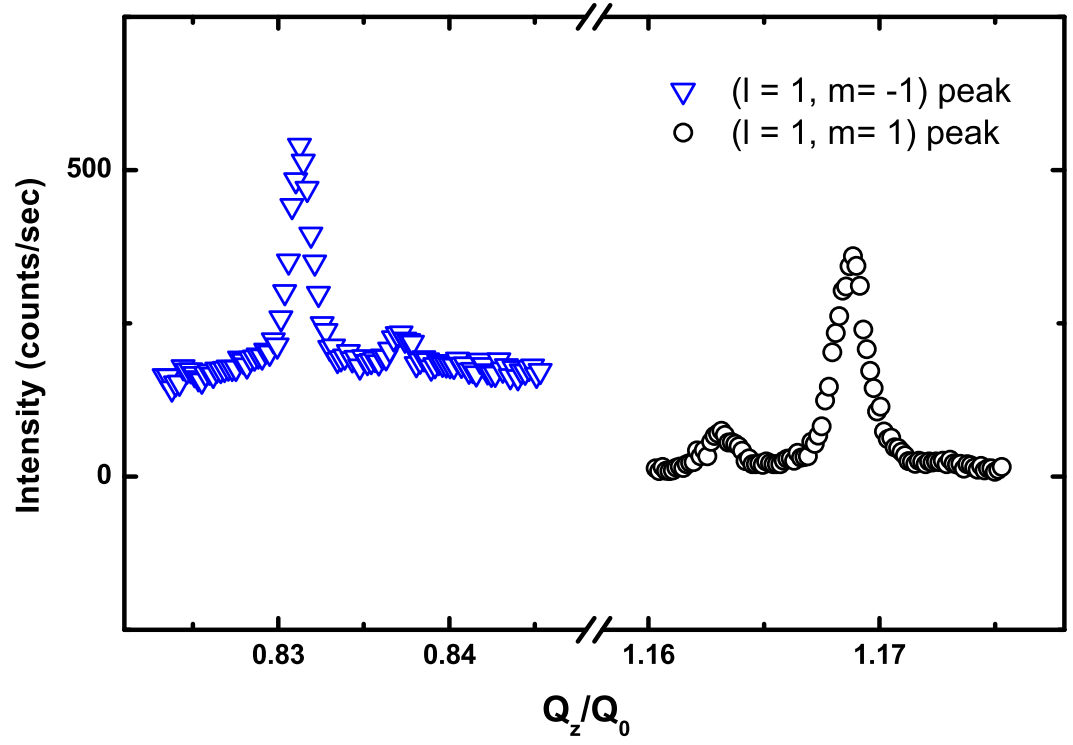
Figure 4.4: The $(l = 1,\ m = -1)$ and $(l = 1,\ m = 1)$ SmC^*_{d6} resonant satellite peaks from Mixture A at $T = 80.89\,^\circ C$.
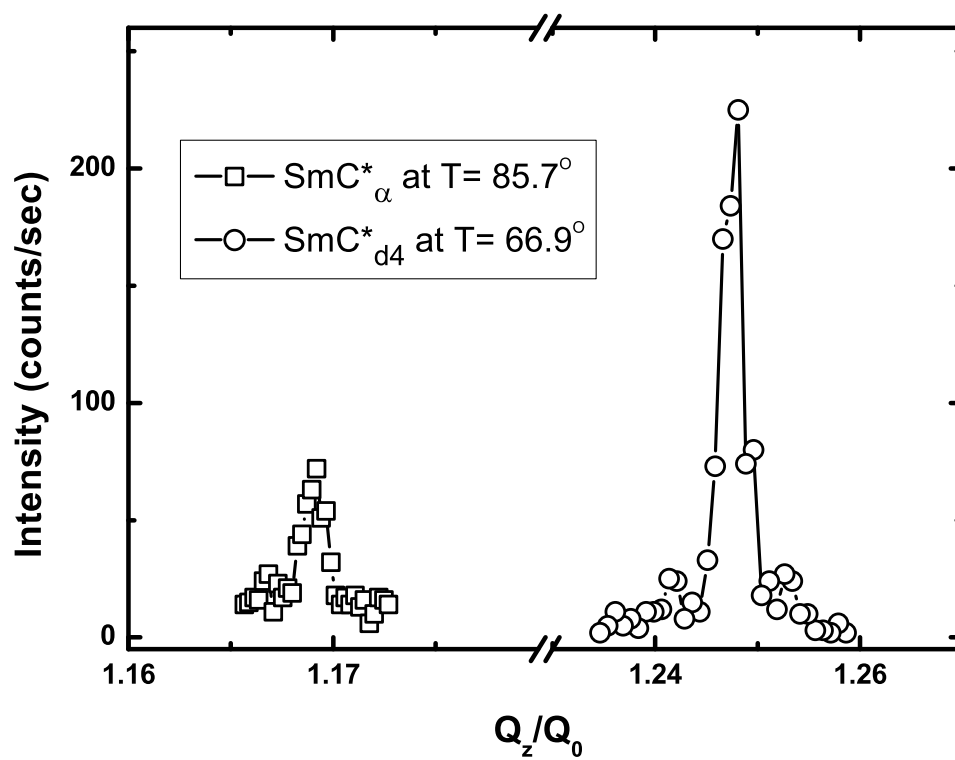
Figure 4.5: The SmC^*_α and SmC^*_{d4} resonant satellite peaks from Mixture A.
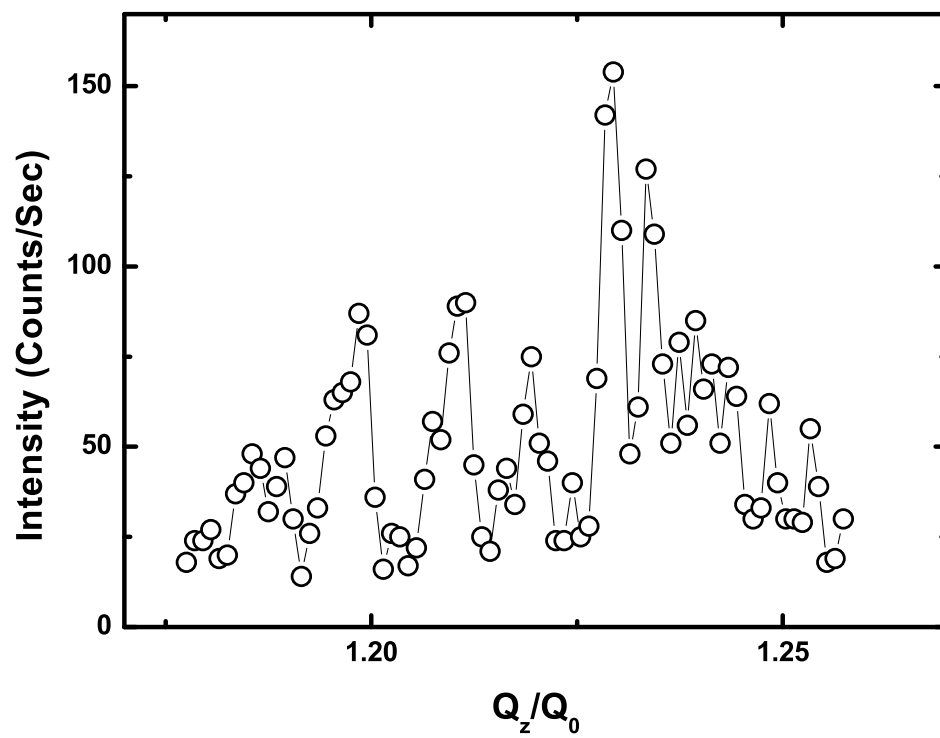
Figure 4.6: The resonant signal in the noisy region from Mixture A.

4.1.3 The SmC^*_{d6} resonant peaks

A typical x-ray intensity scan vs. Q_z in the SmC^*_{d6} phase in Mixture A at $T = 80.89$ $^\circ C$ is displayed in Fig. 4.7. The data clearly show split peaks centered at $Q_z/Q_0 = 1.167$ ($l = 1$, $n = 6$, $m = 1$). It indicates that the SmC^*_{d6} phase is a biaxial six-layer phase. The fact that resonant satellite peaks disappear at $E = 2.460$ keV demonstrates the resonant nature of the split peaks. The cartoon in Fig. 4.7 depicts the structure we propose for the SmC^*_{d6} phase. It is a natural extension of the structure of the SmC^*_{d4} phase. We carried out numerical simulations based on Levelut and Pansu's work [27]. Our results show that if $\delta = 0^\circ$ (planar structure), the two peaks are of equal intensity. If $\delta = 60^\circ$ (uniaxial structure), there is only one single peak. Two peaks of different intensities suggest that the SmC^*_{d6} phase has a distorted clock structure (see Fig. 4.8 and 4.9). The simulation that fits our data yields $\delta = 27^\circ \pm 2^\circ$. Split peaks centered at $Q_z/Q_0 = 0.833$ ($l = 1$, $n = 6$, $m = -1$) were also observed (Fig. 4.4).
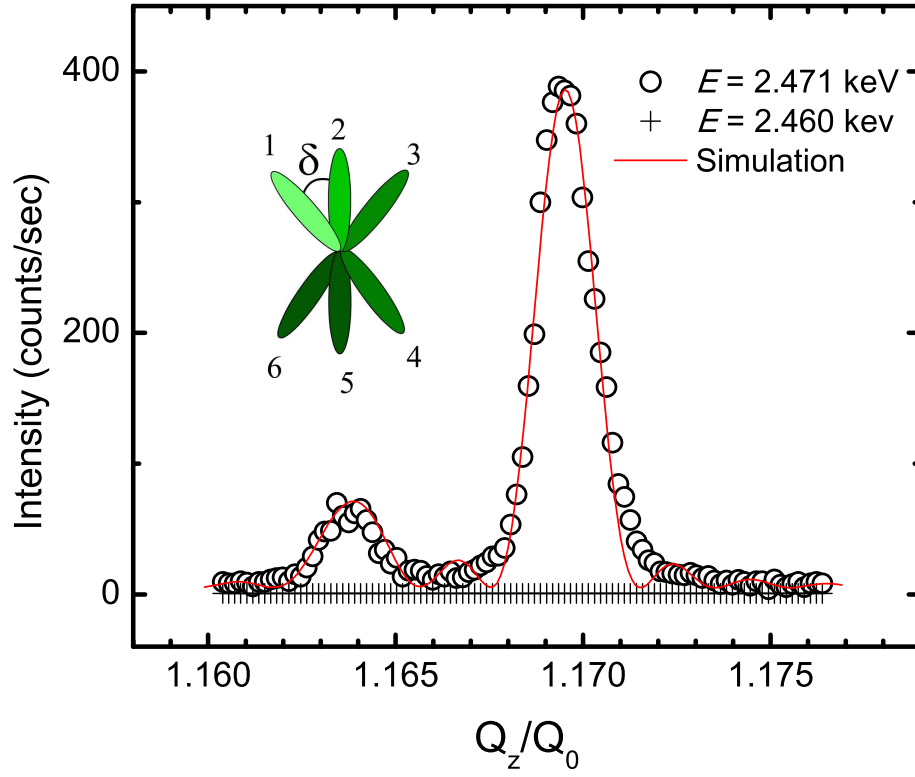
Figure 4.7: The resonant satellite peak (circles) from Mixture A at $80.89\ ^\circ C$ and the simulation (line). Crosses are off-resonance data obtained at $E = 2.460$ keV. The center of the split peaks is located at $Q_z/Q_0 = 1.167$, corresponding to a pitch of six layers. The split peaks indicate a distorted structure. The positions and intensities of the two peaks give an optical pitch of 350 layers (1.36 μm) and a distortion angle δ of $27\pm2^\circ$. The simulation has been normalized to match the measured intensities. The cartoon is the structure used in our fitting.
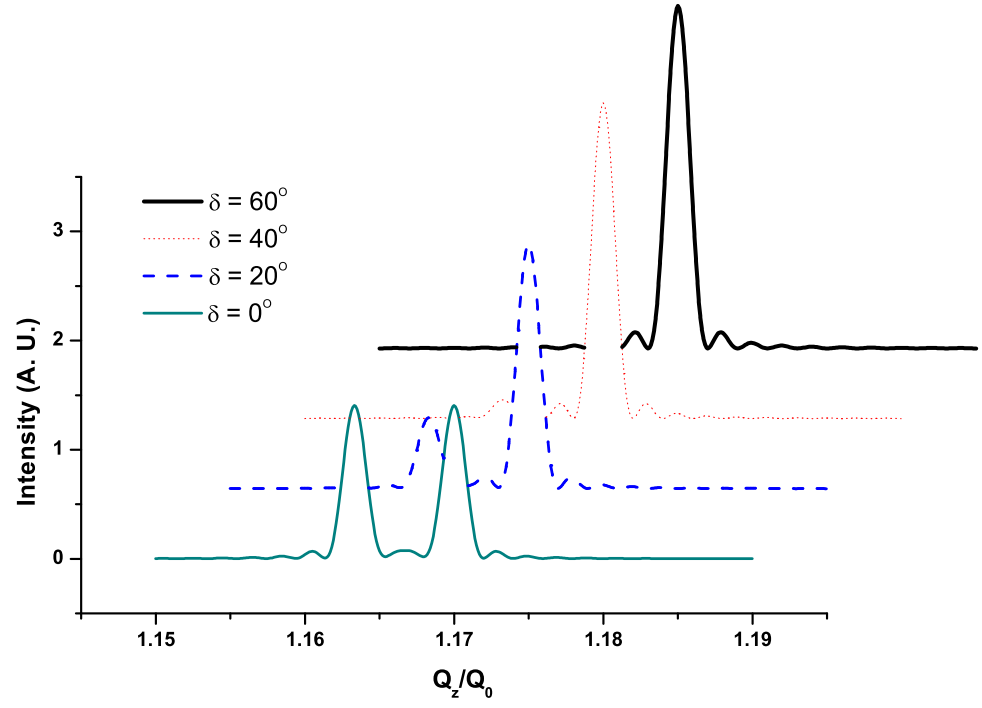
Figure 4.8: The simulated peaks at $Q_z/Q_0 = 1.167$ for different distortion angle δ.
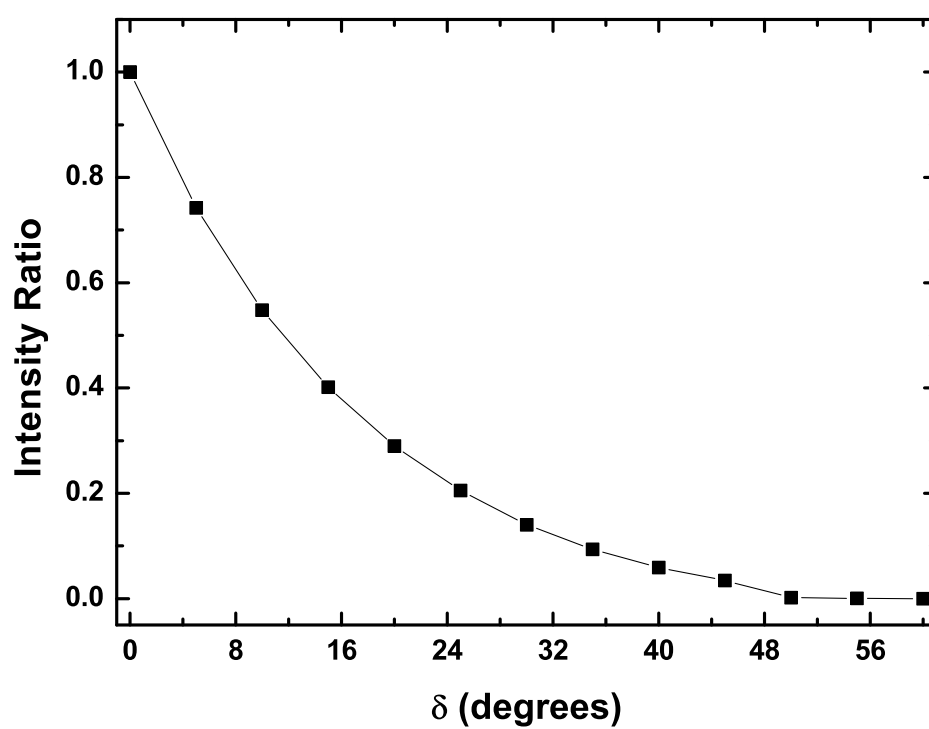
Figure 4.9: The relationship between the intensity ratio of the split peaks and the distortion angle δ obtained from simulation.
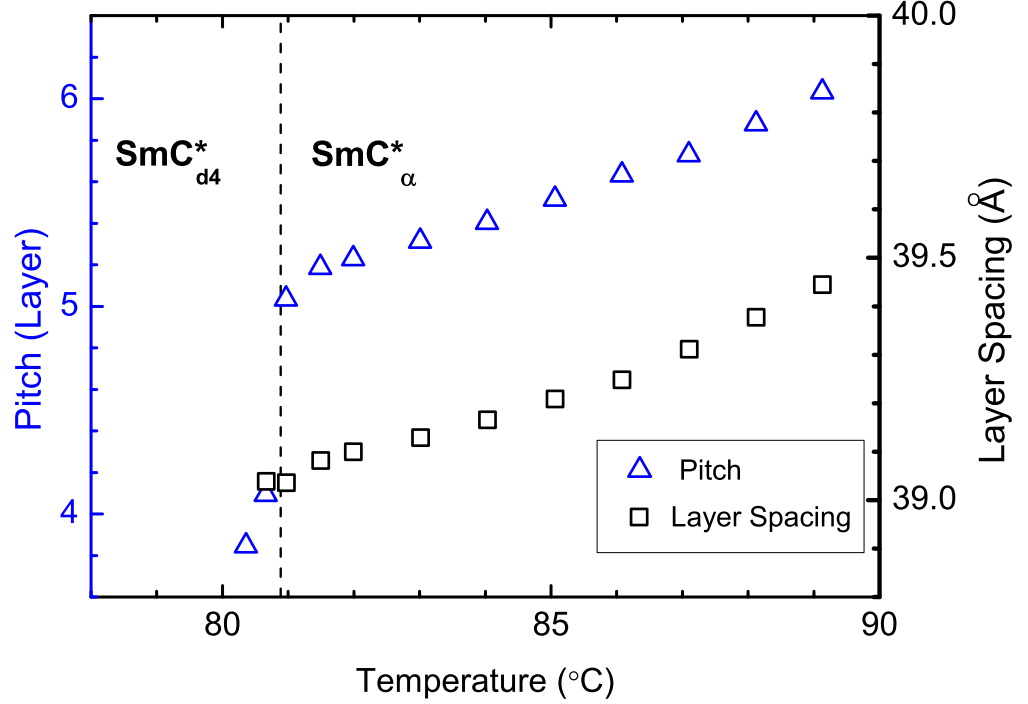
Figure 4.10: Temperature dependences of pitch (triangles) and layer spacing (squares) for the (73% 10OHF/27% 11OHF)$_{0.75}$ C9$_{0.25}$ mixture. Different phases are divided by dashed lines. No SmC$_{d6}^*$ phase is indentified in this mixture.

4.2   The (73% 10OHF/27% 11OHF)$_{0.75}$ C9$_{0.25}$ mixture

Another question we would like to address is the relationship between the SmC$_{d6}^*$ phase and the reversed SmC$_{d4}^*$-SmC* phase sequence. We have studied another ternary mixture (73%10OHF/27%11OHF)$_{0.75}$ C9$_{0.25}$ by RXRD (Fig. 4.10). The concentration of compound C9 is increased from 15% in Mixture A to 25% in this mixture. The phase reversal is still clearly visible but the SmC$_{d6}^*$ disappears. The pitch decreases from 6.03 to 5.03 layers in the SmC$_\alpha^*$ phase and then drops to 4.08 layers in the SmC$_{d4}^*$ phase. Pure 10OHF has the reversed phase sequence. However, by reviewing our high-resolution null transmission ellipsometry data of pure 10OHF [29], there is no indication of the SmC$_{d6}^*$ phase. Both mixtures exhibiting the SmC$_{d6}^*$ phase also display the phase reversal behavior. However, at least one mixture showing the reversed phase sequence does not have the SmC$_{d6}^*$ phase.

4.3 The 89% 10OHF/11% C11 mixture

4.3.1 Optical and RXRD studies
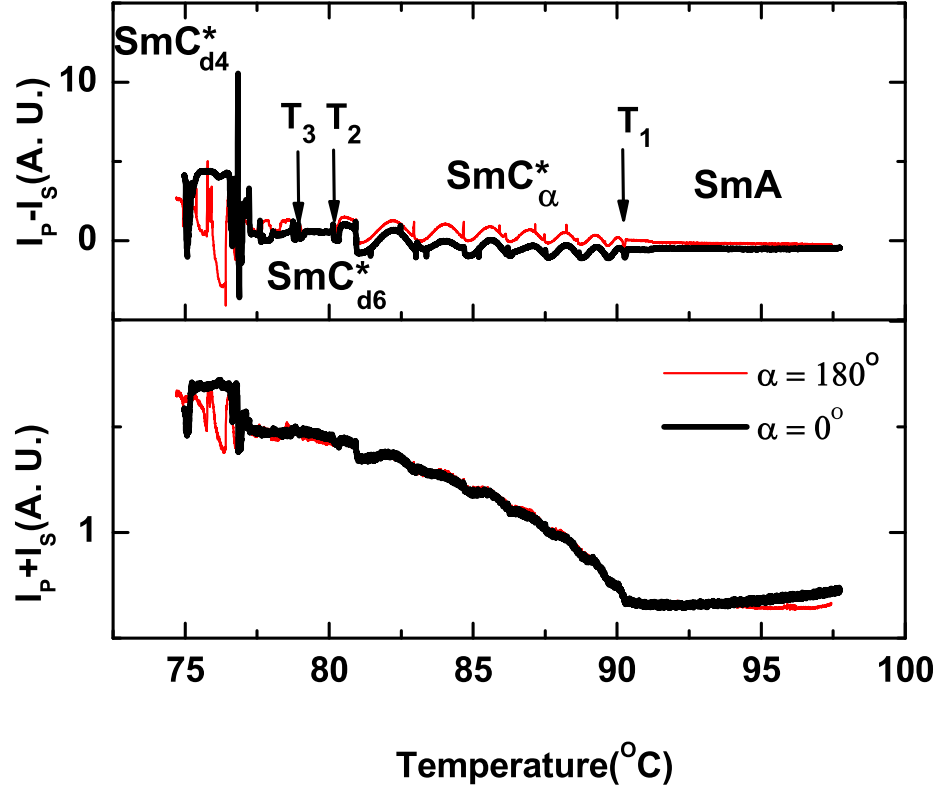
Figure 4.11: I_p-I_s and I_p+I_s as a function of temperature for a film of Mixture B from DOR while cooling at $0.1°C/min$. Arrows mark the transition temperatures. The thickness of the film is about 300 layers.

After going through all the old data associated with 10OHF and the reversed phase sequence, we found one mixture showing very similar pitch evolution as Mixture A. It is the 89% 10OHF/11% C11 mixture. The phase diagram of the 10OHF/C11 mixtures can be found in Ref. [32]. Figure 4.11 shows the DOR data for this mixture. Between T_1 and T_2 is the SmC^*_α phase. Between T_2 and T_3, the signals from α=0° and α=180° overlap and stay almost constant. It is the SmC^*_{d6} phase.

RXRD measurements (Fig. 4.12) confirms the SmC^*_{d6} phase. The temperature evolution of the pitch is very similar to that of Mixture A, changing linearly from 6.47 to 5.44 layers. The temperature range of the SmC^*_{d6} is slightly larger. A "noisy region"

also exists between the SmC^*_{d6} and SmC^*_{d4} phases. There are coexistences of the SmC^*_{d6} and SmC^*_α phases near the transition between them. One major difference from Mixture A is that no observable jump in layer spacing exists. It is somewhat expected because no change in the $I_p + I_s$ was observed at the SmC^*_α-SmC^*_{d6} transition.

Figure 4.12: Temperature dependences of pitch (triangles) and layer spacing (squares) for Mixture B. Different phases are divided by dashed lines. Noisy resonant signals are obtained in the regions between the SmC^*_{d6} and SmC^*_{d4} phases. It is called noisy region (N.R.). No pitch data are given in this region.

4.3.2 The coexistence of the SmC_α^* and the SmC_{d6}^* phases

Details of the coexistences of the SmC_{d6}^* and SmC_α^* phases in Mixture B are illustrated in Fig. 4.13. At T= 80.36 $^\circ C$, the main peak of the SmC_{d6}^* appears and coexists with the single peak of the uniaxial SmC_α^* phase of 5.48 layers. The intensity of the SmC_{d6}^* (SmC_α^*) peak increases (decreases) upon cooling. At $T = 80.04 \,^\circ C$, the split peaks of the SmC_{d6}^* phase are well developed. The data at this temperature again show that the SmC_{d6}^* phase and the SmC_α^* phase coexist. At $T = 79.94 \,^\circ C$, the SmC_α^* peak disappears and the entire film is in the SmC_{d6}^* phase.
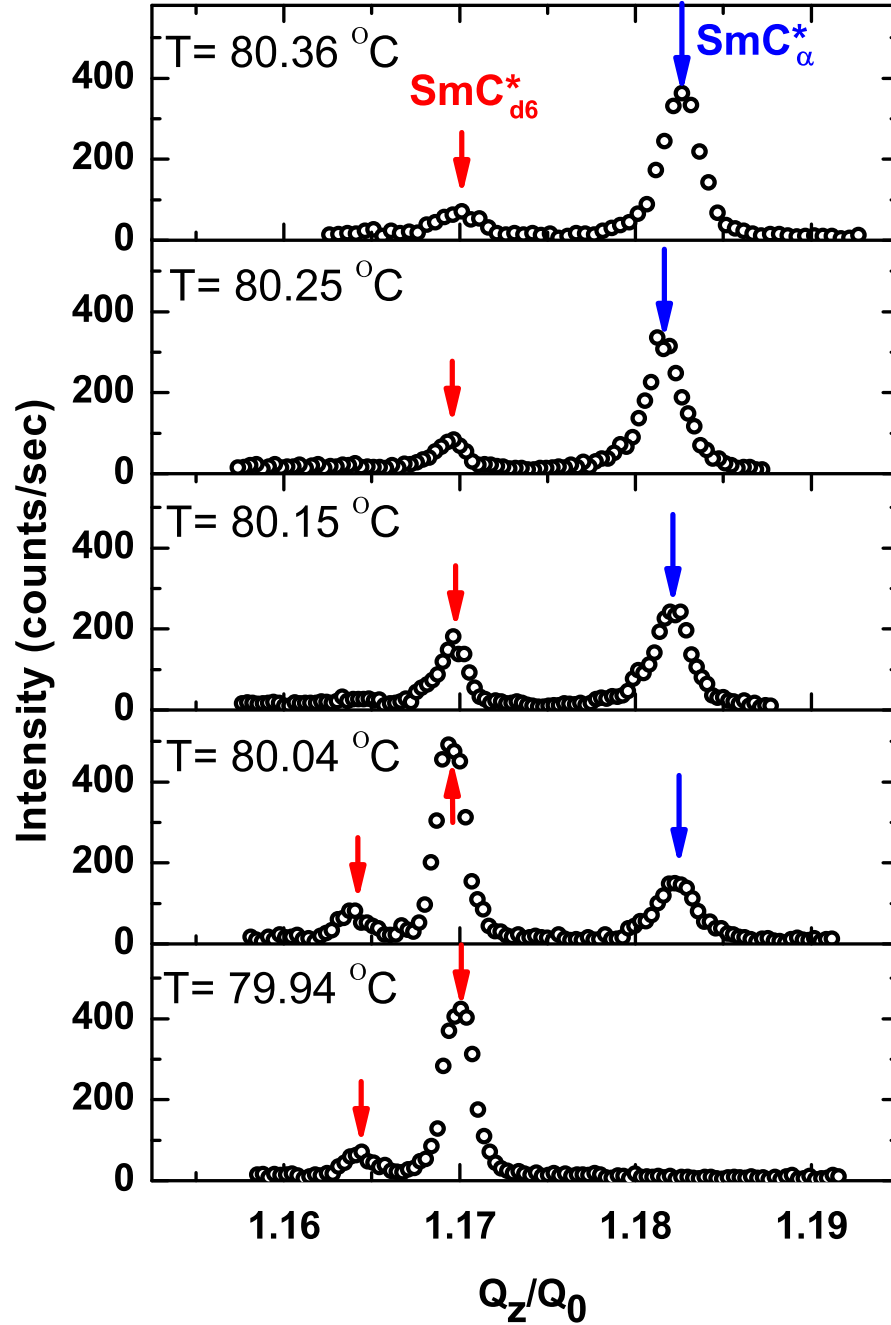
Figure 4.13: X-ray intensity scans in Mixture B at five different temperatures during the SmC$^*_\alpha$-SmC$^*_{d6}$ transition. Short red arrows and long blue arrows point to the peaks of the SmC$^*_{d6}$ phase and the SmC$^*_\alpha$ phase, respectively. The temperature range of the coexistence of the SmC$^*_\alpha$ and the SmC$^*_{d6}$ phases is about 0.4 $^\circ C$.

4.4   The temperature dependence of the distortion angle δ

The distortion angle δ in the SmC^*_{d6} phase does not change much with temperature in both Mixture A and B as shown in Fig. 4.14. The temperature dependence of the distortion angle in the SmC^*_{d6} phase is very similar to that in the SmC^*_{d4} phase, in which the distortion angle varies little with temperature [41]. In Mixture B, the distortion angle decreases towards the transition into the noisy region.
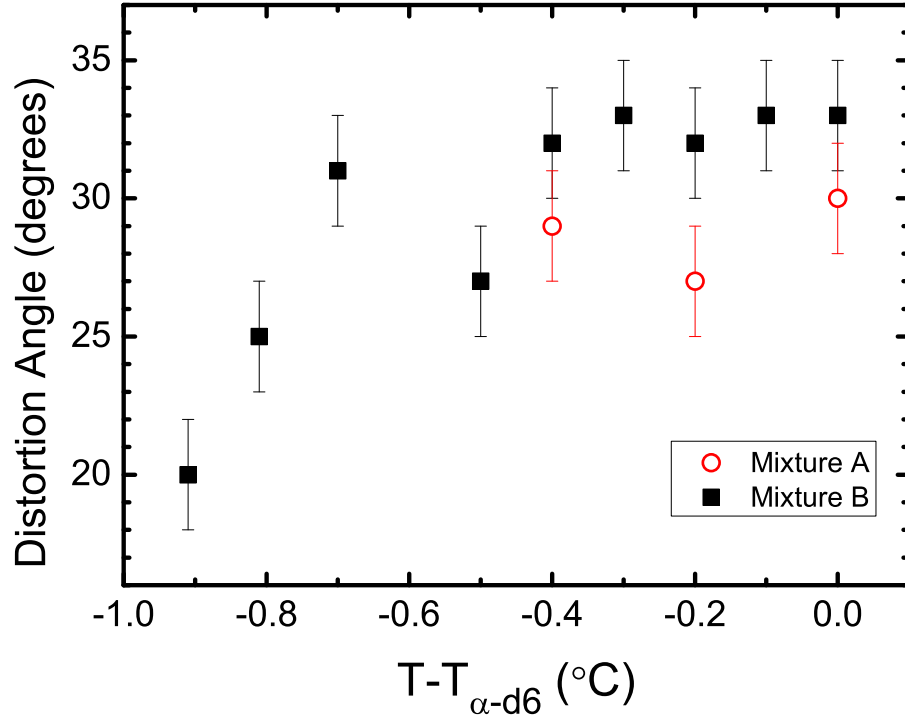
Figure 4.14: The distortion angle δ vs. temperature plot for Mixture A and B in the SmC^*_{d6} phase.

4.5 Other possible structures for the SmC_{d6}^* phase

Based on pure symmetry arguments, Osipov and Gorkunov [42] proposed three possible structures for a six-layer phase. They are shown in Fig. 4.15. All the three phases have 180° symmetry. Therefore, we could not rule any one out from NTE result. The first structure is the one we propose. We also want to present the simulation result for the second and third structure and explain why we think the first one is the right structure.
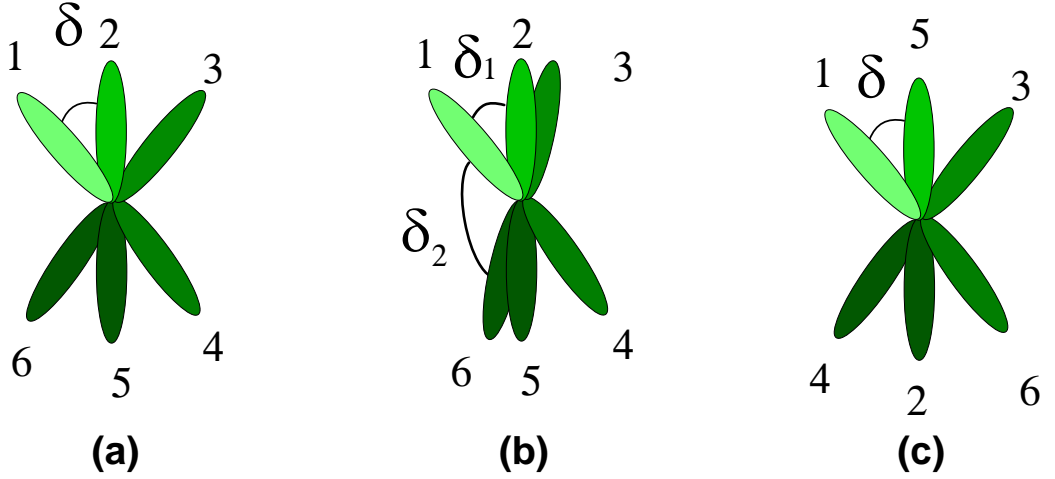
Figure 4.15: Three possible structures for a SmC* phase with six-layer periodicity.

The second structure has less symmetry than the first one. Instead of having one distortion angle, it has two. One extra parameter gives much more flexibility when doing the simulation. Figure 4.16 shows the fitting result by choosing $\delta_1 = 65°$, $\delta_2 = 110°$ and optical pitch = 350 layers. However, this is not the only combination of δ_1 and δ_2 that gives good fitting result. Just from the experimental data, it is impossible to say this structure is unlikely. However, this structure is not favorable in theoretical models that have generated the six-layer phase, which will be discussed in the next section.

The third structure looks very similar to the first one. However, it does not look like the right structure at the first glance. It would take too much energy to rotate the molecules in the adjacent layers by such a big angle, in particular just below the SmC_{α}^* phase. Indeed, the simulation indicates very different result from the experimental
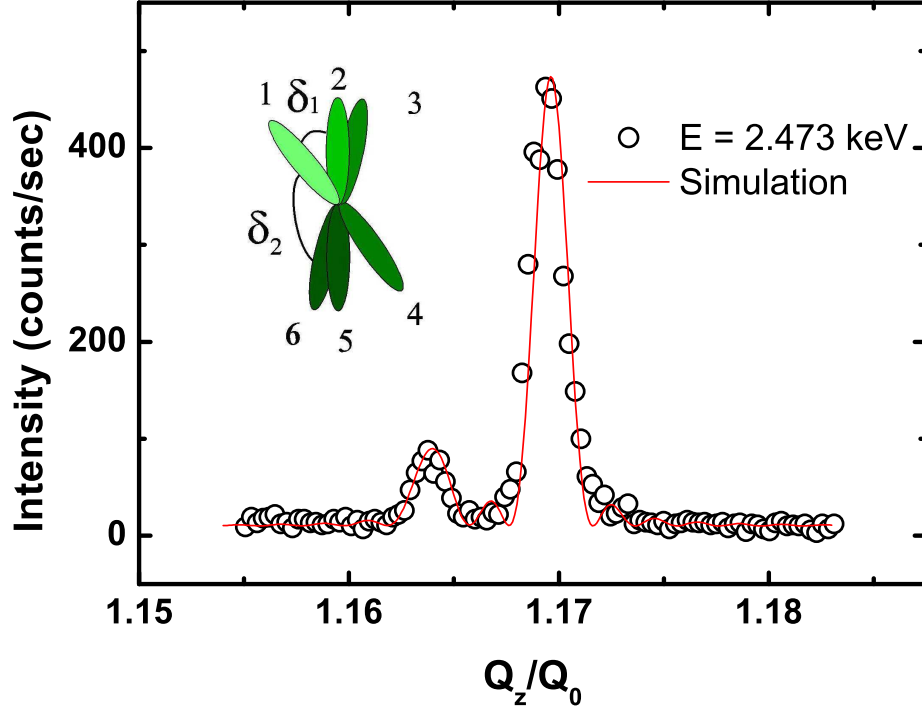
Figure 4.16: The resonant satellite peak (circles) from Mixture B at 78.45 $^\circ C$ and the simulation (line). The center of the split peaks is located at $Q_z/Q_0 = 1.167$, corresponding to a pitch of six layers. The split peaks indicate a distorted structure. The positions and intensities of the two peaks give an optical pitch of 350 layers (1.36 μm) and a distortion angle δ_1 of 65° and δ_2 of 110 °. The simulation has been normalized to match the measured intensities. The cartoon is the structure used in our simulation.

data, as seen in Fig 4.17. Instead of having split peaks, the simulation yields four peaks centered at $Q_z/Q_0 = 1.167$ for both δ values. Thus this structure can be completely ruled out.
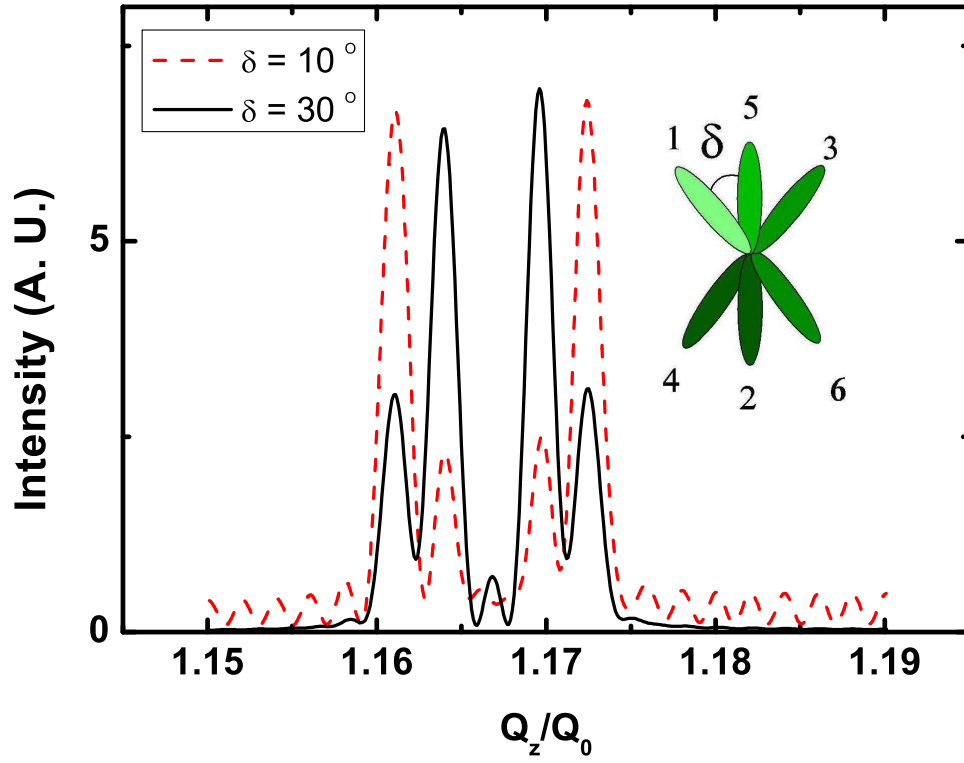
Figure 4.17: The simulation result from the third structure with $\delta = 10°$ and $30°$. Notice the distortion angle δ is defined as the angle between the first and fifth layer in this structure. The cartoon is the structure used in our fitting.

4.6   Discussion

To date, the liquid crystal phase having six-layer periodicity has been proposed by
three research groups. Yamashita [36] predicted a six-layer phase as a part of the
devil's staircase structure which has not been confirmed experimentally. By relaxing
the requirement of the uniformity of tilt angles among different layers, the theoretical
advance by Dolganov *et al.* [39] yielded a mesophase having six-layer periodicity. So far,
the layer spacing variation among different layers has not been observed experimentally.
In particular, our acquired layer spacing variations do not support such an assumption.
Finally, the results from Hamaneh and Taylor [37, 38] do not offer any structural infor-
mation of the six-layer phase. We will discuss the latter two models in more detail in
this section together with the new simulation results we obtained based on a discrete
model.

4.6.1   The work by Dolganov *et. al*

Dolganov *et. al* [39] propose a discrete phenomenological model of antiferroelectric
liquid crystals to study the structures and phase transitions in bulk samples and thin
films. The free energy they use, which contains only the nearest-neighbor and the
next-nearest-neighbor layer interactions, reads

$$G = \sum_i [\frac{1}{2}a_0 \vec{\xi}_i^2 + \frac{1}{4}b_0 \vec{\xi}_i^4 + \frac{1}{2}a_1 \vec{\xi}_i \cdot \vec{\xi}_{i+1} + \frac{1}{8}a_2 \vec{\xi}_i \cdot \vec{\xi}_{i+2} + f(\vec{\xi}_i \times \vec{\xi}_{i+1})_z] \quad (4.1)$$

$a_0 = \alpha (T\text{-}T^*)$ and b_0 are Landau coefficients describing the SmA to SmC transition
in noninteracting layers. The third term is the nearest neighbor layer interaction. This
contribution to the energy stabilizes the synclinic structures (SmC*) for negative a_1 and
anticlinic structures (SmC$_A^*$) for positive a_1. The a_2 term is the next-nearest-neighbor
layer interaction. The f term describes the chiral interaction. Figure 4.18 shows the
phase diagram generated by minimizing Eq. 4.1. In this phase diagram, all the SmC*
variant phases are present together with a six-layer phase. They claim that in the three-
and six-layer phase, unlike the others, both the modulus and phase of $\vec{\xi}_i$ changes with
the layer number i. It means that not only the azimuthal angle ϕ but also the tilt angle
θ in Fig. 1.2 are different in different layers. From our experimental results (Fig. 4.3

and 4.12), no such tilt angle variation is observed. They also suggest non-resonant peaks due to this interlayer variation of the tilt angle at $Q_z/Q_0 = 1.333$. We did not have a chance to check this during our recent RXRD run. This is one of the experiments we would like to perform in the future. We have mapped the observed phase sequence in Mixture A and B onto the phase diagram represented by the red curve with arrow in Fig. ??. The quantity a_1/a_2 has to vary nonmonotonically and the red curve must cross the six-layer phase twice which disagree with our experimental observation.
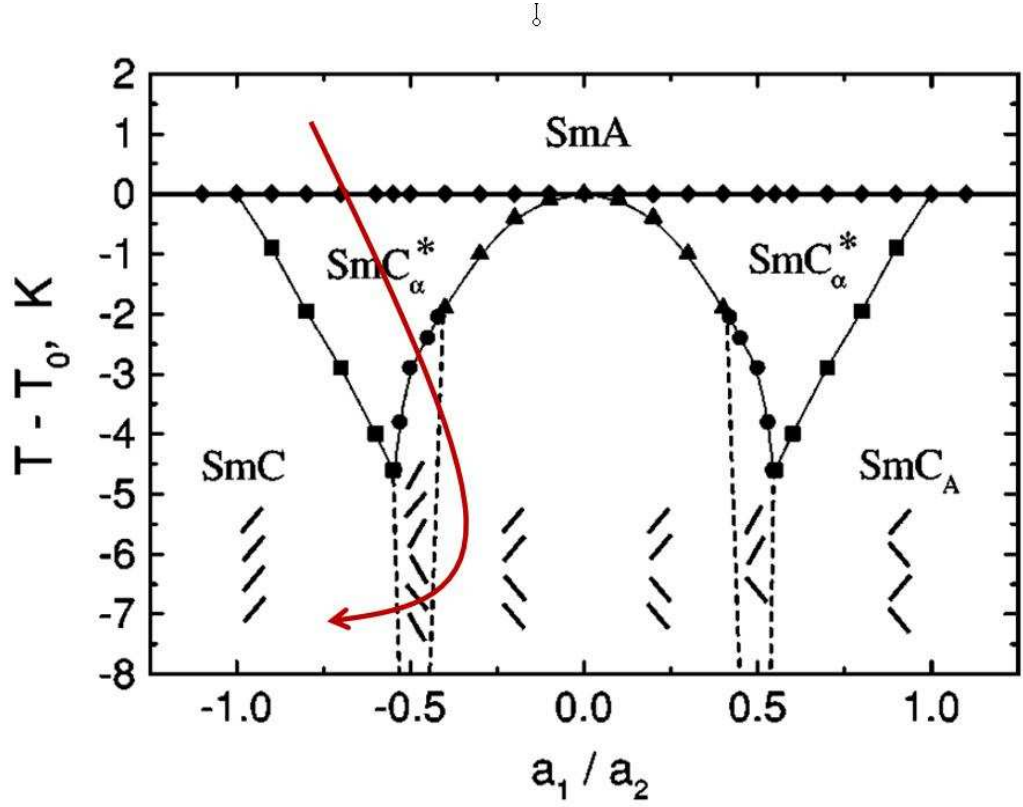
Figure 4.18: Phase diagram proposed by Dolganov *et. al* in Ref. [39]. T_0 is the temperature of the transition from the SmA to tilted phases. The set of model parameters is $\alpha = 0.01~K^{-1}$, $a_2 = 0.02$, $a_3 = 0.05$. A schematic representation of the tilted structures appearing below the SmC_α^* phase is shown in the lower part of the figure. The red curve is the phase sequence of Mixture A and B mapped onto the phase diagram. In order to reach the SmC phase below the SmC_{d4}^* phase, the red curve needs to cross the 6-layer region again, which is contradictory to our results. a_1/a_2 has to be varied nonmonotonically in order to achieve the phase sequence.

4.6.2 The Hamaneh-Taylor model

The idea of competition between short- and long-range interlayer interactions which result in structures locked to commensurate periods was considered by Hamaneh and Taylor [37, 38]. The short range interaction is limited to the nearest neighbor layer. The contribution of the short-range interaction to the free energy is described as

$$V_{sr} = \frac{v_{sr}}{Nd} \sum_l cos(\phi_{l+1} - \phi_l - \alpha) \tag{4.2}$$

v_{sr} is the strength of the short range interaction. N is the layer number and d is the thickness of the layer. ϕ_l is the azimuthal angle of the lth layer. α is the preferential angle formed by tilt in neighboring layers, whose origin is not discussed in their papers. They proposed that interactions to more distant layers originate in bending fluctuations of smectic layers. They took into account the anisotropy of elastic constants for bending of smectic layers, which is a consequence of the anisotropic molecular tilt order in the smectic layer explicitly. The contribution of the long-range interaction to the free energy is

$$V_l = -\eta J^2 \tag{4.3}$$

The new order parameter J is defined as

$$J = \frac{1}{N} \sum_l cos2\phi_l \tag{4.4}$$

By minimizing the free energy (sum of the short and long rang interactions), a phase diagram in the α-η plane is generated as shown in Fig. 4.19. All the SmC^* variant phases can be identified in the phase diagram as well as a six-layer phase. Unfortunately, in their papers no detailed structure for the six-layer phase was given. Again, we cannot map the phase sequence of Mixture A and B onto the phase diagram without varying α nonmonotonically, which is not supported by the theory. Even so, the phase sequence must cross the six-layer region twice.
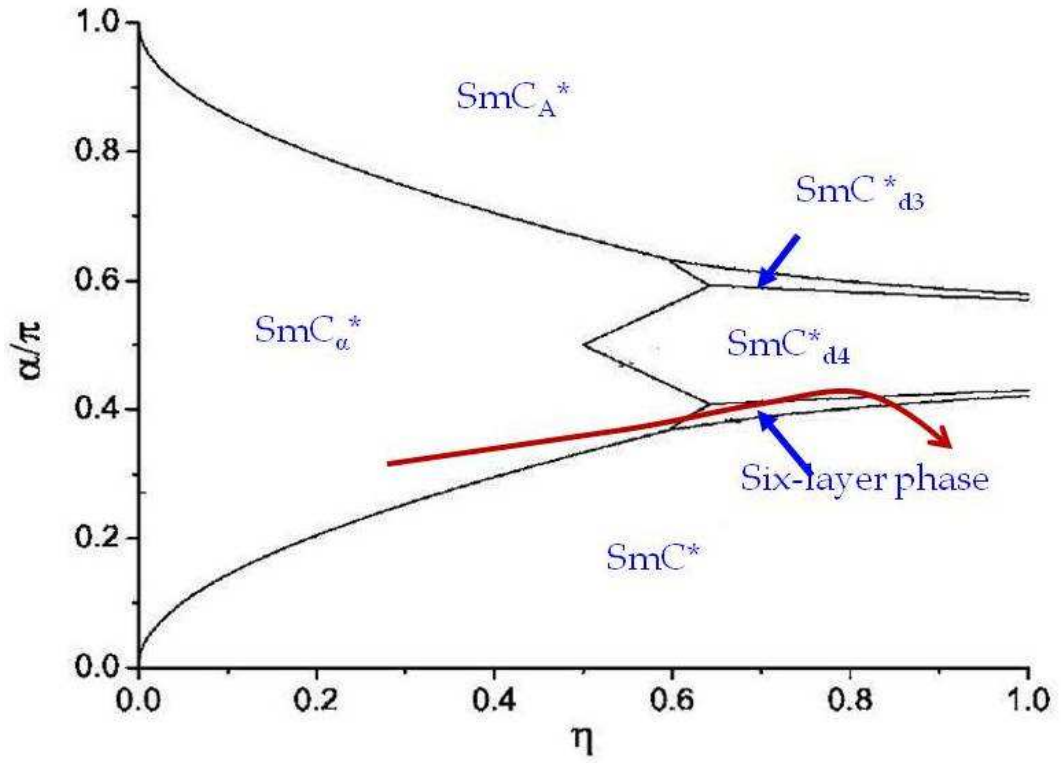
Figure 4.19: Phase diagram proposed by Hamaneh and Taylor in Ref. [37, 38]. The parameters α and η represent the strength of the short-range and effective long-range interactions. The red curve is the phase sequence of Mixture A and B mapped onto the phase diagram. In order to reach the SmC phase below the SmC$^*_{d4}$ phase, the red curve needs to cross the 6-layer region again, which is contradictory to our results. α has to be varied nonmonotonically in order to achieve the phase sequence.

4.6.3 Simulation based on the discrete model

Our group has also tried to carry out simulations based on a phenomenological model proposed by Cepic and Zeks [44]. In their original model, the authors have considered both polar and tilt ordering and shown that effective interactions up to fourth-nearest neighbor can be significant. However, Olson *et. al* [45] found that only interactions up to the third-nearest neighbor are needed to stabilize the five SmC* variant phases. They have been able to reduced the free energy to five terms as following.

$$G = \sum_{j=1}^{N} (\sum_{i=1}^{3} a_i (\overrightarrow{\xi}_j \cdot \overrightarrow{\xi}_{j+1}) + f(\overrightarrow{\xi}_j \times \overrightarrow{\xi}_{j+1})_z + b(\overrightarrow{\xi}_j \cdot \overrightarrow{\xi}_{j+1})^2) \qquad (4.5)$$

a_1, a_2, a_3 terms are the nearest, next-nearest, and third-nearest-neighbor layer interactions. b has to be negative to favor the "Ising-like" arrangement. f term is the chiral interaction which is usually weak.

With the parameters a_3 = -0.2, f = 0.12 and b = -0.4, a phase diagram in the a_1 and a_2 space is simulated as shown in Fig 4.20. It includes the SmC^*_α, SmC^*, SmC^*_{d4}, SmC^*_{d3} and SmC^*_A phases. No SmC^*_{d6} is identified. In order to simulate the SmC^*_{d6} phase, Moths *et. al* [46] decide to change the sign of a_3 from negative to positive . The reason for it is that unlike in the SmC^*_{d3} phase, in the SmC^*_{d6} phase the third nearest neighbors always favor anticlinic arrangement (see Fig 4.7). Therefore, changing a_3 from negative to positive would suppress the SmC^*_{d3} phase and promote the SmC^*_{d6} phase. The result indeed support the conjecture. As shown in Fig. 4.21, when a_3 is changed from -0.2 to 0.2 the SmC^*_{d6} phase emerges in the phase diagram at the expense of the disappearance of the SmC^*_{d3} phase. Thus we conclude that one necessary condition for the stabilization of the SmC^*_{d6} phase is that the interaction between the third nearest neighbor layer has to be antiferroelectric like. However, one problem with this model is that we have to vary the parameters a_1, a_2 and a_3 simultaneously in order to realize the phase sequence observed in Mixture A and B.

Figure 4.20: Phase diagram generated by Olson *et. al* using the free energy Eq. 4.1 with $a_3 = $ -0.2, $f = 0.12$ and $b = $ -0.4. The SmC^*_α, SmC^*, SmC^*_{d4}, SmC^*_{d3} and SmC^*_A are present in the phase diagram.
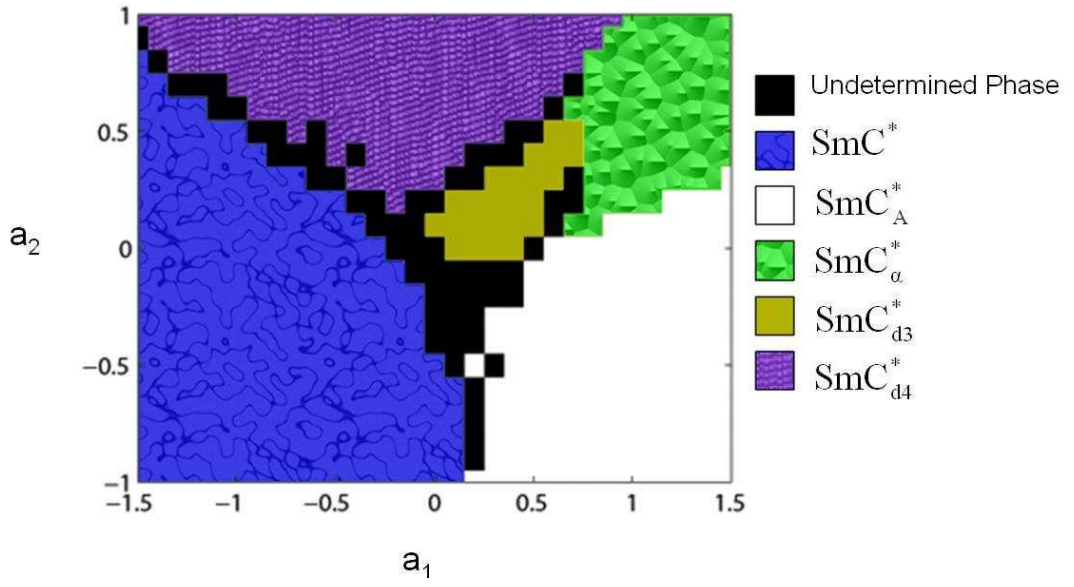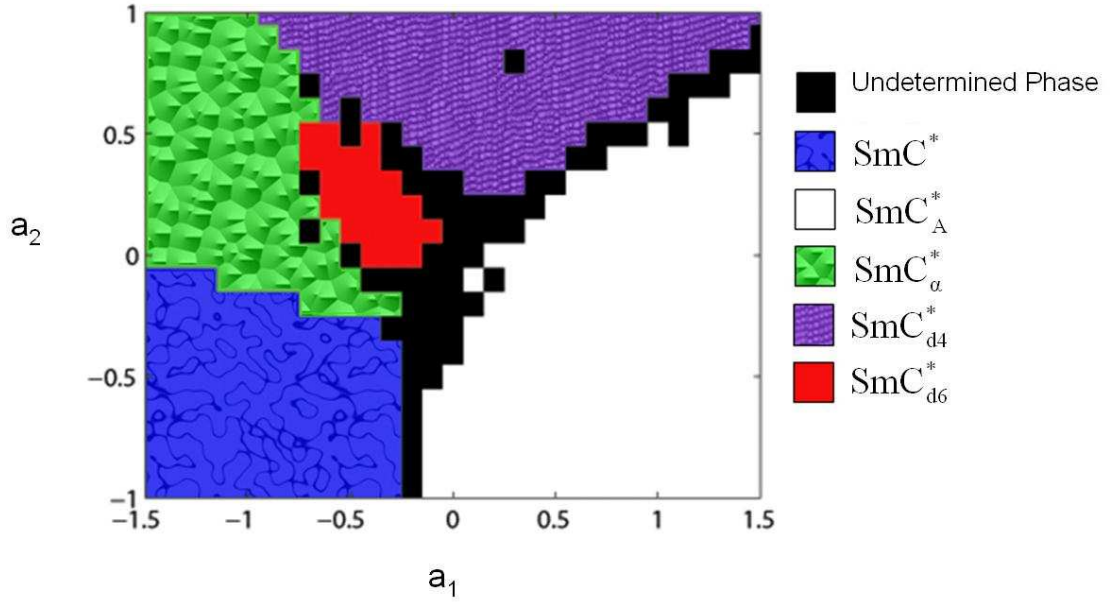
Figure 4.21: Phase diagram generated by Moths *et. al* using the free energy Eq. 4.1 with $a_3 = 0.2$, $f = 0.12$ and $b = $ -0.4. the SmC^*_{d6} phase emerges in the phase diagram at the expense of the disappearance of the SmC^*_{d3} phase.

4.7   Summary

The nature of the long-range interaction in liquid crystals has been a long standing question in condensed matter physics. Two research groups have tried to address the physical origin of the long range order and establish the stability of phases having periodicity larger than four layers. Hamaneh and Taylor [37, 38] propose that thermal fluctuations in the shape of the smectic layers translate into an effective long-range interaction. However, we cannot map the acquired pitch evolution from both mixtures shown in Fig. 4.3 and 4.12 into their phase diagrams without varying two relevant parameters nonmonotonically (see Fig. 4.18 and 4.19), which is clearly forbidden in the model. The long range interaction proposed by Emelyanenko and Osipov [43] is induced by the "discrete" flexoelectric effect. The importance of flexoelectric effect in stabilizing the SmC^* variant phases was first discussed by Cepic and Zeks [44]. Unfortunately, only mesophases with periodicity of 8-, 5-, 7- and 9-layer are predicted between the SmC^* and SmC_A^* phases upon cooling. The six-layer phase is absent which is contradictory to our experimental findings. Thus the physical origin of the long range interaction for phases with a long periodicity (e.g. SmC_{d6}^* phase) remains unsolved.

To summarize, we have discovered a novel biaxial six-layer SmC_{d6}^* phase. Although a phase with 6-layer periodicity was predicted, its measured biaxial structure and phase behavior were unexpected and beyond the current theoretical understanding. The discovery of this phase extends the range of the commensurate long range order in the SmC^* variant phases from four layers to six layers. Our findings point out the need for a theory that could describe the structures of all SmC^* variant phases including the SmC_{d6}^* phase and generate a phase diagram that explains the associated phase sequence.

Chapter 5

Effect of Molecular Shape on the Stability of Smectic-C* Variant Phases

In all the theories describing the SmC* variant phases, liquid crystal molecules are simplified as rods [4, 5]. The shape of the liquid crystal molecule has never been taken into consideration. In this section, we investigate the effect of molecular shape on the stability of the SmC* variant phases by mixing a well studied antiferroelectric compound MHPBC [47, 48] with two achiral liquid crystal compounds showing very different molecular shapes. Except overall reduction in chirality, achiral dopants will not yield any unexpected chiral interactions between different chiral molecules. We present two phase diagrams as a function of doping concentrations that clearly show the influence of steric interaction on the stability of SmC* variant phases.

5.1   Studied compounds

Figure 5.1 shows the chemical structures and three-dimensional models of the investigated compounds. MHPBC has all the SmC* variant phases except the SmC* phase. From the three-dimensional model, one can immediately see that the molecular shape of MHPBC resembles the molecular shape of the hockey-stick like sf-7 more than that of

the rod-like $\bar{8}$S5. In fact, it has been demonstrated by polarized infrared spectroscopy [49] as well as x-ray diffraction measurements [50] that in one antiferroelectric compound there is a significant angle between the chiral chain and the core axis. There is also evidence from steric and optical tilt measurements that the alkyl chains are bent in the SmC* variant phases in several antiferroelectrics [51]. Two achiral dopants are $\bar{8}$S5 and sf-7. $\bar{8}$S5 is a simple rod-like molecule which shows the synclinic SmC phase. sf-7 is a hockey-stick shaped compound with the SmC phase and the anticlinic SmC_A phase [52, 53, 54]. If the bend in the molecular structure in MHPBC plays an important role in stabilizing the SmC* variant phases, one would expect that mixtures of MHPBC with $\bar{8}$S5 and sf-7 to show completely different results.
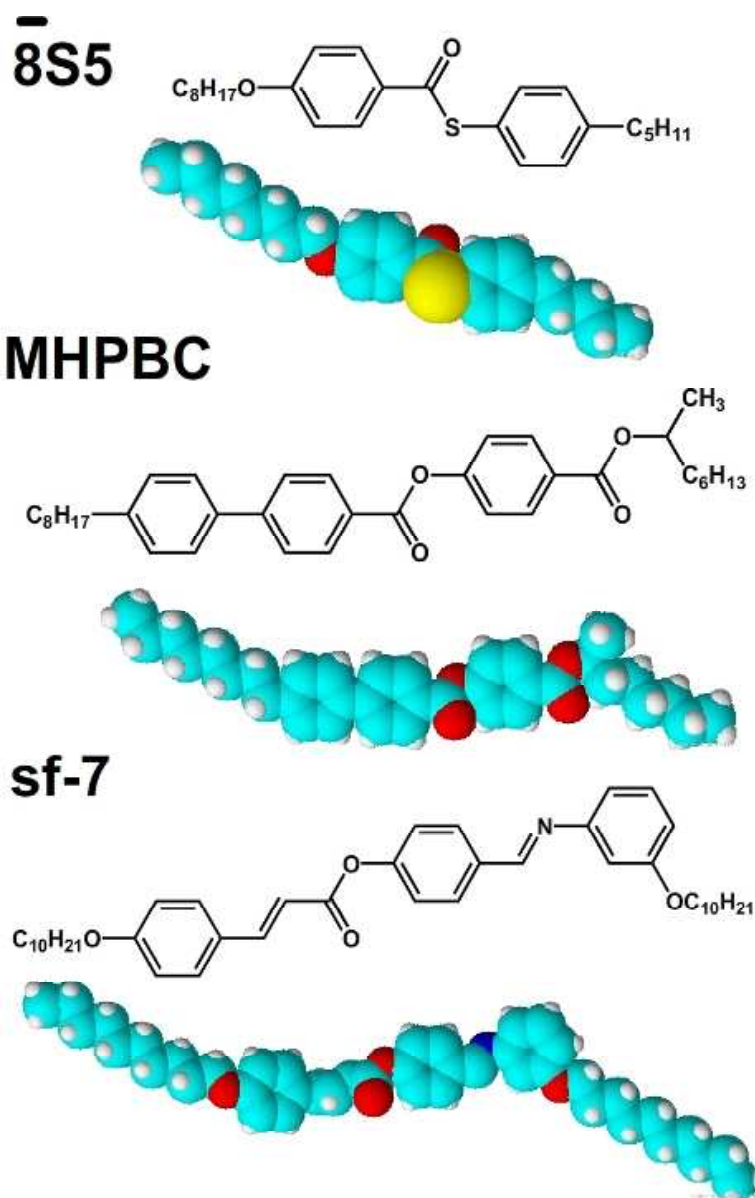
Figure 5.1: The molecular structures and the 3D models of the studied compounds. The phase sequences of these compounds are: MHPBC, Isotropic (109 °C) SmA (76 °C) SmC^*_α (71 °C) SmC^*_{d4} (66 °C) SmC^*_{d3} (62 °C) SmC^*_A (51 °C) Crystal. $\bar{8}S5$, Isotropic (87 °C) Nematic (63 °C) SmA (56 °C) SmC (31 °C) Crystal. sf-7, Isotropic (101 °C) SmA (99 °C) SmC (93 °C) SmC_A (71 °C) Crystal.

5.2   Results

We have prepared eleven mixtures of $\bar{8}$S5 and MHPBC with 1, 2, 3, 4, 5, 6, 9, 15, 40, 70 and 95% $\bar{8}$S5 in MHPBC and eleven mixtures of sf-7 and MHPBC with 5, 10, 15, 20, 35, 50, 55, 60, 65, 70 and 75% sf-7 in MHPBC. The primary experimental method employed to determine the phase sequences of MHPBC and mixtures was DOR.

Figure 5.2 shows the DOR data from films of mixtures of 1, 2, 3, and 4% $\bar{8}$S5 in MHPBC. Previous detailed studies of MHPBC by DOR and NTE [47] provide an excellent guide for our phase identifications. The clearing and crystallizing temperatures are determined by polarising optical microscopy in device geometry.
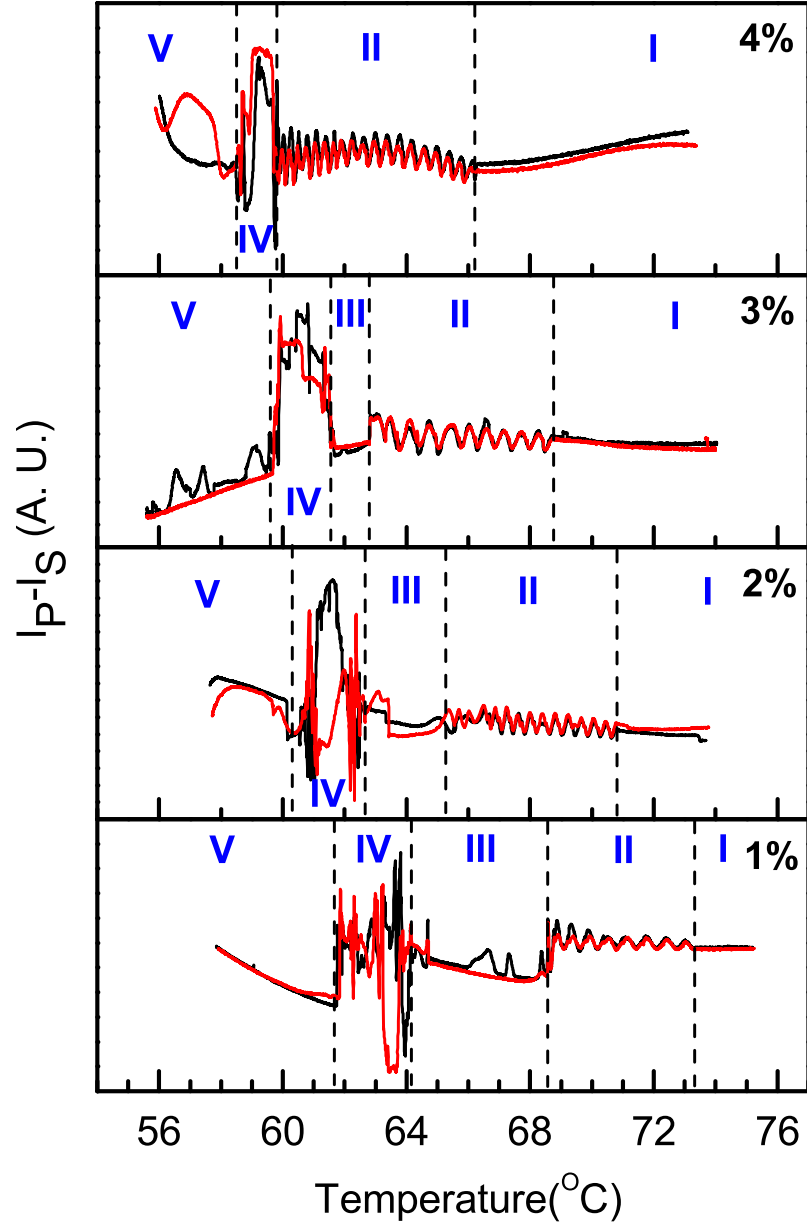
Figure 5.2: DOR data from films of mixtures of 1, 2, 3 and 4% $\bar{8}$S5 in MHPBC. The red data were taken with the angle between the electric field and the incident plane equaled to 0° and the black data were obtained when this angle was 180°. The Roman numbers represent the phases in the following way: I (SmA), II (SmC$_\alpha^*$), III (SmC$_{d4}^*$), IV (SmC$_{d3}^*$), V (SmC$_A^*$). The thicknesses of the films were between 200 to 300 layers.
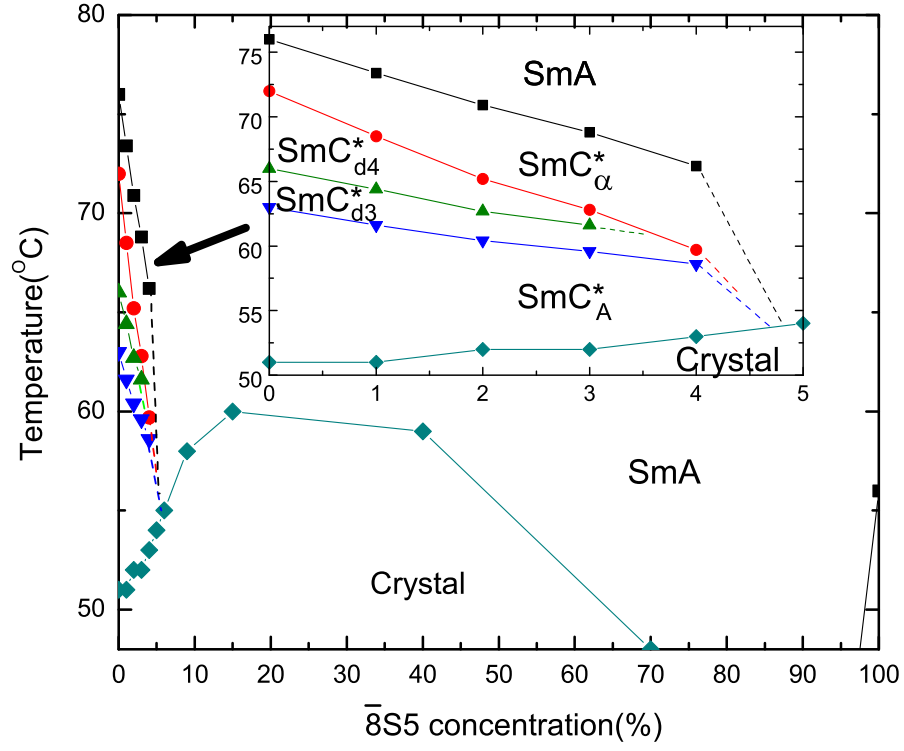
Figure 5.3: The phase diagram for $\bar{8}$S5 and MHPBC mixtures. The SmA-SmC* transition temperatures of the 95% $\bar{8}$S5 mixutre is very low thus not shown in the diagram. The nematic phase on the $\bar{8}$S5 rich side is not shown because we are not interested in the nematic phase.

Figure 5.3 illustrates the phase diagram summarizing the transition temperatures obtained from DOR and polarizing optical microscopy for the $\bar{8}$S5 and MHPBC mixtures. The clearing temperature curve (not shown in the diagram) is almost linear, connecting the clearing points of the two pure compounds. On the MHPBC rich side, the SmA to SmC$_\alpha^*$ transition temperature decreases with doping. This suggests a reduction in the strength of the steric interaction which drives the SmA to SmC$_\alpha^*$ transition. The crystallizing temperature increases with doping. The decrease in the SmA-SmC$_\alpha^*$ transition temperature and the increase in the crystallizing temperature cause the temperature range of the SmC* variant phases to shrink as the doping concentration increases. There is no SmC$_{d4}^*$ phase in the 4% mixture, in which the SmC$_\alpha^*$, SmC$_{d3}^*$ and SmC$_A^*$ phases are still present. Up to 4% doping, the temperature ranges of the SmC$_{d4}^*$ phase and the SmC$_A^*$ phase decrease with increasing dopant concentration. Upon doping the temperature range of the SmC$_{d3}^*$ phase stays more or less constant, while that of the SmC$_\alpha^*$ phase expands. In the 5% mixture, all the SmC* variant phases abruptly disappear. Between 5 and 75% doping concentration, the SmA phase is the only phase between the isotropic and crystalline phases. On the $\bar{8}$S5 rich side, the SmA to SmC* transition temperature also decreases very quickly with increasing MPHBC concentration. In the 95% $\bar{8}$S5 mixture, the SmA-SmC* transition temperature is 35°C compared to the SmA-SmC trasition temperature of 56°C in pure $\bar{8}$S5.

The phase diagram of the sf-7 and MHPBC mixtures is shown in Fig. 5.4. The clearing temperature curve is similar to that of the $\bar{8}$S5 and MHPBC system. Other than that, the two phase diagrams are very different. On the MHPBC rich side, the crystallizing temperature is slightly suppressed by doping. Although the SmA to SmC$_\alpha^*$ transition temperature goes down with increasing amount of dopant, it is at a much slower rate than the MHPBC/$\bar{8}$S5 mixtures. As a result, the total temperature range of the SmC* variant phase does not change much with doping. The temperature ranges of the SmC$_\alpha^*$ phase and the SmC$_A^*$ phase increase with doping, at the expense of both the SmC$_{d4}^*$ and SmC$_{d3}^*$ phases. The SmC$_{d4}^*$ and SmC$_{d3}^*$ phases disappear in the mixtures with more than 10% doping. The SmC$_\alpha^*$ phase and SmC$_A^*$ phase propagate throughout the phase diagram. The temperature range of the SmC$_\alpha^*$ phase becomes very small in the intermediate doping. The SmC$_\alpha^*$ phase turns into the SmC* phase around 75% doping. This is not surprising because it has been demonstrated by Liu *et al.* that without

change in symmetry, the SmC_α^*-SmC^* transition is a first order transition ending at a critical point [55], just like the liquid/gas transition. Thus it is possible to have a continuous evolution from the SmC_α^* to the SmC^* phase beyond the critical point. To the best of our knowledge, this is the first experimental indication of a possible continuous evolution between the SmC_α^* and the SmC^* phase. More experimental work is required to confirm this important observation. It is also reasonable that adding the chiral compound MHPBC into sf-7 makes the achiral SmC phase become the chiral SmC^* phase.

The SmC_A^* phase in MHPBC is largely enhanced by sf-7 doping. Its temperature range reaches 34 K at 75% doping, which is larger than the 11K in MHPBC and 22K in sf-7.
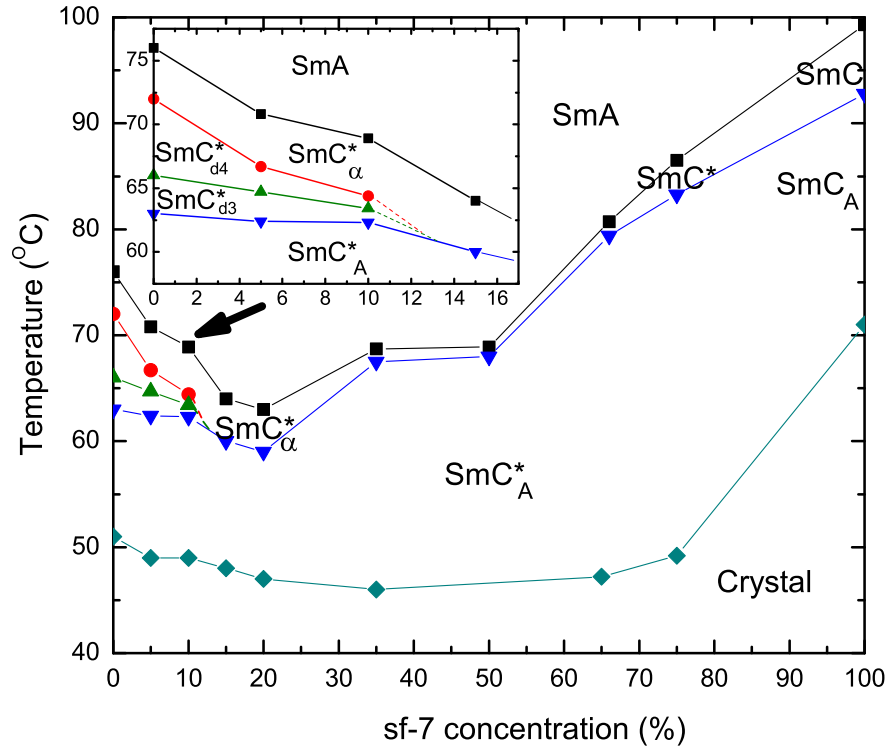

Figure 5.4: The phase diagram for the sf-7 and MHPBC mixtures.

5.3 Discussion

The study of the two mixture systems have shown that the rod-like molecule $\bar{8}$S5 is much more destructive to the SmC* variant phases in MHPBC than the hockey-stick-shaped sf-7. None of the SmC* variant phases is miscible with the SmC phase in $\bar{8}$S5. On the other hand, the SmC*$_\alpha$ and the SmC*$_A$ phases in MHPBC are miscible with the SmC phase and the SmC$_A$ phase in sf-7. Recently, Enz *et al.* [56] reported the miscibility of the SmC* phase and the SmC*$_A$ phase in two antiferroelectric compounds with the SmC phase and the SmC$_A$ phase in one hockey-stick compound. No other SmC* variant phases appear in the reported mixtures.

The disappearance of the SmC*$_{d4}$ and SmC*$_{d3}$ phases in the MPHBC and sf-7 mixtures in less than 15% doping can be reconciled by the phase diagram presented by Olson *et al.* [45] based on the discrete model proposed by Cepic *et al.* [44]. In the phase diagram, the SmC*$_{d4}$ and SmC*$_{d3}$ phases emerge when the coefficient a_1 of the effective nearest neighbor layer interaction is near zero. When adding sf-7, both the SmC*$_{d4}$ and SmC*$_{d3}$ phases disappear and only SmC*$_\alpha$ and the SmC*$_A$ phases are stable. This suggests that the coefficient a_1 changes from being approximately zero to a positive value. For large positive a_1 value, only SmC*$_\alpha$ and SmC*$_A$ exist. In most of the theoretical models, it is believed that the steric interaction in the antiferroelectric compound stabilizes the ferroelectric ordering [44, 42]. However, the fact that antiferroelectric SmC*$_A$ phase in MHPBC is greatly enhanced by mixing with a compound that is similar in shape suggests that the steric interaction could also be in favor of antiferroelectric ordering.

It has been argued that in order to reduce the electrostatic interaction energy, antiferroelectric arrangement is found in many liquid crystal compounds showing large polarization. In investigating the enantiomeric effect on the stability of the SmC* variant phases [47, 48], it has been demonstrated that the SmC$_A$ phase is stable even in the racemic mixture, which strongly indicates that the electro-static interactions alone cannot explain the stability of the SmC*$_A$ phase. In this work of binary mixtures, we clearly demonstrate the importance of the molecular shape, namely steric interaction, in enhancing the stability of the SmC*$_A$ phase.

Liquid crystal mixtures displaying antiferroelectric response have been used for electro-optical device applications showing fast switching rates [4]. In this research

work, we have discovered a significant increase in the temperature window of the SmC_A^* phase in the mixture of MHPBC with a hockey-stick compound, sf-7. The large SmC_A^* temperature window will, in general, facilitate the device applications. Because sf-7 compound is achiral, it would be extremely important to study the threshold voltage and switching rate of the SmC_A^* to the SmC^* under the applied electric field. Unfortunately, we do not have enough samples for such measurements requiring device-cell geometry and a large amount of samples. New hockey-stick shaped compounds have been reported recently [57]. We plan to extend our research work of studying the stability of the SmC^* variant phases to other binary mixtures involving antiferroelectric liquid crystal compounds and other compounds, in particular, the new hockey-stick compounds.

5.4 Conclusion

To conclude, we have investigated the effect of steric interaction on the stability of the SmC^* variant phases. Doping one antiferroelectric compound with achiral compounds having different shapes gives dramatically distinct results. The hockey-stick compound stabilizes the SmC^* variant phases while the rod-like compound destroys them. It shows the importance of steric interaction in stabilizing the SmC^* variant phases.

Chapter 6

Conclusion and Future Works

The primary research goal of this thesis is to investigate the orientational order in the chiral smectic liquid crystals showing the SmC* variant phases. The study of the reversed SmC_α^*-SmC_{d4}^*-SmC* phase sequence is certainly interesting because a phase of higher symmetry appears at a lower temperature than the phase with lower symmetry, which is counterintuitive. So far, the only compound showing this behavior is 10OHF [29, 32]. In Chapter 3, the mixtures of 10OHF and its homologs are thoroughly characterized. The SmC_{d4}^* phase is eleminated upon large 9-, 11-, 12-OHF doping. Mixtures of nOHF and Cn are also studied. However, no phase reversal is identified in mixtures other than those with 10OHF. It confirms the uniqueness of 10OHF. 11OHF, which displays no SmC_{d4}^* phase, has the ability to promote the SmC_{d4}^* in the binary and ternary mixtures with Cn. The further pursuit of the reversed phase sequence has lead to a great discovery, the SmC_{d6}^* phase, which is discussed in Chapter 4. The experimental evidences found in two mixtures are solid and unambiguous. The orientational order in the SmC_{d6}^* phase is clearly revealed by optical and RXRD studies along with computer simulations. The discovery of this new phase and the identification of its structure sets another milestone in the research of chiral smetic liquid crystals. None of the existing theories is able to explain the physical properties associated with this new phase. Our discovery challenges the theorist to revise their models and probably to look for new mechanism for the interactions in chiral smectic liquid crystals. In Chapter 5, the impact of the molecular shape on the stability of the SmC* variant phases is investigated by mixing MHPBC with achiral rod-shaped $\bar{8}$S5 and achiral hockey-stick-shaped sf-7. It

was found that $\bar{8}$S5 is extremely destructive to the stability of the SmC* variant phases. All the SmC* variant phases disappear upon only 5% doping. On the other hand, sf-7 is much more miscible with MHPBC. Although the SmC$^*_{d4}$ and SmC$^*_{d3}$ phases are eliminated upon around 15% doping, the SmC$^*_\alpha$ and SmC$^*_A$ phases survived throughout the whole phase diagram. It clearly shows that the molecular shape of MHPBC resembles that of sf-7 and the impact of the molecular shape on the stability of SmC* variant phases is significant.

There are some future works I would recommend people who are interested in this research area to follow up.

1. Two 9OHF and 10OHF mixtures have some interesting DOR data in thick films. The physics behind it is not clear at the moment. Doping these 10OHF/9OHF mixtures with small amount of C9 might allow us to perform RXRD to acquire the pitch evolution. Hopefully, this interesting pitch evolution would not disappear when adding a sufficient amount of C9 for RXRD studies.

2. It seems like the SmC$^*_{d6}$ phase is present only in the mixtures with the reversed phase sequence. The relationship between the SmC$^*_{d6}$ phase and the reversed phase sequence needs to be studied more, i.e. look for the SmC$^*_{d6}$ phase in other compounds (mixtures) showing a SmC$^*_\alpha$-SmC$^*_{d4}$ transition. It is interesting to see whether the reversed phase sequence is a necessary condition for the formation of the SmC$^*_{d6}$ phase.

3. The temperature window of the SmC$^*_{d6}$ phase is only about one degree in Mixture A and B. Researchers have doped some chiral dopants to compounds having the SmC$^*_{d4}$ and SmC$^*_{d3}$ phases and expand the temperature ranges of these two phases from a few degrees to tens of degrees [58, 59]. Therefore, doping Mixture A and B with some chiral dopants or other antiferroelectric liquid crystal compounds seems a viable approach to increase the temperature stability of the SmC$^*_{d6}$ phase.

4. Dolganov *et. al* have proposed non-uniform tilt in the SmC$^*_{d6}$ phase. A non-resonant peak at $Q_z/Q_0 = 1.333$ should be observed if this is the case. In the next RXRD experiment, we should certainly check the $Q_z/Q_0 = 1.333$ peak with non-resonant energy.

References

[1] P. G. de Gennes and J. Prost, *the Physics of Liquid Crystals, second edition*, Clarendon, Oxford, 1998.

[2] S. Chandrasekhar, *Liquid Crystals, second edition*, Cambridge University Press, Cambridge, 1992.

[3] R. B. Meyer *et al.*, J. Phys. Lett. (Paris) **36**, L69 (1975).

[4] A. Fukuda, Y. Takanishi, T. Isozaki, K. Ishikawa, and H. Takezoe, J. Mater. Chem. **4**, 997 (1994).

[5] H. Takezeo, E. Gorecka and M. Cepic, Rev. Mod. Phys. **82**, 897 (2010).

[6] A. D. L. Chandani, T. Hagiwara, Y. Suzuki, Y. Ouchi, H. Takezoe, and A. Fukuda, Jpn. J. Appl. Phys. Part 2 **27**, L729 (1988).

[7] A. D. L. Chandani, Y. Ouchi, H. Takezoe, A. Fukuda, K. Terashima, K. Furukawa and A. Kishi, Jpn. J. Appl. Phys. *28*, L1261 (1989).

[8] K. Ema, H. Yao, Kawamura, T. Chan and C. W. Garland, Phys. Rev. E **47**, 1203 (1993).

[9] C. Bahr, and D. Fliegner, Phys. Rev. Lett. **70**, 1842 (1993).

[10] P. M. Johnson, D. A. Olson, S. Pankratz, T. Nguyen, J. Goodby, M. Hird, and C. C. Huang, Phys. Rev. Lett. **84**, 4870 (2000).

[11] D. R. Link, J. E. Maclennan, and N. A. Clark, Phys. Rev. Lett. **77**, 2237 (1998).

[12] Y. P. Panarin, O. Kalinovskaya and J. K. Vij, Liq. Cryst. **25**, 241(1998).

[13] E. Gorecka, A. D. L. Chandani, Y. Ouchi, H. Takezoe, and A. Fukuda, Jpn. J. Appl. Phys., Part 1 **29**, 131 (1990).

[14] P. Mach, R. Pindak, A. M. Levelut, P. Barois, H. T. Nguyen, C. C. Huang, and L. Furenlid, Phys. Rev. Lett. **81**, 1015 (1998).

[15] P. Mach, R. Pindak, A. M. Levelut, P. Barois, H. T. Nguyen, H. Baltes, M. Hird, K. Toyne, A. Seeda, J. W. Goodby, C. C. Huang, and L. Furenlid, Phys. Rev. E **60**, 6793 (1999).

[16] S. Pankratz, P. M. Johnson, and C. C. Huang, Rev. Sci. Instrum. **71**, 3184 (2000).

[17] D. A. Olson, X. F. Han, P. M. Johnson, A. Cady, and C. C. Huang, Liq. Cryst. **29**, 1521 (2002).

[18] LiDong Pan, Shun Wang, C. S. Hsu, and C. C. Huang, Phys. Rev. Lett. **103**, 187802 (2009).

[19] E. B. Sirota, P. S. Pershan, L. B. Sorensen, and J. Collett, Phys. Rev. A 36, 2890 (1987).

[20] S. Pankratz, "Optical reflectivity studies on freely-suspended liquid-crystal films",2000, Ph.D thesis, University of Minnesota.

[21] A. Cady, "Optical and resonant x-ray diffraction investigations of molecular ordering in chiral smectic liquid crystals",2003, Ph.D thesis, University of Minnesota.

[22] Z. Q. Liu, "Optical and resonant x-ray studies of chiral smectic-C liquid crystals structures and transitions",2007, Ph.D thesis, University of Minnesota.

[23] Ch. Bahr, C. J. Booth, and D. Fliegner, Ferroelectrics **178**, 229,(1996).

[24] LiDong Pan, Shun Wang, C. S. Hsu, and C. C. Huang, Phys. Rev. E **79**, 031704 (2009).

[25] D. A. Olson, S. Pankratz, P. M. Johnson, A. Cady, H. T. Nguyen, and C. C. Huang, Phys. Rev. E **63**, 061711 (2001).

[26] V. E. Dmitrienko, Acta Crystallogr. Sect. A **39**, 29 (1983).

[27] A.-M. Levelut and B. Pansu, Phys. Rev. E **60**, 6803 (1999).

[28] V. Laux, N. Isaert, V. Faye, and H. T. Nguyen, Liq. Cryst. **27**, 81 (2000).

[29] S. T. Wang, Z. Q. Liu, B. K. McCoy, R. Pindak, W. Caliebe, H. T. Nguyen, and C. C. Huang, Phys. Rev. Lett. **96**, 097801 (2006).

[30] K. L. Sandhya, J. K. Song, Yu. P. Panarin, J. K. Vij and S. Kumar, Phys. Rev. E **77**, 051707 (2008).

[31] W. Weissflog, C. Lischka, S. Diele, I. Wirth, and G. Pelzl, Liq. Cryst. **27**, 43 (2000).

[32] B. K. McCoy, Z. Q. Liu, S. T. Wang, Lidong Pan, Shun Wang, H. T. Nguyen, R. Pindak, and C. C. Huang, Phys. Rev. E **77**, 061704 (2008).

[33] Shun Wang, LiDong Pan, B. K. McCoy, S. T. Wang, R. Pindak, H. T. Nguyen, and C. C. Huang, Phys. Rev. E **79**, 021706 (2009).

[34] D. Schlauf, Ch. Bahr, V. K. Dolganov, and J. W. Goodby, Eur. Phys. J. B **9**, 461 (1999).

[35] J.P.F. Lagerwall, G. Heppke, and F. Giesselmann, Eur. Phys. J. E **18**, 113 (2005).

[36] M. Yamashita, J. Phys. Soc. Jpn. **67**, 198 (1997).

[37] M. B. Hamaneh and P. L. Taylor, Phys. Rev. Lett. **93**, 167801 (2004).

[38] M. B. Hamaneh and P. L. Taylor, Phys. Rev. E **72**, 021706 (2005).

[39] P. V. Dolganov, V. M. Zhilin, V. K. Dolganov, and E. I. Kats, Phys. Rev. E **67**, 041716 (2003).

[40] Shun Wang, LiDong Pan, R. Pindak, Z. Q. Liu, H. T. Nguyen, and C. C. Huang, Phys. Rev. Lett. **104**, 027801 (2010)

[41] A. Cady, J. A. Pitney, R. Pindak, L. S. Matkin, S. J. Watson, H. F. Gleeson, P. Cluzeau, P. Barois, A.-M. Levelut, W. Caliebe, J. W. Goodby, M. Hird, and C. C. Huang, Phys. Rev. E **64**, 050702(R) (2001).

[42] M. A. Osipov and M. V. Gorkunov, Liq. Cryst., **33** 1133 (2006).

[43] A. V. Emelyanenko and M. A. Osipov, Phys. Rev. E **68**, 051703 (2003).

[44] M. Cepic and B. Zeks, Phys. Rev. Lett. **87**, 085501 (2001).

[45] D. A. Olson, X. F. Han, A. Cady, and C. C. Huang, Phys. Rev. E **66**, 021702 (2002).

[46] To be published.

[47] A. Cady, Z. Q. Liu, X. F. Han, S. T. Wang, M. Veum, N. Janarthanan, C. S. Hsu, D. A. Olson, and C. C. Huang, Phys. Rev. E **66**, 061704 (2002).

[48] E. Gorecka, D. Pociecha, M. Cepic, B. Zeks and R. Dabrowski, Phys. Rev. E **65**, 061703 (2002).

[49] B. Jin, Z. Ling, Y. Takanishi, K. Ishikawa, H. Takezoe, A. Fukuda, M.-A. Kakimoto, and T. Kitazume, Phys. Rev. E **53**, R4295 (1996).

[50] Y. Ouchi, Y. Yoshioka, H. Ishii, K. Seki, M. Kitamura, R. Noyori, Y. Takanishi and I. Nishiyama, J. Mater. Chem. **5**, 2297 (1995).

[51] J. T. Mills, H. F. Gleeson, J. W. Goodby, M. Hird, A. Seed and P. Styring, J. Mater. Chem. **8**, 2385 (1998).

[52] R. Stannarius, J. Li, W. Weissflog, Phys. Rev. Lett. **90**, 025502 (2003).

[53] X. F. Han, S. T. Wang, A. Cady, Z. Q. Liu, S. Findeisen, W. Weissflog, and C. C. Huang, Phys. Rev. E **68**, 060701(R) (2003).

[54] S. T. Wang, S. L. Wang, X. F. Han, Z. Q. Liu, S. Findeisen, W. Weissflog and C. C. Huang, Liq. Cryst. **32**, 609 (2005).

[55] Z. Q. Liu, S. T.Wang, B. K. McCoy, A. Cady, R. Pindak, W. Caliebe, K. Takekoshi, K. Ema, H. T. Nguyen and C. C. Huang, Phys. Rev. E **74**, 030702(R) (2006).

[56] E. Enz, S. Findeisen-Tandel, R. Dabrowski, F. Giesselmann, W. Weissflog, U. Baumeistera and J. Lagerwall, J. Mater. Chem. **19**, 2950 (2009).

[57] F. C. Yu and L. J. Yu, Liq. Cryst. **35**, 799 (2008).

[58] S. Jaradat, N. W. Roberts, Y. Wang, L. S. Hirst and H. F. Gleeson, J. Mater. Chem. **16**, 3753 (2006).

[59] J. Kirchhoff and L. S. Hirst, Phys. Rev. E **76**, 051704 (2007).